Traction Control of an Electric Vehicle with Four In-Wheel Motors

by

Amin Hajihosseinlu

A thesis submitted to the Faculty of Graduate Studies of
The University of Manitoba
in partial fulfillment of the requirements for the degree of

MASTER OF SCIENCE

Department of Electrical and Computer Engineering
University of Manitoba
Winnipeg, MB, Canada

Abstract

This thesis evaluates an electric vehicle with four independently-controlled in-wheel electric motors. The electric vehicle investigated in this work requires a main controller that not only coordinates with each individual motor drive controller, but is also needed to distribute torque and power to each in-wheel motor. The controller adjusts the speed of each motor to the driving conditions according to the requirements and emulates the behavior of a mechanical differential. Then, in addition to the electronic differential controller, a simple yet robust control strategy for maximizing traction force between tire and road is developed and presented. Moreover, the controller continuously senses the yaw rate and prevents over- and under-steering by adjusting the torque on the right or left wheels. Simulation and experimental results validate the proposed strategy.

Acknowledgements

First and foremost, I would like to express my sincere gratitude to my academic advisor, Dr. Shaahin Filizadeh for giving me the opportunity to work here on a project that I am enthusiastic about and for his continual support and guidance. Without his support and the facilities that he provided, this dissertation would not have been possible.

I want to thank my parents for their support. I cannot find the words to express my gratitude to you, Mom and Dad, and I certainly cannot imagine two better role models. Their life stories are a testament to the fact that hard work and perseverance will enable you to achieve your dreams.

I wish to express my appreciation to the University of Manitoba for making it possible for me to accomplish my goals on this project. I would like thank Mr. Erwin Dirks providing technical insights and assisting me throughout, and Mr. Garry Bistyak for sharing his industry experience. I am indebted to all my friends that were always there to listen and help and make my graduate studies the most memorable and intriguing period of my life. Finally a special thank you goes to Azita Fazelkhah for her support and encouragements.

Dedication

To my loving parents and supportive friends.

"All mankind is divided into three classes: those that are immovable, those that are movable, and those that move"

Benjamin Franklin.

==========

Table of Contents

List of Tables

List of Figures

Chapter 1

TRANSPORTATION ELECTRIFICATION

1.1 Introduction

Modern transportation has revolutionized humans' lives. With fast, safe, and comfortable transportation, urban sprawl has significantly expanded. It is predicted that the number of cars will surpass 2.5 billion units by 2050 [1]. Recently, environmental concerns along with the shortage and the uncertainty of the supply of fossil fuels have led the automotive industry to increasingly consider alternative vehicular drivetrains, such as hybrid, plug-in hybrid, and electric. Conventional cars that utilize internal combustion engines (ICEs), operate by burning fossil fuels. They emit green house gases such as carbon dioxide and carbon monoxide. These gases result in pollution effects and global warming, which not only affects the earth's climate, but is also considered a major threat to humans lives. Moreover, gas price is significantly

increasing. These issues are compelling car manufacturers to come up with modified vehicles for transportation with the least possible amount of emission. Car industries are now approaching a new phase in their development efforts that entail building powerful, long-range, fast-charging and less expensive electric vehicles. For decades battery electric cars have not been used, because of the lack of energy storage devices. By the 20th century, electric vehicles used to compete with ICE cars, but soon the short range of electric cars and the low price of oil led to the disappearance of battery electric vehicles from the market. Nowadays, however, studies show that with improvements in batteries, electric motor drives, and power electronics, these environmentally-friendly vehicles are able to perform satisfactorily and at times even better than conventional vehicles.

Other recently-developed concepts are more-electric vehicles, use of in-wheel motors, and removing most of the mechanical parts of the drive-train (such as shaft and differentials). These kinds of vehicles that are equipped with in-wheel electric motors have shown high reliability in terms of drive-train efficiency and motion control stability. In recent years, significant amount of research have been conducted on several advantages of independently driven in-wheel motors. It increases efficiency of the drive-train since mechanical shaft, axles and mechanical differential will be removed in vehicles with in-wheel installation. The more developed advantage of electric vehicles with in-wheel motors is to prevent unintended vehicle behavior and increase its stability and controllability.

1.2 Motivations and Problem Definition

The structure of a typical all-electric vehicle is shown in Figure 1.1. As it is seen, there is one electric motor in the drive-train, which is connected to the rear wheels using a gear box and a mechanical differential.

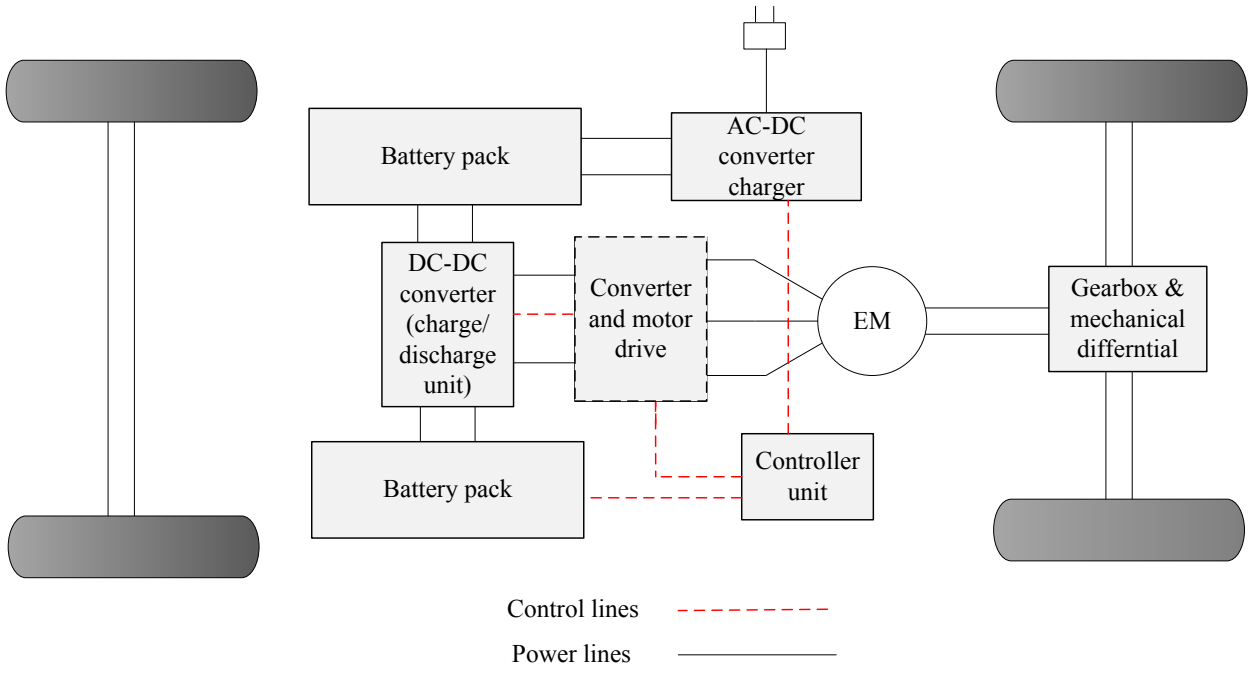

Figure 1.1: Schematic diagram of an all-electric vehicle

A new trend in electric cars is the use of in-wheel motors. An in-wheel motor, also called a wheel hub motor, is an electric motor that is incorporated into the hub of the wheel and drives the wheel directly. This new structure in electric vehicle drive-trains eliminates the transmission line and the differential altogether. Figure 1.2 shows a schematic diagram of an all-electric vehicle with four in-wheel motors. As a result of removing the transmission line and the mechanical differential, the overall weight of the drive-train as well as the delay of the motor torque caused by the higher inertia

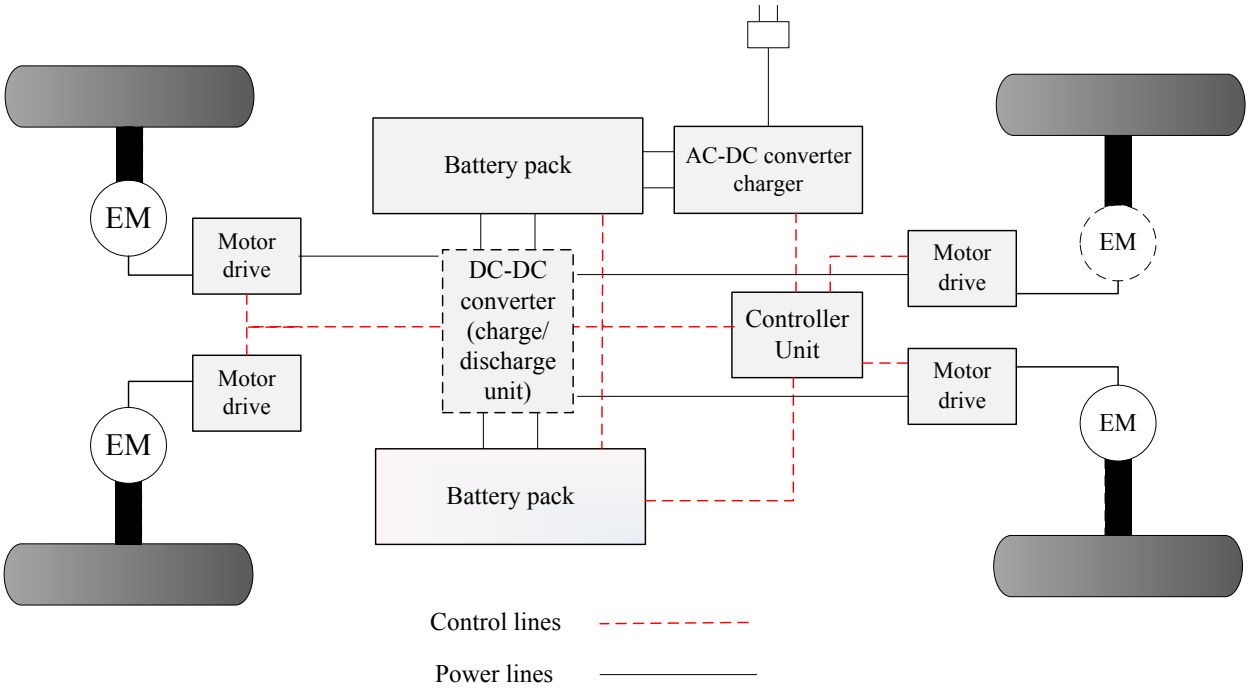

Figure 1.2: Schematic diagram of an electric vehicle with four in-wheel motors

of the mechanical components of the drive-train will be reduced. This will allow a more precise control of the motors with faster response. The main benefit of the conventional mechanical differential that it is a proven and reliable concept, although it has its weaknesses. For example, it can only regulate the rotational speeds of the wheels, but not the torque. By supplying equal torque to all wheels, mechanical differential are unable to produce any yaw stabilization force on the vehicle. On the other hand, electronic differential not only regulates different speed for different wheels, but it also resists vehicle rotation, over- and under-steering by providing more torque to outer wheels and less torque to inner wheels. This has driven the automotive industry to design complicated and expensive components in order to improve a vehicle's performance such as electronic stability control and/or electronic stability program [2, 3].

This thesis investigates the different aspects of all-electric vehicles and compares them to the conventional internal combustion engine cars; it will also look into advanced traction control systems of electric vehicles with four independent in-wheel electric motors. This thesis, primarily, explains the steps toward the design of an electronic differential, which will significantly advance the operation and the efficiency of the drive-train. It will then look at the advantages of an electronic differential in order to improve a vehicle's performance by extending the control range of the motors. It will be illustrated that by use of four independent in-wheel motors the yaw-motion stability control can be markedly improved. Furthermore it can also be extended to use regenerative braking where all of the in-wheel motors are used as generators during braking to recover large portions of the kinetic energy. Use of multiple motors increases the reliability of the vehicle as it may continue to operate even if one or two of the motors may fail. In that case, the controller will use the other three motors for vehicle propulsion. The yaw motion controller must adjust the traction forces to different wheels to prevent any unintended yaw force of the vehicle. This thesis designs and develops a motor drive system for drive-trains. The existing field-oriented control method is explained and state space equations are utilized to simulate the traction control system of the drive-train. A resonant converter is studied and presented in the appendix and its applications in electric vehicle drive-trains are explained. The concept of an electronic differential is illustrated, developed, and added to the existing controller. After verifying the functionality of the electronic differential, this thesis presents the wheel slippage and proposes a method that improves the traction control system and increases the vehicle's overall stability.

1.3 Past work

Electric vehicles are expected to have faster torque response than conventional vehicles due to advanced motor-control methods, which allow the electric motor to generate rapidly-varying amounts of torque. AC machines, such as induction machines and the permanent magnet synchronous motors (PMSM), have the major requirements for electric vehicle propulsion [4]. The ac motor drive dynamic behavior can be significantly improved using advanced ac control methods. Among several ac motor drives, the direct torque control appears as an effective and robust control scheme for in-wheel electric motors [5–7]. Electric machines need to be optimized for a range of operating speeds. In the case of an electric vehicle with four in-wheel motors, each motor must offer fast and accurate response. Since, it is assumed an all-electric vehicle contains regenerative braking system, the electric motors must also be able to work as a generator, as an electrodynamic brake for recuperation of the kinetic energy [8]. In addition to fast torque and speed response, the other main demands of an electric motor include: high efficiency over a large range of the torque-speed characteristic curve and small volume and weight (as they are to be installed in the hub of the wheel), low maintenance, high reliability, and low price. Different electric motors with high negative and positive torque characteristics have been investigated including switched reluctance and permanent-magnet synchronous motors [9, 10]. With such requirements in performance, the design of vehicular-grade machines is particularly challenging.

Other important components that play key roles in commercializing all-electric

vehicles are power electronic devices. The power electronic system must be efficient to increase the range of the electric vehicle. In order to develop an efficient and high-performance vehicle, the selection of switching converters, motor drive converters, switching methods, and system integration become critical. In [11–14] the authors investigate the new trend and the function of power electronic subsystems and their applications in drive-train.

Drive-train layouts including one, two or four independently controlled motors have been considered. Use of four independent in-wheel motors provides the opportunity to generate different torque (speed) references to each wheel independently [15]; this not only leads to a better differential operation, but also has considerable potential for improved yaw-motion stability control [16]. In-wheel motor controllers have been considered for various aspects of motion stability such as yaw control, lateral control, and anti-skid braking systems [17, 18]. Different topologies and aspects of electronic differential, such as master-slave control or synchronization structure, and sliding mode yaw-motion control, have been investigated in the literature. In [19], the authors investigate the advantages of the electronic differential in the vehicle motion stability. Chen and Wang investigate an electric vehicle with in-wheel motors during cornering and maneuvering by comparing them with conventional cars and they demonstrate significant improvements in the drive-train performance [20].

This thesis proposes an electronic differential based on fundamental geometric expressions, which describe the motion of the vehicle and its four wheels while turning. Using a purely mathematical procedure, this thesis shows that the addition of an electronic differential requires simple modifications to the existing electric vehicle

drive-train controller structure. Additionally, the method proposed herein considers the slippage of the wheels in the design of the electronic differential and proposes a method for yaw-motion stability control. Then, a simulation case and two experimental setups are developed to demonstrate the advantages and feasibility of the proposed methods. In parts of this thesis it is assumed that the yaw-rate and the ground vehicle-speed are available through continuous sensing. Ground speed sensors using optical means are found in [21, 22]. Other speed estimation methods have also been proposed in the literature including in [23].

1.4 Thesis Organization

The thesis is presented as follow:

Chapter 2 presents an outline of an electric vehicle and its necessary components. Different components of a typical drive-train of an electric vehicle are explained in this chapter. In-wheel technology as a new trend in the electric vehicle industry is presented. A regenerative braking system is explained and its several advantages are illustrated. Battery technology and common energy storage systems are included in the same chapter. An introduction to power electronics and motor drive systems in drive-trains are also presented in this chapter and their designed and development are demonstrated in Chapter 3 and Appendix.

In Chapter 3, design, modeling, and mathematical equations governing the kinetic and dynamic vehicle model will be presented. The thesis continues with an introduction to the electronic differential and its necessity. Basic geometric equations that

underline the turning action are then presented and used to derive a controller that generates different power commands for different wheels during cornering.

Chapter 3 also presents another important phenomenon in vehicular motion, namely wheel slippage. It happens in particular on icy and snowy roads. The thesis throughly investigates this fact and explains why it happens and how it can be prevented. An algorithm for the operation at optimal wheel slippage is developed using the curves of adhesion friction versus wheel slippage. This allows for maximizing the traction force without excessive power consumption by each motor. This chapter investigates yaw motion control and enhancing the stability of the vehicle [2, 3].

In order to verify parts of the proposed methods, a simulation model and an experimental setup have been developed and will be discussed in Chapters 4 and 5. First, the popular field-oriented control method is modeled in PSCAD/EMTDC simulator. Then, this model is used in a real-time digital simulator (RTDS).

A small-scale laboratory setup is developed to test the performance of the proposed algorithm using an actual electric motor drive system connected to a synchronous machine. This emulates the in-wheel motor in the actual implementation of the system in a real vehicle. The electronic differential algorithm is implemented on RTDS, which is then interfaced with the power electronic of the drive system. A field-oriented control scheme is developed, which upon receiving the torque command from the RTDS will generate proper stator current commands for the ensuing PWM switching scheme. Conclusions, contributions and future work are presented in Chapter 6.

Chapter 2

All-Electric Vehicle Drive-Train

An all-electric vehicle uses a portable energy storage system such as a battery, and has one or more electric motors for propulsion. When the battery is charged, the car uses this energy to propel the vehicle by driving the electric motor(s). All-electric vehicles have several benefits compared to conventional internal combustion engine vehicles. They produce no local air pollution, have lower operating and maintenance cost, and higher efficiency. However, they are still considered expensive compared to conventional vehicles.

Even though all-electric vehicles are still more expensive than conventional cars, recently, all-electric vehicles have become more popular and are being commercialized faster than before. Some famous car companies have manufactured all-electric vehicle such as BMW i3, Chevrolet Spark, Honda FIT EV, Nissan leaf and Tesla Model S.

The several advantages and necessity of electric vehicles motivate scientist and industry to perform significant research on electric vehicle drive-trains. This chapter introduces electric vehicles and their differences with conventional combustion engine

vehicles. It presents major components of an electric vehicle drive-train and their important role in this recently-grown industry.

2.1 Use of In-Wheel Electric Motors in Drive-Trains

Nowadays, significant amount of research is being performed on a new concept called more-electric vehicles in which many mechanical parts are removed and replaced with electrical parts. Transmission line, gearboxes, axles and mechanical differentials are common mechanical components that are desired to be removed in order to minimize mechanical losses, make the vehicle lighter and increase the overall efficiency. In-wheel motors are a new trend in the electric vehicle industry that researchers and manufacturers are interested in utilizing in their new designs. There is significant research done on these type of electric vehicles because of their compact structures, fewer mechanical connections, less transmission losses, and extra space and flexibility of driving [24]. A typical electric vehicle has one motor in the drive-train that sends power to the axles and the wheels. In electric vehicles with in-wheel electric motors, the power and control circuits, including the dc/ac inverters are all tucked into the wheel space.

When designing an in-wheel electric motor for an electric vehicle, it is critical to consider all different factors in this drive-train controller design. These requirements often present themselves as the design challenges that were not encountered in traditional drive-trains. Safety requirements are one of the vital factors that cannot

be ignored. This narrows down the design choices and provides a logical direction towards an in-wheel electric motor design which includes:

1) considering a single point failure on a wheel and its impact on the vehicle stability;

2) minimizing the total motor volume and mass, and minimizing the complexity and cost of the system;

3) integrating power electronics to provide a more practical solution through higher efficiency, less volume, less expensive drive-train, and more importantly, providing easier drive-train assembly by minimizing the number of connections;

In order to obtain a simple understanding of an independently-controlled electric motor and its difference from conventional wheels, Figure 2.1 gives a general view of an electric motor that is controlled independently. Although in this figure, motor drive converter and the controller are not built inside the hub of the wheel, it pictures an electric motor that is controlled and driven independently, i.e. without any use of shaft and/or mechanical differential.

2.2 Power Electronics and Motor Drive Controller

This section provides an overview of the power electronics used in the traction system of a plug-in hybrid electric and plug-in electric vehicles and studies a high frequency power converter used in the drive train.

Conventionally, electric power is used in vehicles for electronic accessories, such as power windows, entertainment systems, air conditioning, dashboard instruments, seat adjustment, seat heaters and other accessories. Recently manufactured electric

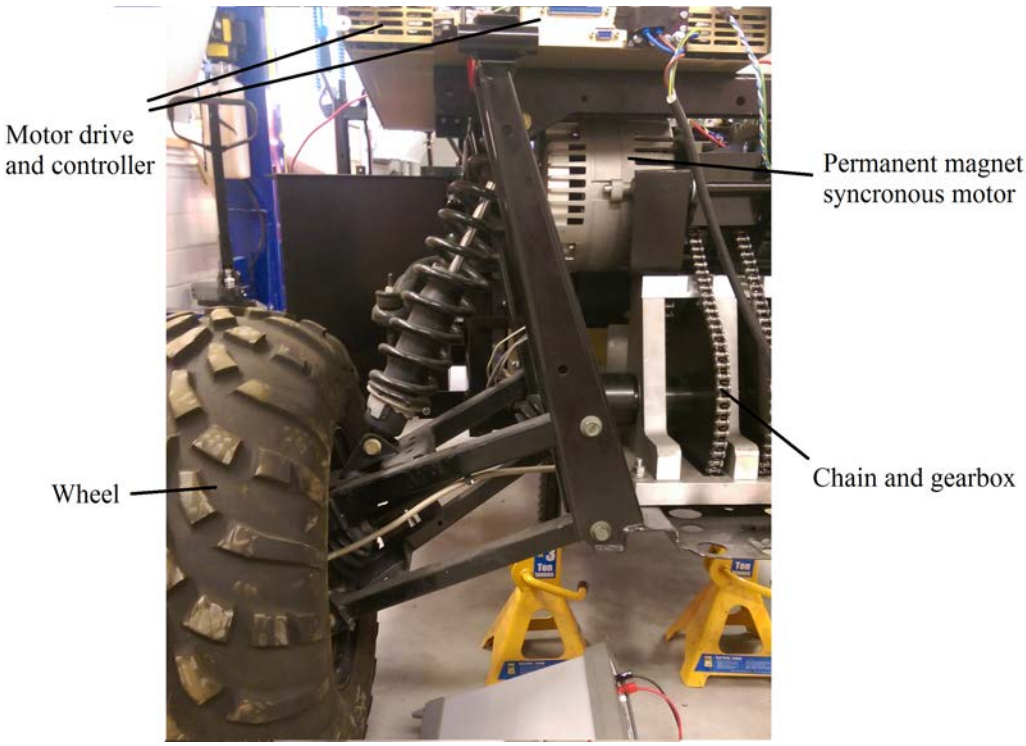

Figure 2.1: Independently-controlled electric motor

cars use electric power not only for electric accessories but also for the main drive-train. These electric vehicles look quite similar to gasoline-propelled cars but have more advanced electronic-based technology in their drive-train. This has raised the importance of power electronics converters in all-electric vehicle's industry.

The main power electronic components of a electric vehicle are a dc/dc converter that steps up battery's voltage to higher voltage level to drive the motor and/or step down the battery's voltage to a lower voltage level for the electronic accessory usage. An inverter is necessary in order to convert the dc to ac at a required voltage and frequency for the electric motors. This inverter must be bidirectional since it is also used to convert ac voltages from the generator to dc voltage to recharge the batteries through the regenerative breaking system. In order to charge the battery an ac/dc rectifier is utilized, which must be capable of converting very high rate of power.

Power electronics-based components can be seen in Chapter 1 in Figure 1.2. The efficiency of these switching converters are high and they can be isolated and non-isolated. High efficiency, high power density, high reliability, small size, and low cost are the typical requirements for these converters. Increasing the switching frequency to the range of megahertz significantly reduces the need for larger energy storage elements and that increases the energy density and decreases the size of the converters. However, by increasing the frequency, the power loss, which primarily depends on the switching frequency, will be greatly increased. Nowadays, the latest zero current switching and zero voltage switching methods have been utilized in order to miniaturize the bulky and heavy converters and increase the efficiencies. In [25–27] some topologies for a resonant converter application in electric vehicle are proposed. In [28] the author clearly represents that power electronic components can be miniaturized by increasing the frequency to tens of megahertz. Although the paper [28] does not directly investigate resonant converters applications in electric vehicles, it gives a clear view of resonant converters that can be used in vehicular applications. This approach will greatly reduce the size and the price of the power electronic components and increase their overall efficiency.

In the appendix, a high frequency resonant converter has been designed, modeled and developed. This resonant converter has several applications in electric vehicles' drive-train, which are used for fast charging, dc/dc step up/down of the voltage and dc/ac converters for motor drive systems.

2.2.1 Motor Drive

The motor drive is used to provide proper dc or ac voltage for the motor with desirable amplitude and frequency. The drive processes the power flow from the stiff dc batteries to the motor and vice versa. A controller is needed to generate gating pulses for the converter, based on the driver's input command. During braking the motor drive is also responsible to bring the energy back to the batteries. Figure 2.2 shows a simple diagram of a motor drive used in an electric vehicle.

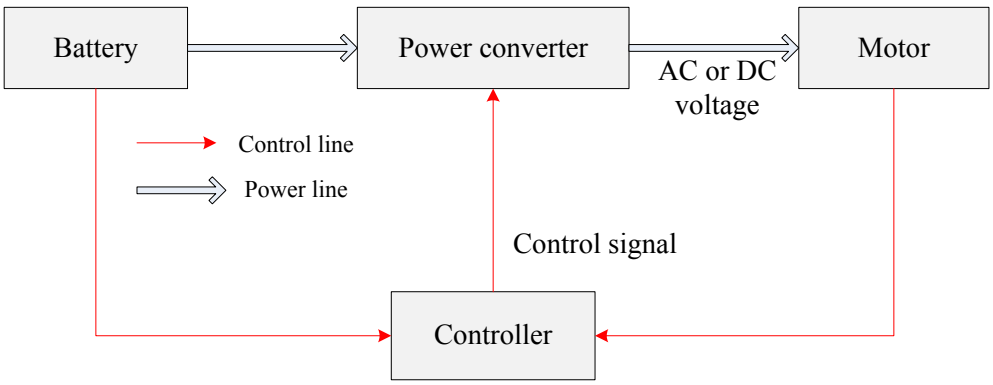

Figure 2.2: A typical diagram of a motor drive system

There are different kinds of machines and motor drives with dc or ac input voltages. The robustness of ac machines compared with dc machines makes them more appealing in several motor drive applications including in electric vehicles. The robustness of ac motors is considered beneficial only when ac motor drives are precisely designed with required complexity. Fast response is a critical requirement for drive-train systems; motor drives must respond instantaneously with the changes in the torque commands. In dc machines, the torque is directly controlled by the armature current without any dynamics involved, which makes the motor show instantaneous torque

response. AC motors can have faster and more accurate torque response compared to dc drives, but at the expense of more complicated drive systems [29]. Among several types of ac motors, permanent magnet synchronous motors (PMSM) show promising application in electric vehicle industry. They have several advantages including small size, light weight, fast response, brush-less structure and high efficiency [30]. In torque control of these electric motors, it can be assumed that torque is proportional to current. Torque control is critical in applications like electric vehicles since the acceleration pedal presents a torque command for electric motors. When the current suddenly changes, the torque will be instantly changed, which gives great performance in vehicular technology. The control strategy of PMSMs will be presented in Chapter 3.

2.2.2 Regenerative Braking System

In conventional vehicles, kinetic energy is converted to heat on the surface of frictional pair during mechanical braking and is wasted; mechanical energy, however, can be transformed into electrical energy.

A regenerative brake system is an energy recovery mechanism, which slows down an electric vehicle by converting its kinetic energy into electrical energy using generators, which can be stored into the batteries or supercapacitors. Regenerative braking systems have several advantages, which make them attractive for automotive industry. The wear and tear of the friction brake is reduced specially in downhill motion and hard braking. Since the brake is electrical by applying negative torque to the motor shaft, it generates less noise. Besides the above advantages, it greatly improves

the vehicle efficiency and reduces range anxiety [31]. However, the design process of a regenerative braking system can be complicated with several restrictions such as battery capability for fast charging and power electronic converters and motor characteristics. In the design process and studying of regenerative braking controllers different factors must be considered; it must identify the driver's intention for braking based on his/her action on brake pedal. It also needs to determine the vehicle state and the amount of brake force required and, then, distribute the mechanical braking force and electromagnetic force. The electromagnetic braking may not generate enough negative force to the vehicle to stop the car, therefore, mechanical braking should be added to the electromagnetic braking to stop the car based on the driver command. In order to meet some of these requirement, several topologies have been investigated in different literature [32, 33]. In some cases supercapacitors are used to absorb the energy quickly since they have very high power density while batteries have high energy density. In some studies researchers utilize supercapacitors to take advantages of their very high power density [34–37].

2.3 Battery pack

It can be said that on-board energy storage systems are the most crucial aspects of electric vehicles. Among various choices of energy storage devices batteries have been utilized in many applications due to their ease of use and availability with current electric infrastructure. A battery is a simple energy storage device that converts chemical energy into electrical energy and vice versa. A battery consists of one or

more cells, which can be connected in parallel and/or series. By connecting cells in parallel or series it is possible to achieve the desired voltage or current of the battery pack. Each cell consists of three different parts namely the anode, the cathode and the electrolyte. Currently, the most prohibiting factor for electric vehicles to compete with ICE vehicles are batteries because of their high cost, lack of high performance in cold weather as in Canada, low charging rate and, more importantly, low energy density.

While the number of highway-capable electric cars is increasing every day, they still face short driving ranges that greatly limit their sales and practicality. The Mitsubishi i-MiEV, Nissan Leaf, and Ford Focus Electric have electric ranges [the maximum distance that can be traveled on a single charge] of between 60 and 76 miles and the Tesla Roadster has a much higher range of 244 miles [38]. Although these ranges show improvement in electric vehicle industry, they are still lower than an ICE car. This low driving range creates range anxiety, the fear that the car has insufficient stored electricity to reach to its destination [31]. Even if ICE cars could not achieve such a superior driving range, they can be refueled at any gas station in a short time. Recharging time for an electric car can take more than an hour.

Figure 2.3 illustrates the energy density of commonly used materials and energy storage devices in a logarithmic plot with a base-4 log scale used in the Y axis [39]. As it is seen, chemical-type energy materials have very high specific energy and energy density, while electrochemical materials (batteries) have very low rate (less than one). In this figure, lithium-ion batteries are the only electrochemical storage devices that have energy density more than 1 MJ/L. For supercapacitors specific energy is too

low, around 0.02 MJ/kg. They, however, show very high power density which is typically 10 to 100 times more than typical batteries. They can be used for maximizing acceleration and regenerative braking systems since they can absorb or provide high current for short amount of time.

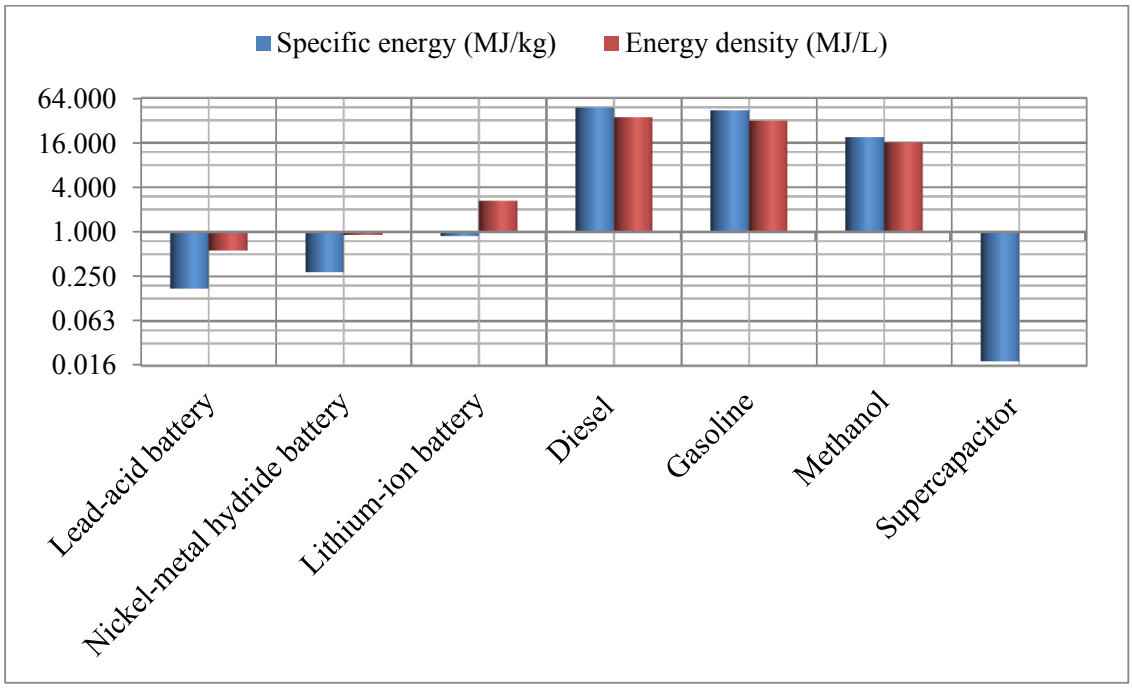

Figure 2.3: Energy densities of common energy storage materials

Chapter 3

DESIGN AND MODELING

In order to design the drive-train of an electric vehicle, a suitable model of the vehicle is needed. This thesis mainly focuses on electrical design of the drive-train and does not use advanced vehicle dynamics models. Besides, its main goal is to propose a reliable method for the motor drive and the control system for a drive-train. At first, a model for the motor drive controller is needed to control the three-phase permanent magnet motor. The model is presented here and the design and development will be presented in Chapter 4. After having the motor drive function properly, the traction control system will be integrated into the existing controller. Then this chapter explains electronic differential and its important role in drive-train with in-wheel motors. It illustrates the geometry of a vehicle while turning and derives basic equations needed to design and understand the theory of electronic differentials. Since the rates of acceleration and deceleration are low, certain assumptions can be applied to the vehicle model to simplify the dynamical model [40]. Moreover, in this chapter a traction control system is demonstrated, which includes preventing the excessive

slippage on the startup in slippery roads, boosting the vehicle stability in sudden changes in the road condition, preventing over- and under-steering, and limiting the slippage on off-road trails and bumpy roads.

3.1 Motor Drive Controller Design and Development

In this project three-phase permanent magnet synchronous motors (PMSMs) are used. PMSMs are very reliable since no brushes are used. They have high efficiency with smooth rotations with minimum ripple. This section demonstrates the vector control, which is used to drive PMSMs and briefly explains the theory behind field oriented control method [29]. The following steps demonstrate different equations for PMSMs and a procedure to design a basic ac motor drive controller. For designing a motor drive controller for a PMSM, the *abc* phase variables are transformed into the rotor reference frame, which is also the synchronous reference frame in steady state. Stator voltage equations in the stationary *abc* reference frame are presented here in equation (3.1).

$$\overrightarrow{v}_{abcs} = \overline{R}_s \overrightarrow{i}_{abcs} + \frac{d}{dt} \overrightarrow{\lambda}_{abcs} \tag{3.1}$$

where $(\overrightarrow{f}_{abcs})^T = [f_{as}\ f_{bs}\ f_{cs}]$ (f represents voltage v, current i or flux linkage) and $\overline{R}_s = diag[R_s\ R_s\ R_s]$

The flux linkages are

$$\overrightarrow{\lambda}_{abcs} = \overline{L}_s \overrightarrow{i}_{abcs} + \overline{\lambda}_f \tag{3.2}$$

where L_s is stator inductance and λ_f is the amplitude of the flux linkage. These equations need to be transformed to the rotor reference frame. Following shows the transformation equations

$$T_{abc\to dq} = \frac{2}{3}\begin{pmatrix} \cos(\theta) & \cos(\theta - \frac{2\pi}{3}) & \cos(\theta + \frac{2\pi}{3}) \\ \sin(\theta) & \sin(\theta - \frac{2\pi}{3}) & \sin(\theta + \frac{2\pi}{3}) \\ 0.5 & 0.5 & 0.5 \end{pmatrix} \tag{3.3}$$

(3.4) and (3.5) show dq-based equations.

$$\begin{aligned} v_q &= R_s i_q + \frac{d}{dt}\lambda_q + \omega_r \lambda_d \\ v_d &= R_s i_d + \frac{d}{dt}\lambda_d - \omega_r \lambda_q, \end{aligned} \tag{3.4}$$

where

$$\begin{aligned} \lambda_q &= L_q i_q \\ \lambda_d &= L_d i_d + \lambda_f \end{aligned} \tag{3.5}$$

Here i_d and i_q are the dq axis stator currents, v_d and v_q are the dq axis stator voltages, R_s is the stator phase resistance, L_d and L_q are the dq axis phase inductances, λ_d and λ_q are dq axis flux linkages, and ω_r is the rotor speed in electrical radians per second. All equations are expressed in terms of electrical angles. The subscript "s" is used to refer to stator quantitative earlier but it is dropped for simplification. λ_f is the amplitude of the flux linkage established by the permanent magnet as viewed from the stator phase windings. The d- and q-axes inductances are

$$L_d = L_{ls} + L_{ms} \quad and \quad L_q = L_{ls} + L_{mq} \tag{3.6}$$

L_{ls} represent the leakage inductance. The electromagnetic torque is given by

$$T_e = \frac{3}{2}\frac{P}{2}[\lambda_f i_q + (L_d - L_q) i_d i_q] \tag{3.7}$$

where P is the number of motor poles. The rotor position information gives the position of d- and q- axes. The rotor position can obtained by

$$\theta_r(t) = \int_0^t \omega_r(\tau)\mathrm{d}\tau + \theta_r(0) \tag{3.8}$$

Equations (3.1)-(3.7) can be included in the vehicle model and simulation case. In order to simulate the PMSM using a computer, state-space representation is required which is provided in [29]. This method is used for the PMSMs drives in the electric vehicle application to deliver the required strong performance. The torque expression in equation (3.7) for the PMSM shows that if the d-axis current is maintained constant, the generated torque is proportional to the q-axis current. For the special case, when i_d is kept zero $\lambda_d = \lambda_f$ and

Therefore, torque will be

$$T_e = K_e i_q \tag{3.9}$$

where K_e motor constant and can be calculated from equation (3.7). The block diagram of the field oriented control drive for PMSM is shown in Figure 3.1.

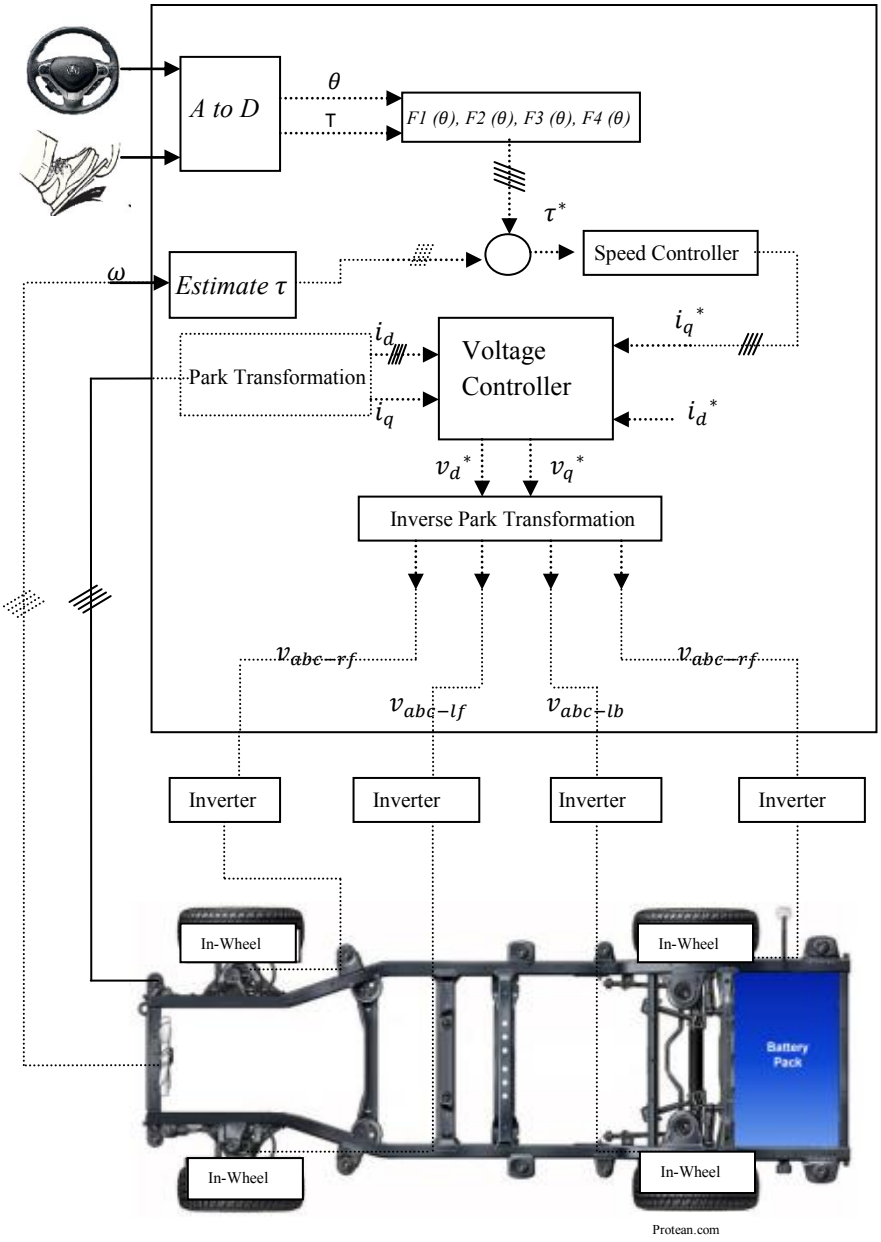

Figure 3.1: Schematic diagram of the controller including electronic differential design implemented in conjunction with a real-time digital simulator

A simulation case for this drive system is also developed in PSCAD/EMTDC simulator. It is later used in a real-time digital simulator to perform the experimental setup. The simulation case is shown in Figure 5.2.

3.2 Vehicle Dynamic Equations in Longitudinal Motion

Basically, the vehicle equations of motion in longitudinal direction can be presented by equations (3.10), (3.11), and (3.12).

$$M(\frac{dV}{dt} - u\gamma) = \cos(\theta)(Fr_{lf} + Fr_{rf}) + Fr_{lr} + Fr_{rr} - F_a \tag{3.10}$$

where M is vehicle mass. θ is steering wheel angle and is shown in Figure 3.2. γ and u are the yaw rate and the lateral speed, respectively. Fr_i is rolling force of tire i where i is lf, rf, lr, rr and F_a is air drag, which is shown in equation (3.17). lf, rf, lr, rr stand for left front, right front, left rear and right rear, respectively.

$$M(\frac{du}{dt} + V\gamma) = Fy_{lf} + Fy_{rf} + Fy_{lr} + Fy_{rr} - F_a \tag{3.11}$$

where Fy_i is lateral net force of tire i.

$$I\frac{dr}{dt} = 2(L_2(Fy_{lf} + Fy_{rf}) - L_1(Fy_{lr} + Fy_{rr})) \tag{3.12}$$

I is the yaw moment of inertia and L_1 and L_2 are the distances from vehicle's center of mass to the rear and front wheels, respectively. L_1 and L_2 are shown in Figure 3.2.

In most parts of this thesis, the acceleration and deceleration are modeled when the vehicle is traveling forward. In other words, the motor drive and the proposed method for maximizing traction control system and optimizing the power usage during

high wheel slippage are exclusively in longitudinal direction. Therefore, lateral forces and side slip angle have been neglected for simplicity.

Therefore, in (3.10) u and γ will be neglected for now. However, they should be considered whenever the vehicle is cornering and accelerating or decelerating.

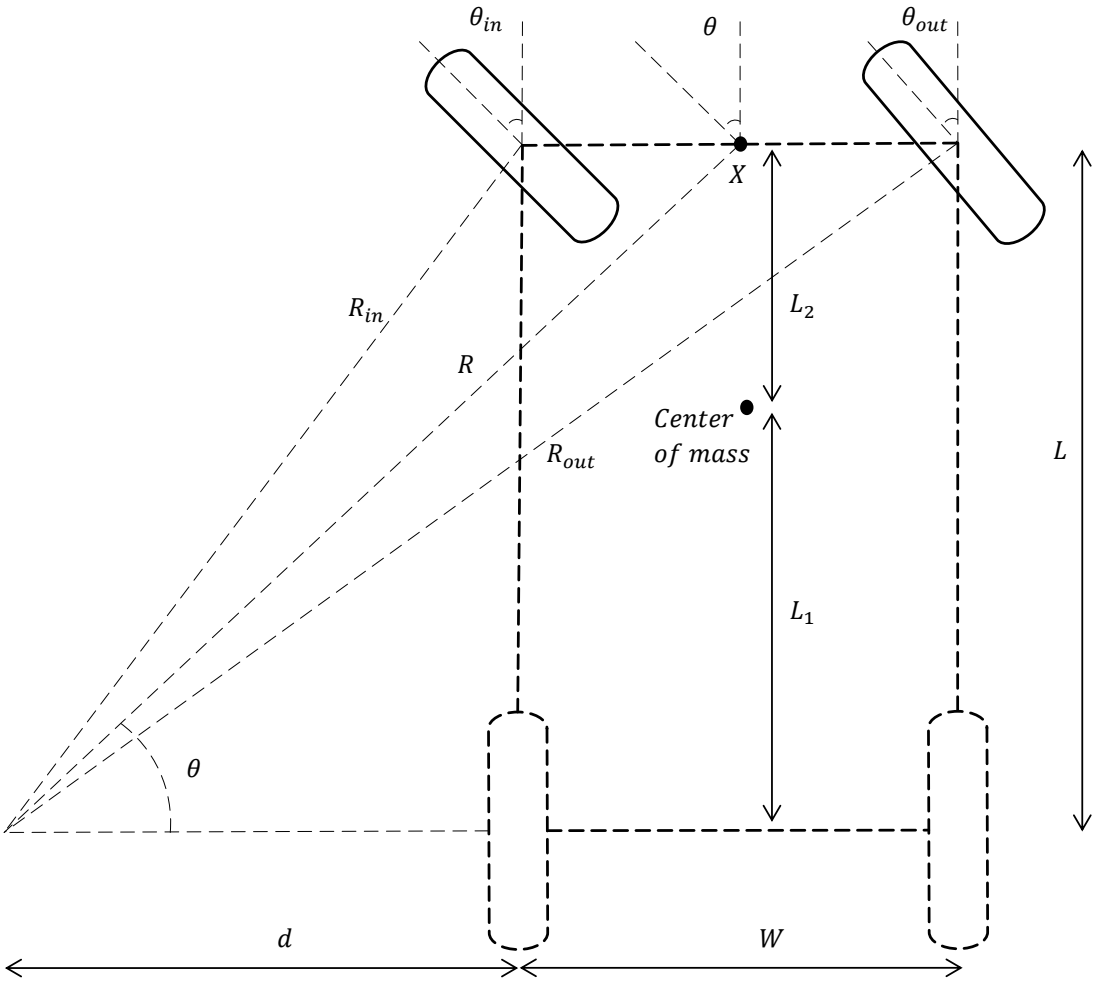

Figure 3.2: Vehicle's kinematic model

By simplifying equation (3.10) and neglecting equations (3.11) and (3.12), vehicle dynamics will be simplified. Dynamic equations used in this thesis originally come from Newton's law. Newton's second law states that acceleration of an object is

proportional to the net force exerted on it. There are mainly two different sets of equations, which are highly related to each other. One is for the vehicle dynamics and the other is for wheel dynamics. Although the dynamic model considered here is relatively simple, it retains the essential dynamics of the vehicle.

Figure 3.3 shows an image of a car and the linear forces acting upon it. Note that angular forces exerted to the wheel are not shown in this figure. Wheel forces can be seen in Figure 3.4. In Figure 3.3, it is assumed that the vehicle travels at constant speed and in a straight path and the forces are just for the vehicle and not for the wheels. There are only four forward forces applied to the vehicle, which make the vehicle go froward.

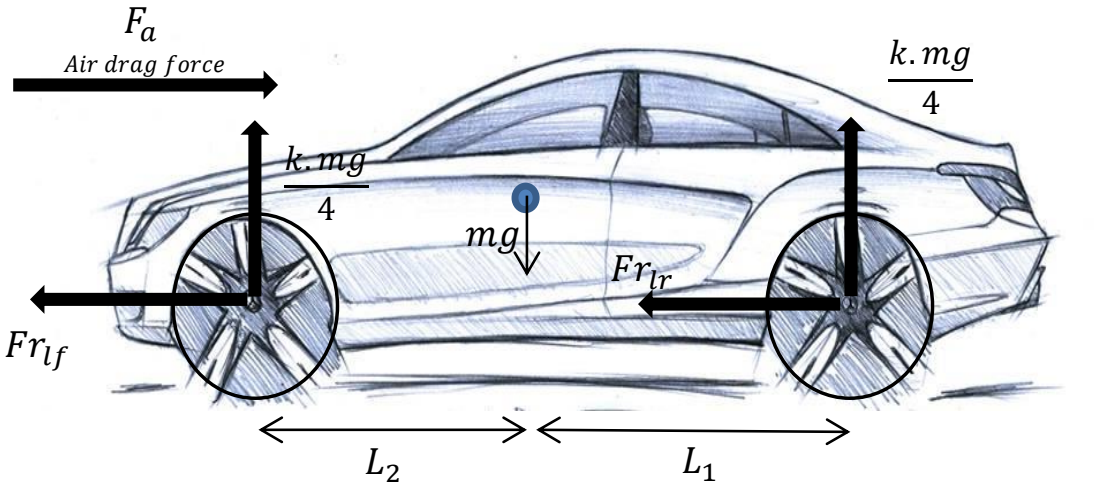

Figure 3.3: Forces exerted on the vehicle

Normal forces on each wheel are caused by the vehicle's weight. In the Figure 3.3, the coefficient k represents that normal forces exerted on each tire may not necessarily be equal. For example, during acceleration (deceleration) the normal forces on front (rear) wheels are higher than rear (front) wheels or it can be said that in turning

the normal forces on outer wheels will be higher than inner wheels. However, for simplicity it is assumed that k is equal to one, which make all four normal forces equal.

Dynamic equations of the vehicle are divided into two parts. The dynamic equations of the four wheels are presented first, followed by the dynamic equations of the vehicle motion. The following shows the dynamics of the wheels, assuming that each wheel is powered by its own motor (in-wheel installation).

$$J\frac{d\ \omega_i}{dt} = \tau_i - Fr_i - b\ \omega_i \qquad i = lf, rf, lr, rr \tag{3.13}$$

where J is moment of inertia of each wheel, τ_i is the torque generated by the respective motor, b is the viscous friction coefficient and Fr_i is rolling force of each wheel which is shown in (3.14).

$$Fr_i = U(S_i)N_i\cos(\alpha) \qquad i = lf, rf, lr, rr \tag{3.14}$$

In (3.14) S_i is the slip ratio of the particular wheel, U is the adhesion friction, which is a function of wheel slippage and vehicle speed shown in equation (3.22), N_i is the normal force and α is the road slope angle. Typical $U(S_i)$ curves for various road surfaces are shown in next section (see Figure 3.5). Slippage is defined as follows

$$S_i = \frac{V\omega_i - V_i}{Max(V\omega_i, V_i)} \qquad i = lf, rf, lr, rr \tag{3.15}$$

where $V\omega_i$ is the linear speed of the wheel (measured at its outer periphery) and V_i is

the linear speed of the center of the wheel. In order to simplify that imagine a vehicle is on an extremely slippery icy road and by applying high acceleration, the wheels will spin fast, however the vehicle is not moving as fast as the wheel does. Therefore, the linear speed of the wheels, $(V\omega_i)$, will be some value and the linear speed of the center of the wheel will be a very low value close to zero since the vehicle has very low speed at that instant of time.

Using equation (3.15), the slippage can be calculated as 1 in this specific case. Under normal conditions the slippage ratio is normally small and remains in stable region.

In case of vehicle moving straight (while the steering wheel angle is zero), equation (3.10) will be rewritten as follows.

$$M\frac{dV}{dt} = \Sigma Fr_i - F_a \qquad\qquad i = lf, rf, lr, rr \tag{3.16}$$

Equation (3.17) shows air drag force.

$$F_a = \frac{1}{2}C_d\rho V^2 \tag{3.17}$$

where C_d is the drag factor (a function of the vehicle geometry and the frontal area of the vehicle), and ρ is the air density.

3.3 Mathematical Model of the Vehicle During Cornering

In this section the mathematical model of a vehicle during turning is developed. This model will be used to design and develop an electronic differential as will be described later in this section. The model is valid for front, back, and all-wheel electronic differential. Vehicle longitudinal dynamic equations will be used to examine and verify the motor drive and electronic differential model.

Figure 3.2 shows the geometry of a vehicle during cornering. The ground speed of the center of each wheel can be obtained based on the vehicle ground speed (measured at point X in Figure 3.2). The following equations show the ground speed of each wheel as a function of the ground speed (V) at point X, and the geometric parameters of the turn.

$$V_{lf} = \frac{R_{in}}{R}V,\ V_{rf} = \frac{R_{out}}{R}V,\ V_{lr} = \frac{d}{R}V,\ V_{rr} = \frac{(d+W)}{R}V \tag{3.18}$$

The linear speed of the wheel and its angular velocity are as shown in equation (3.19).

$$\omega_i = \frac{V\omega_i}{r} \qquad i = lf, rf, lr, rr \tag{3.19}$$

In equation (3.19) ω_i and $V\omega_i$ are angular and linear speed of each wheel, and r is radius of the wheels.

It is necessary to notice the difference between $V\omega_i$ and V_i as shown in Figure 3.4. If the slippage is neglected, $V\omega_i$ and V_i will be equal. In this section the slippage is

neglected since in this design acceleration and deceleration are very small, excessive slippage will not occur. Slippage will be explained in the next section and its effects on traction systems will be elaborated.

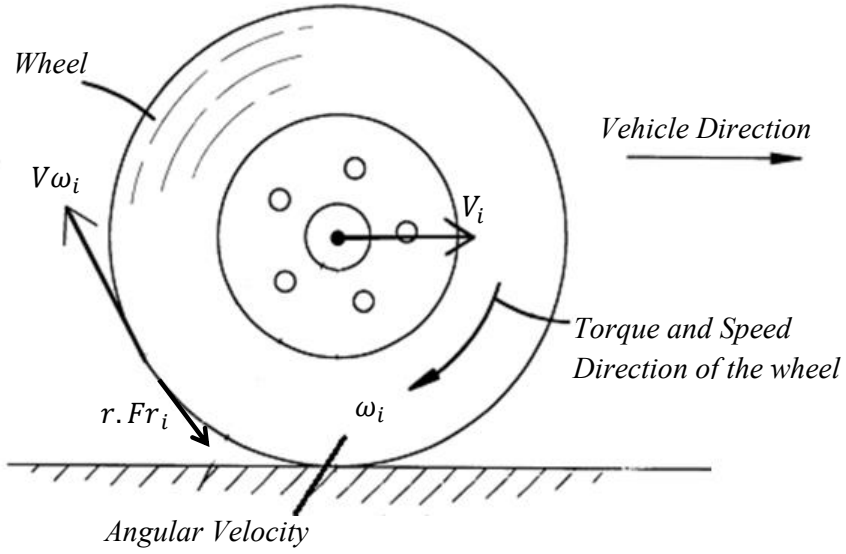

Figure 3.4: Wheel and related parameters

Expressions for ω_i can be obtained in terms of the vehicle ground speed, V, and other vehicle parameters. From Figure 3.2 note that

$$d = \frac{L}{\tan\theta} - \frac{W}{2} \tag{3.20}$$

where θ is the steering wheel angle. Since θ is measured continuously, a continually calculated value of d is available. If d is known, by considering Figure 3.2, and using geometric equations, R_{out}, R_{in}, and R can be obtained. Based on equations (3.18), (3.19), and (3.20), the following equation can be extracted.

$$V_i = f_i(\theta)V \tag{3.21}$$

It can be implied that equation (3.21) is same as equation (3.18). This equations states that the linear speed of each individual wheel is known and is a function of steering wheel angle and vehicle speed. Note that steering wheel angle is function of time. Therefore, f is a function that is responsible to continuously calculate the four speed references of the wheels by sensing steering wheel angle. Considering wheel slippage this equation must be modified, as will be shown in the next section in equation (3.24).

3.4 Inclusion of Wheel Slippage

When a vehicle moves on the surface of a road, the wheels may turn at a certain angular velocity; however the actual linear velocity of the vehicle may be somewhat lower. This is due to the slippage of the wheels, which does not fully translate to forward motion of the vehicle. In extreme cases, the vehicle may remain stationary while its wheels spin in place. There are different tire friction models, which can be used and are available in different literatures [41, 42]. They provide the tire-road adhesion friction as a function of the wheel slippage and the vehicle linear speed, V. Equation (3.22) shows one of the commonly-used equations used to obtained the adhesion friction. Coefficient C_1, C_2, C_3 are shown in Table 3.1 and C_4 is equal to 0.04 in this thesis [43]. Note that the coefficient used in this equation are not unique and they change based on different road conditions.

$$U(S_i, V) = [C_1(1 - e^{-C_2 S_i}) - C_3 S_i] e^{-C_4 S_i V} \tag{3.22}$$

Slippage can be positive or negative. It is positive during acceleration and negative during deceleration (braking). The slippage curves during deceleration are obtained by odd symmetry rules from the curves shown in Figure 3.5. During acceleration $\max(V\omega_i, V_i)$ will be $V\omega_i$ and ΣFr_i in equation (3.16) will be positive to help the vehicle accelerate. Equation (3.23) continuously evaluates slip ratio by measuring steering wheel angle, vehicle speed and angular velocity of each wheel. This equation can be obtained using equations (3.15) and (3.21).

$$S_i(t) = 1 - \frac{V_i(t)}{V\omega_i(t)} = 1 - \frac{V.f_i(\theta)}{V\omega_i(t)} \tag{3.23}$$

As seen in Figure 3.4, $V\omega_i$ and V_i are different because of the slippage. Considering the above, there will be four independent slip ratios for the four wheels, S_{lf}, S_{rf}, S_{lr} *and* S_{rr}, which are slip ratios of left front, right front, left rear and right rear wheels, respectively. As an example for left front wheel, during the acceleration $Max(Vw_{lf}(t), V_{lf}(t))$ is equal to $Vw_{lf}(t)$ and, on the other hand, during deceleration $Max(Vw_{lf}(t), V_{lf}(t))$ is equal $V_{lf}(t)$. In the first case both the slip ratio and adhesion friction are positive, so the waveforms are in first quadrant. In the second case, however, both the slip ratio and the adhesion friction are negative, i.e., the waveforms are in third quadrant. The curves in Figure 3.5 are obtained using (3.22) with parameter values listed in Table 1. Given the curves in Figure 3.5 one can maximize the output torque to each wheel while the consumed power by each motor is minimized. The main goal is to keep the slip ratios in the stable regions. The stable region is the rising side of the curves in Figure 3.5, before the adhesion friction reaches its maxi-

mum; beyond this point, the slippage becomes uncontrollably high while the adhesion friction drops rapidly.

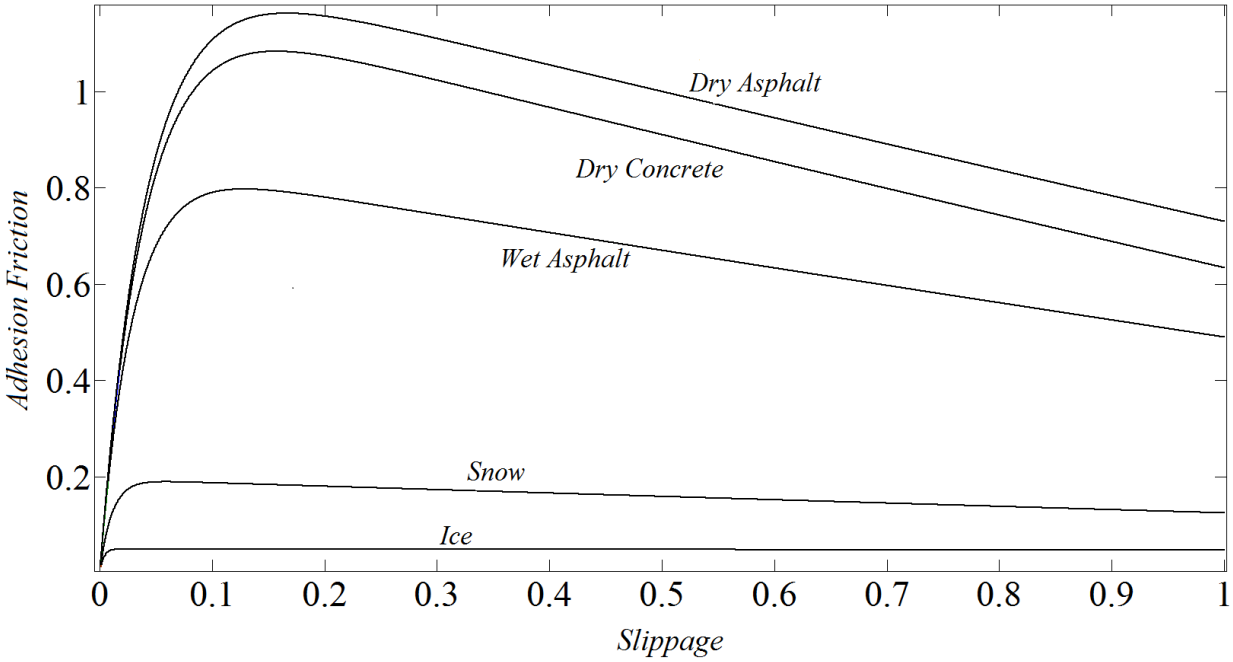

Figure 3.5: Adhesion coefficient versus slip ratio for different road conditions

Figure 3.6 shows the slippage characteristics as a function of the vehicle speed for motion of the vehicle on dry asphalt. As it is seen from this figure, the maximum adhesion friction occurs at different values of the slip ratios for different vehicle speeds. Figure 3.7 shows the slip ratios that corresponds to the maximum adhesion friction as a function of the vehicle speed. Therefore, using a look-up table, one can intricately adjust the torque commands to maintain the slip ratio that gives the maximum adhesion friction for different vehicle speed. This theory is the main idea used in this thesis to develop a robust traction control system. With consideration of the

Table 3.1: Friction model parameters and coefficients

Surface Condition	C_1	C_2	C_3
Dry asphalt	1.2801	23.99	0.52
Wet asphalt	0.857	33.822	0.347
Dry concrete	1.1973	25.168	0.5373
Snow	0.1946	94 .129	0.0646
Ice	0.05	306.39	0

slip ratios, one can re-write (3.21) as follows explicitly as a function of the slip ratio.

$$V\omega_{lf} = \frac{f_{lf}(\theta)}{1 - S_{lf}}V \tag{3.24a}$$

$$V\omega_{rf} = \frac{f_{rf}(\theta)}{1 - S_{rf}}V \tag{3.24b}$$

$$V\omega_{rb} = \frac{f_{rb}(\theta)}{1 - S_{rb}}V \tag{3.24c}$$

$$V\omega_{lb} = \frac{f_{lb}(\theta)}{1 - S_{lb}}V \tag{3.24d}$$

Note that the equations shown in (3.24) are the modified versions of the angular velocity in (3.21) with inclusion of the wheel slip. It is expected that with the inclusion of the slippage, the angular velocity of the wheels be higher than what is assumed using (3.21).

3.5 Maximizing Traction Force and Yaw Motion Control

A method for improvement of yaw motion stability of a vehicle is proposed as follows. This proposed method will not be completely verified using dynamic vehicle model in experimental setup; however, a simpler dynamic model of the vehicle is used to

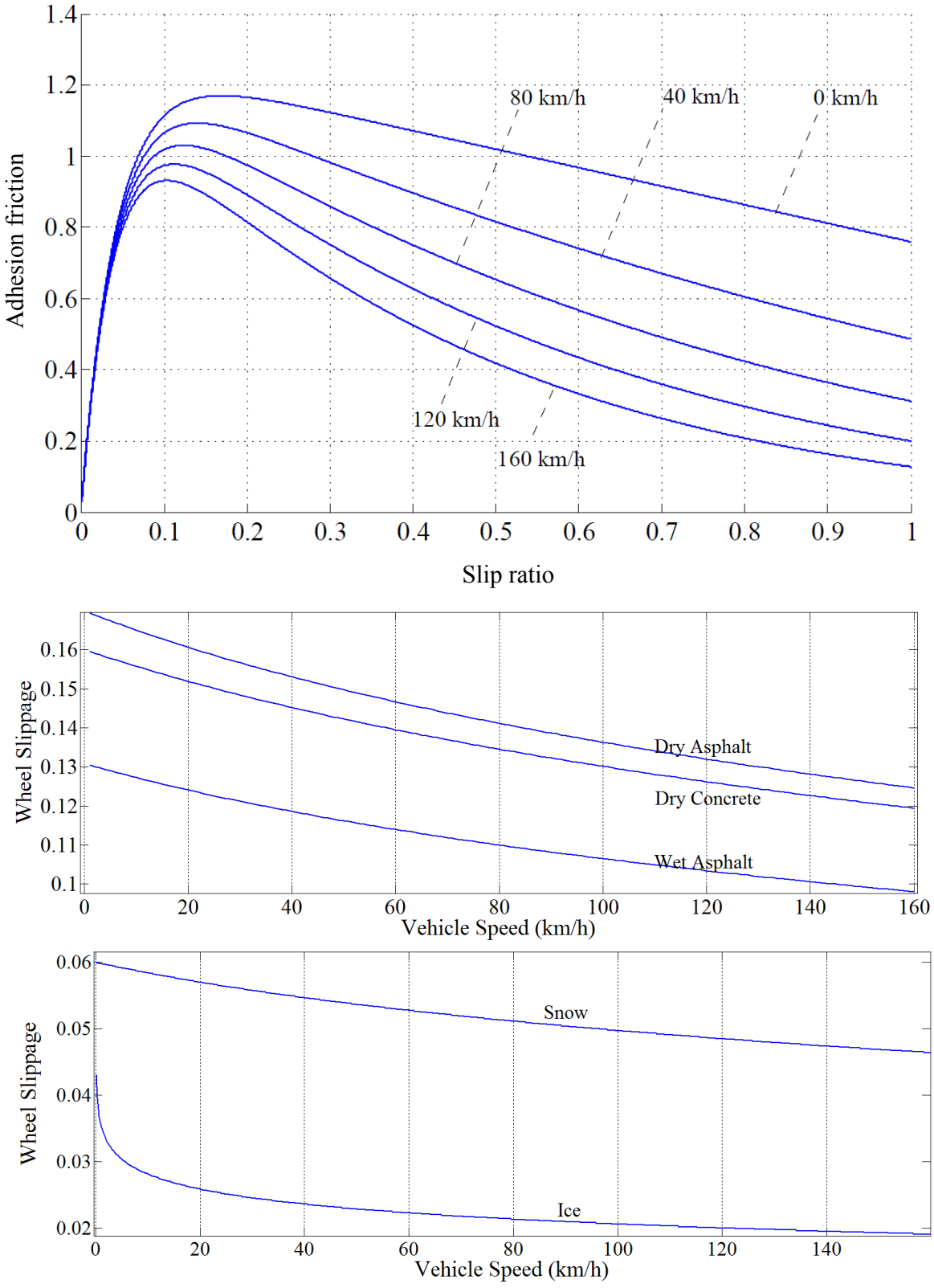

Figure 3.7: Wheel slippage corresponding to the maximum adhesion friction for different types of roads

partially verify the controller in the simulation and experimental case. The main goal in this proposed topology is to improve the motor drive and the main controller of the drive-train. First, parameters of the motion namely $\theta, T, \gamma, \omega_i$, and V are measured. θ is measured by steering wheel angle sensor. γ and ω_i will be measured by yaw rate sensor and angular speed sensor using encoders. Ground speed sensors or advance ground speed estimation methods are used to measure ground speed [21–23]. The slip ratio of each wheel is then calculated using (3.15). The desired yaw rate must also be evaluated based on the steering wheel angle (θ) and the vehicle speed (V) and other required parameters. Then the actual yaw rate is compared with the desired yaw rate to determine if corrective action is necessary.

To implement the propose yaw motion stability algorithm, the maximum allowable slippage needs to be determined using a look-up table, extracted from Figure 3.7, which is a function of the vehicle speed and road type. The four calculated slip ratios are tracked with a high-speed processor; by adjusting the torque command to the motors, the yaw motion control algorithm forces the slip ratios to remain below the optimal operating point. If the slippage of a wheel exceeds this point, the algorithm reduces the torque command to that wheel to reduce the slippage to below the optimum, and increases the torque command(s) to the wheel(s) with the lowest slip ratio. Yaw rate is considered positive if the vehicle turns counterclockwise and vice versa.

The following flowchart provides a view of the proposed yaw motion control. First, information about current slippage status for individual wheels is needed. Information from Figure 3.7 will provide the optimal slip ratio, which generates maximum torque.

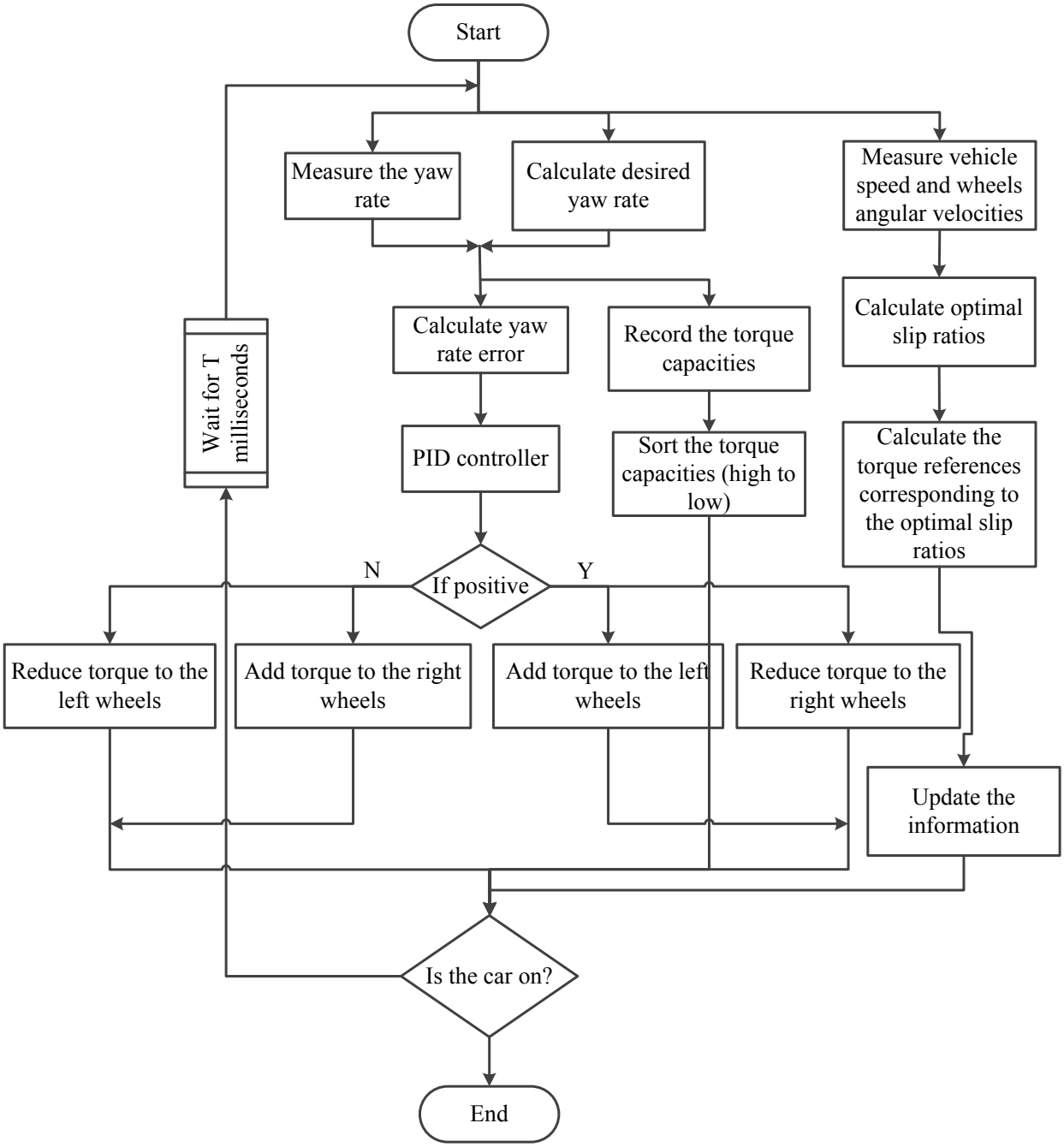

Figure 3.8: Yaw motion control strategy flow chart

Torque capacity is defined as the difference between the torque that keeps the slippage at the optimal point and the actual instantaneous torque command. In this proposed control strategy, the instantaneous torque command will never be allowed to exceed the optimum torque. As seen in Figure 3.8, yaw rate error must be obtained. This error is the difference between the measured yaw rate and the desired yaw rate. If this error is non-zero, it implies over-steering or under-steering is detected. A positive yaw rate error indicates over-steering in the counterclockwise direction. This means that the compensating yaw force must be clockwise. Therefore, torque will be added to the left wheels taking into account the torque capacities of the left wheels. If the torque capacity of either of the left wheels is close to zero, i.e. the instantaneous torque command is already close to the maximum possible torque, then torque will remain the same for that wheel. At the same time, the torque commands will be reduced to the right wheels in particular to the one with lower torque capacity. By using this strategy, firstly the yaw compensation will be fast due to the rapid response of the four electric motors. Secondly, the torque capacities of all the wheels tend to be close to each other and in the stable region. In the same way, if the yaw rate error is negative, the inverse strategy will be applied.

Chapter 4

SIMULATION RESULTS

The simulation model and results of the proposed traction control system will be presented in this chapter. For the simulation part, a vehicle model in MATLAB is created to test the proposed methods including electronic differential, traction control and yaw stability control. A motor drive controller is also simulated in PSCAD/EMTDC simulator to be tested and deployed in the real-time digital simulator (RTDS) interface software (RSCAD). Then the controller is implemented in the RTDS to verify the electronic differential method. First, a simulation case shows the functionality of the proposed electronic differential topology in the drive-train. Then the traction control system and the yaw stability control are explained and simulated.

4.1 Electronic Differential Simulation Results

A detailed computer model of a vehicle is developed and implemented (in MATLAB) to simulate the functionality of the proposed electronic differential method. The

parameters of the vehicle required for this simulation case are given in Table 4.1; these parameters pertain to an off-road vehicle. The simulations are conducted for motion on dry asphalt on a flat road. The two inputs to the model, i.e., the steering wheel angle and the traction force, are shown in Figures 4.1a and 4.1b, respectively. The latter is an indication of the command given by pressing the acceleration pedal. This traction force is the summation of four torque commands given to the four electric motors. In other words, the traction command given by the driver will be distributed between four electric motors as torque references. As explained in Chapter 3, the command given by the acceleration pedal is used by the developed electronic differential to generate four independent torque reference values to each wheel. By applying torque to the wheels, the wheel speed increases and causes a slight increase in slip ratio (see (3.15)), thereby increasing the rolling force (via (3.22) and (3.14)); the increasing rolling force increases the vehicle speed (as in (3.16)). Figure 4.2a shows four torque references for four wheels and as shown, when the steering wheel angle increases the four resulting wheel speed will have different values. Figure 4.2b shows the slippage of each wheel. Since the outer wheels need more torque, they will operate on higher slip ratio to create more rolling force and higher speed. Figure 4.2c shows the linear speed of wheels, as they follow the torque commands. Outer wheels have higher speed than inner wheels as expected.

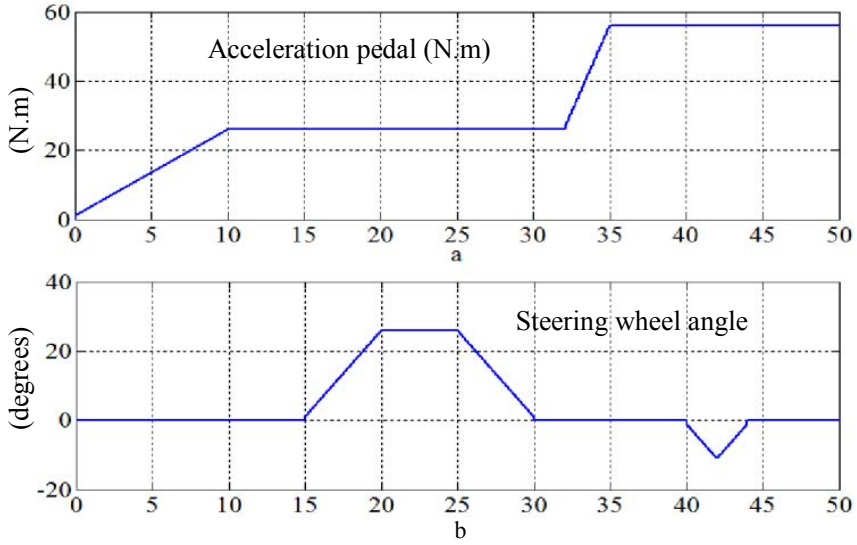

Figure 4.1: Electronic differential simulation results (input parameters)

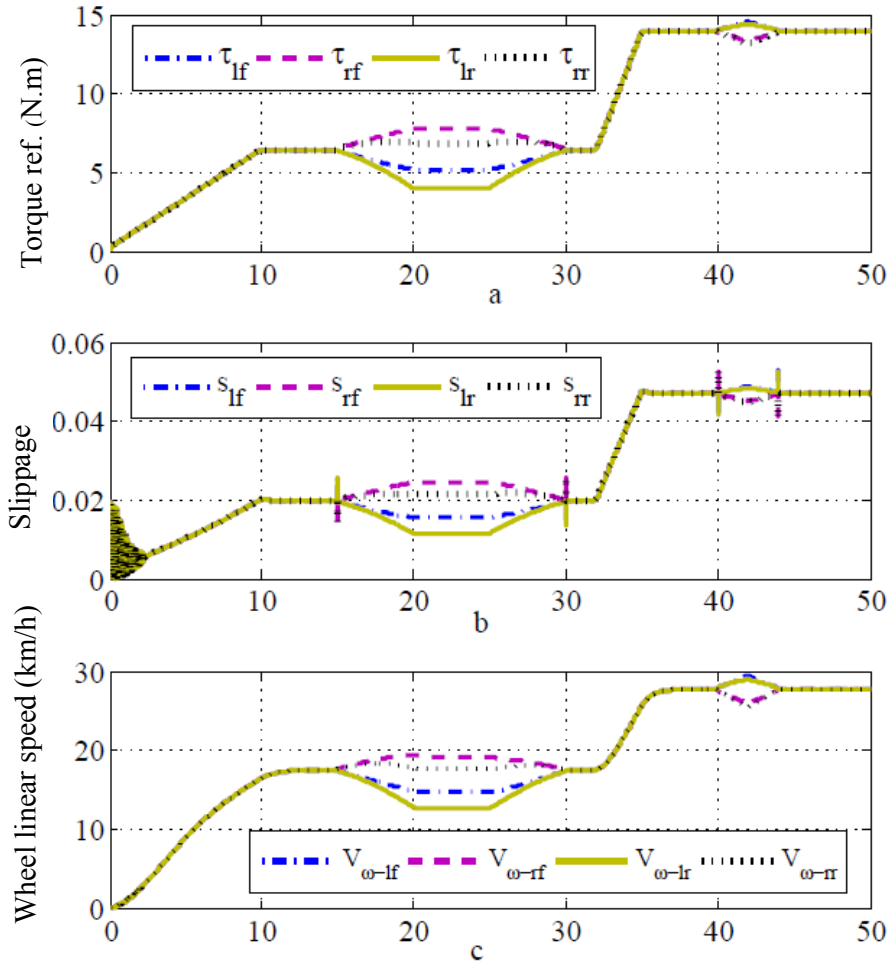

Figure 4.2: Electronic differential simulation results (output parameters)

Table 4.1: Vehicle parameters

Vehicle Length	1.94 m	Width	1.27 m
Mass	800kg	Wheel radius	0.25 m
Wheel moment of inertia	1 $kg.m^2$	Steering wheel gear	20
Air drag coefficient	1.5		

4.2 Traction Control Simulation Cases

Two simulation cases have been chosen to present the idea of the traction control system. Situations similar to these two cases may occur while driving on icy and snowy roads.

4.2.1 Start-up Traction Optimization on Snowy Road

This section illustrates the simulation case that uses the traction control system proposed in this thesis. It explains how it is possible to prevent slippage and excessive power consumption, especially on snowy and icy roads and during high rates of acceleration. As it was explained before, when slippage occurs, the wheels use excessive power without applying enough rolling force to the vehicle. In that case the slip ratio will be higher than the optimal slip ratio. This simulation case is performed with the assumption that the vehicle is on a snowy road. Figure 4.3h shows the adhesion friction curve versus slip ratio for a speed of 40 km/h. In this figure, the maximum adhesion friction can be up to 0.18 and it occurs when slippage is approximately 0.045. Based on what was shown in Figure 3.7 for any vehicle speed and different types of road there will be a specific slip ratio and a maximum adhesion friction value.

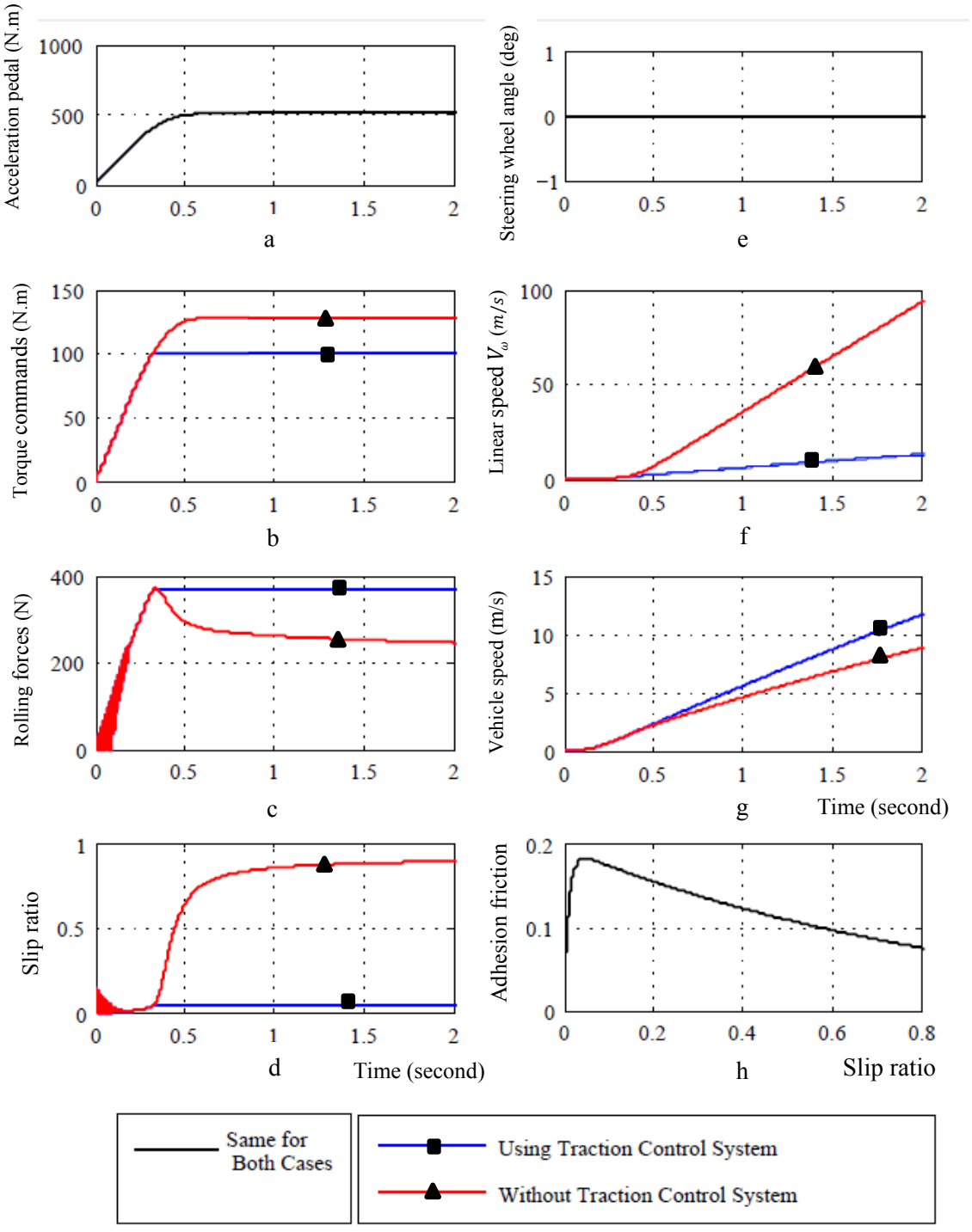

Figure 4.3: Simulation results of the slippage during start-up

Figure 4.3 shows the simulation case for two different traction systems: one that uses a regular traction control system and one with an optimized traction control sys-

tem. Curves with triangular marker (red curves) show the results of regular traction control system and curves with rectangular marker (blue curves) show the results of the optimized traction control system proposed in this thesis. All x-axes show the time except Figure 4.3h, which shows the slip ratio. Figure 4.3a shows the throttle reference for two seconds. This simulation test has been performed for start-up slippage. It is assumed that the acceleration pedal will be pushed suddenly to a high value and it applies torques to the four wheels up to 500 N. Figure 4.3e shows the steering wheel angle, which is set to zero for this simulation test. Figure 4.3b shows torque references sent to the four motors for the two cases. In regular traction control systems, the torque will be distributed equally to the four electric motors without considering slippage. In this optimized traction control system, however, the torque given to the motors have been limited to keep the slip ratios at their optimal points and maximize the traction force. In Figure 4.3d, it is seen that the slippage of the regular traction control system increases to high values and becomes unstable. On the other hand, the control system proposed in this thesis keeps the slip ratios at the optimal point. Since the vehicle speed is sensed continuously and the road type is known (snowy), using a look-up table extracted from Figure 3.7, the controller will set up a value as an optimal slip ratio. For this case the optimal slip ratio is 0.045. In Figure 4.3d the slip ratio has been limited to 0.045. Figure 4.3c illustrates that by keeping the slip ratio at its optimal point, the rolling force stays constant. This value for the rolling force (blue waveform) is the optimized rolling force for this case. Therefore, not only will the vehicle stay in the stable region, it also maximizes the vehicle's efficiency. In the red waveform, however, the slippage goes to the unstable

region and the rolling force starts dropping. Figure 4.3f shows the linear speed of the wheels for the two different controllers. The red waveform shows the wheel speed for a vehicle without the optimized traction control system and the blue one represent the linear speed in a vehicle that uses the controller proposed in this thesis. The wheel speed will increase quickly without generating forward force to the vehicle. Figure 4.3g shows the vehicle speed for the two different cases. Vehicle speed will increase faster with less power consumption by the electric motors if the optimized traction control system is used.

4.2.2 Yaw Motion Control on Snowy Road

In this section yaw motion stability control is simulated. This case uses extreme conditions of sudden change in the road type. It is assumed that the vehicle is traveling on a straight path with a constant speed on asphalt and two of the wheels suddenly transition onto the snow. Figure 4.4 illustrates this scenario.

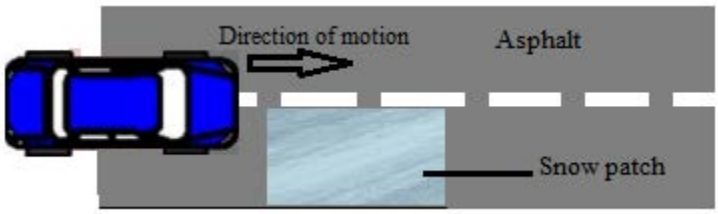

Figure 4.4: Yaw stability simulation case

In this case, the right wheels are suddenly on the snow and cannot provide as much rolling force as the left wheels. The left wheels are on wet asphalt and have higher adhesion friction. Therefore, the unbalanced forces on the left and right wheels result in the car rotating in the clockwise direction.

The following simulation case in Figure 4.5 shows what happens in this scenario.

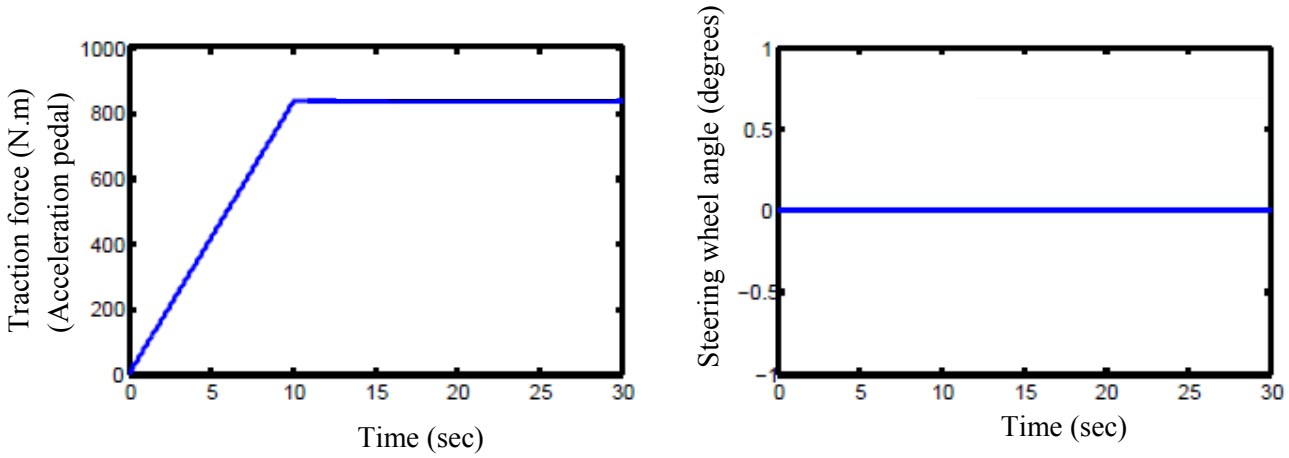

Figure 4.5: Throttle command and steering wheel angle

As it is seen, the acceleration pedal linearly increases for ten seconds after which it remains constant. The road model is designed such that at t=20 secs the two right wheels will be on the snow patch.

Figure 4.6 shows the simulation results for a vehicle with a regular traction control system. Torque references will stay the same for all wheels. The acceleration pedal will be equally divided to four to generate each wheel's torque command.

Figure 4.6c shows that slip ratios of the right wheels jump up to a value close to one, which will make the vehicle unstable. All four parts of the Figure 4.6 show that before the wheels transition to the snowy patch the vehicle is functioning well, however after that, it goes to instability i.e. the two right wheels experience excessive slippage. The results in this figure show that the vehicle will be unstable after t=20 sec and it does not analyses the vehicle performance after that time.

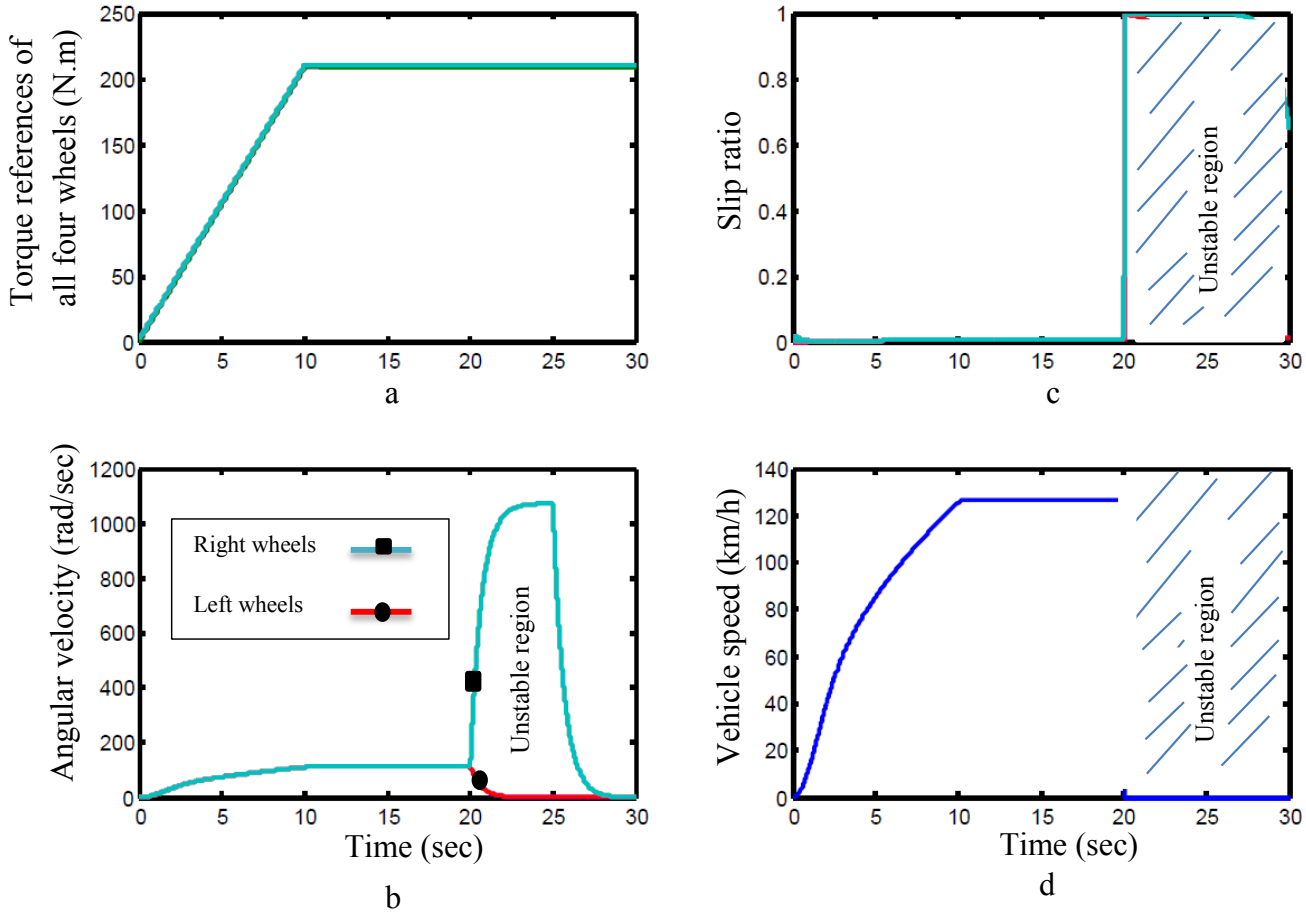

Figure 4.6: Simulation results of a vehicle without the optimized traction control system

The same scenario has been performed while the proposed optimized traction control system is used. Figure 4.7 shows the simulation results.

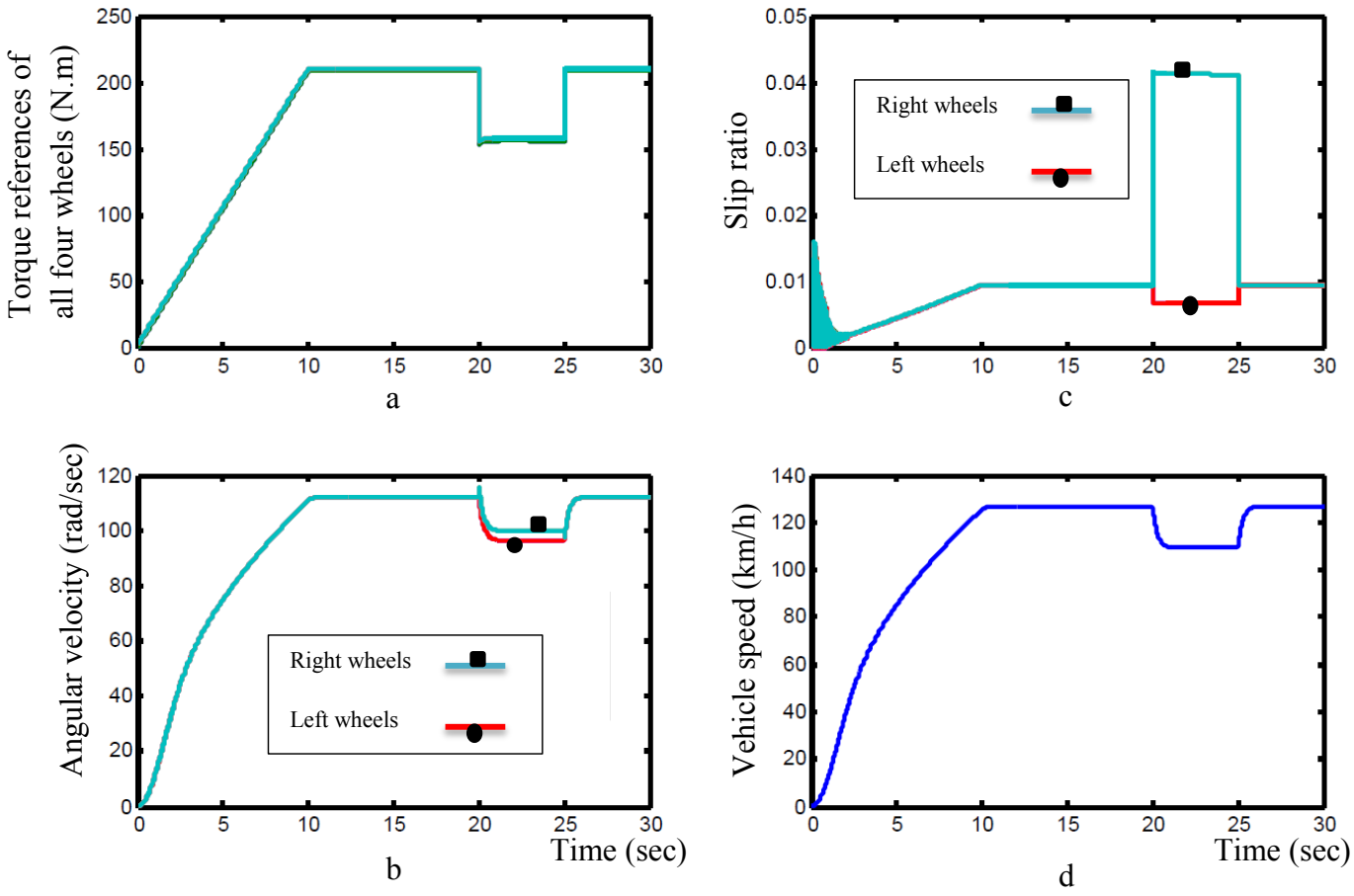

Figure 4.7: Simulation results of a vehicle with optimized traction control system

In Figure 4.7c when the right wheels go on the snow, they will start slipping because snowy road cannot provide enough friction. Therefore, the angular velocity starts increasing fast without the vehicle speeding up. Figure 4.7c shows that the slip ratios of the right wheels will stay at their optimal ratio, which in this case is equal to 0.044 for a snowy road. Figure 4.7a illustrates that by reducing the torque command the slip ratio can be kept at its optimal operating point. One may want to reduce the torque commands just for the right wheels. While that may appear to be logical, doing so, the yaw force will not be compensated and the vehicle may turn clockwise. Therefore, in order to keep the vehicle moving on a straight line, all four motors must

have the same rolling forces. Finally, since the torque commands temporarily have been reduced, the vehicle speed will be decreased for a limited amount of time (5 seconds).

Chapter 5

Experimental Implementation and Results

The experimental tests conducted are divided into two sections: (i) tests conducted on a real-time digital simulation setup for the electronic differential model proposed in this thesis, and (ii) tests performed to investigate common issues in traction control systems including excessive wheel slippage, yaw instability and, over- and under-steering. The same real-time digital simulation setup with a more advanced control system is used to examine the traction control system.

The simulation results in Section 4.1 showed the response of the developed electronic differential algorithm to the commands of steering wheel angle and traction force. In reality, the torque commands generated by the electronic differential algorithm are transmitted to the individual electric motor drive systems (for each wheel), which will then apply suitable voltages and currents to their respective motor to achieve the desired torque value. The dynamics of the electric motor drive system

were ignored in the simulation results presented earlier. In this section a small-scale laboratory setup is developed to test the performance of the proposed algorithm using an actual electric motor drive system connected to a synchronous machine, which emulates the in-wheel motor in the actual implementation of the system in a real vehicle. This experimental setup is shown in Figure 5.1.

Then, this chapter develops two different case studies of traction control systems, experiments, and compares the results with the simulation case. These two cases were simulated and presented before in section 4.2. The main goal is to examine the functionality of the proposed traction control system for different road conditions. Figure 5.7 shows the experimented setup that is developed and used in the Electric Vehicle Laboratory at the University of Manitoba. The first developed case is when a vehicle suddenly accelerates and its wheels start to slip. This case has been performed in two different conditions: (i) on the dynamometer shown in Figure 5.7, which simulates dry asphalt and (ii) when a tape is wrapped around the dynamometer to make the adhesion friction curves more similar to a snowy road rather than dry asphalt. The second case is when a wheel suddenly goes on a slippery road or when one of the wheels is suddenly off the ground for a short amount of time.

In the next sections, these experiments will be presented in greater details.

5.1 Real-Time Testing of the Electronic Differential Controller

The electronic differential algorithm is implemented on a real-time digital simulator (RTDS), which is then interfaced with the power electronics of the drive system. A field-oriented control scheme is developed, which upon receiving the torque command from the RTDS will generate proper stator current commands for the ensuing PWM switching scheme. The synchronous motor (with constant field current) responds by exerting the requested amount of torque on its shaft. This experimental setup is shown in Figure 5.1. The controller containing motor drive and electronic differential topology has been implemented in the RTDS interface software (RSCAD) [44]. Analog inputs have been used to collect speed and torque data from the dynamometer. Analog outputs that are generated by the programming software (RSCAD) are used to create two input signals: throttle command (torque command) and steering wheel angle. Using a SPWM method, RTDS provides six related pulses for the six IGBTs in a three-phase full bridge. Dead-time generator ICs have been used to protect the IGBTs. Figure 5.2 shows the PSCAD/EMTDC simulation case for the motor controller, which is used in RSCAD software to drive the motor using RTDS.

In order to see if the implemented motor drive works properly, a basic test has been performed without including the electronic differential in the motor controller system. Figure 5.3 illustrates that the motor drive produces expected performance and the motor speed rapidly follows the speed reference. The small delay in the speed response is because of the mechanical inertia of the motor, dynamometer, and the

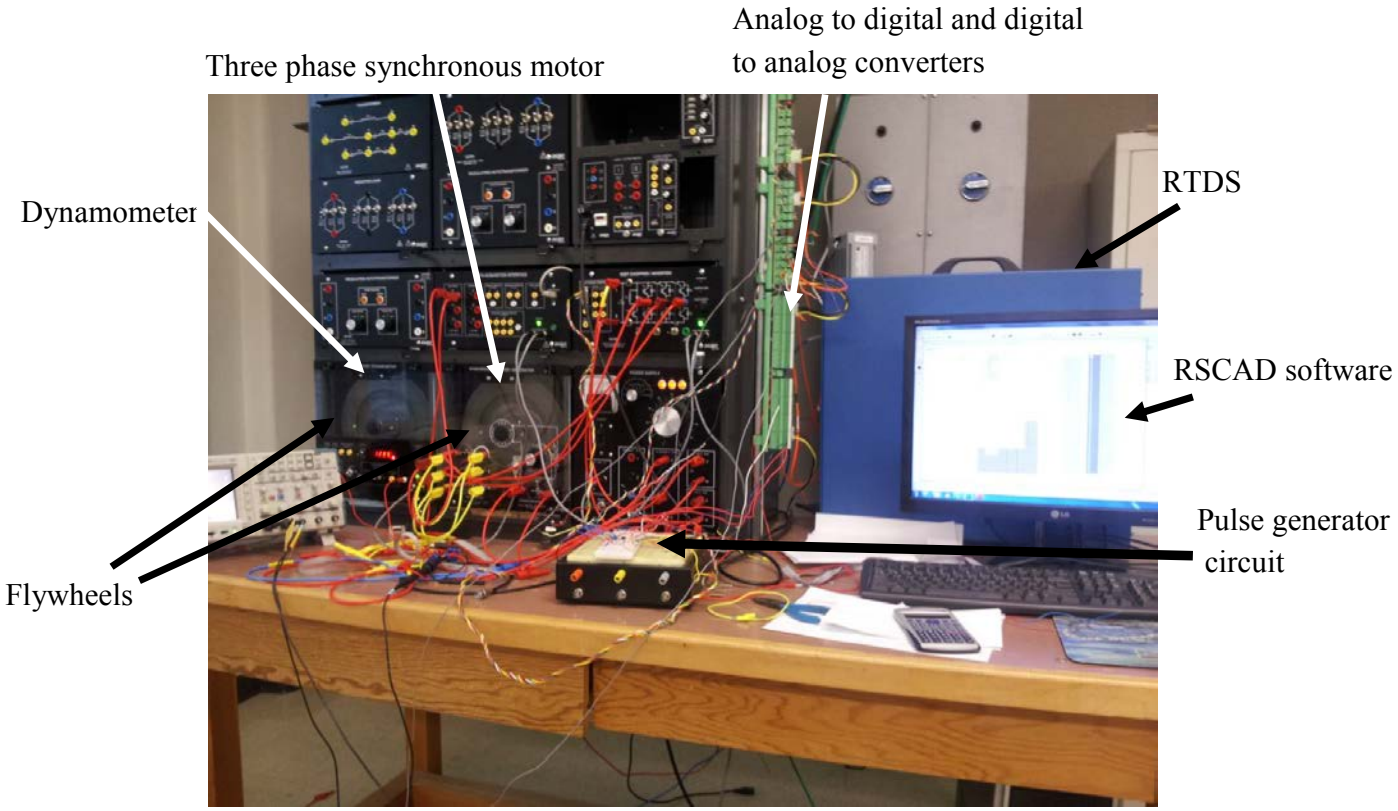

Figure 5.1: Experimental setup to test the motor drive and electronic differential

two flywheels.

Figure 5.3 shows the torque (speed) reference and the speed response of the car. This figure also illustrates the performance of the motor drive setup. As seen, the speed response of the motor is fast and it closely follows the speed command.

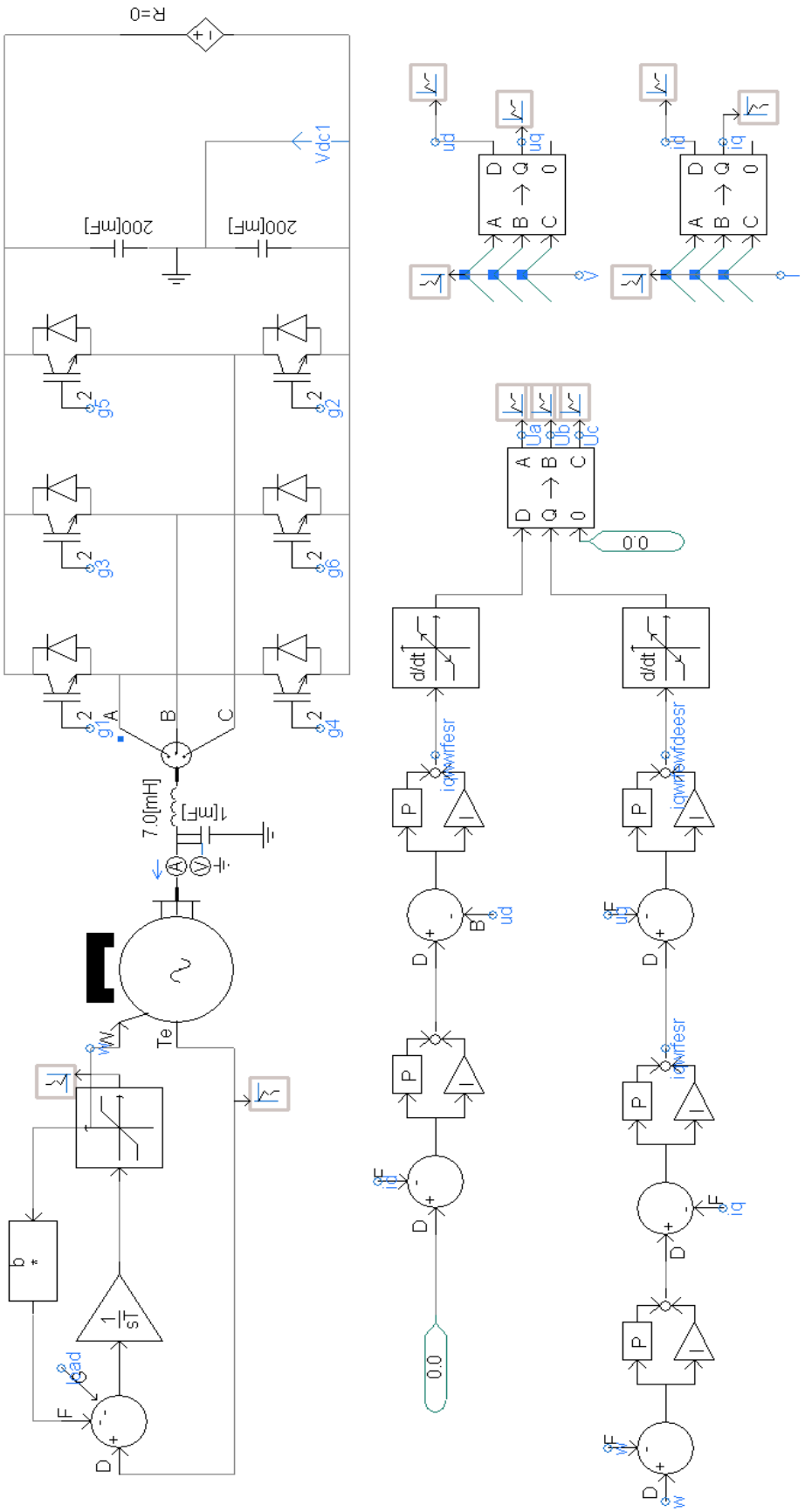

Figure 5.2: PSCAD/EMTDC simulation case of the PMSM motor drive

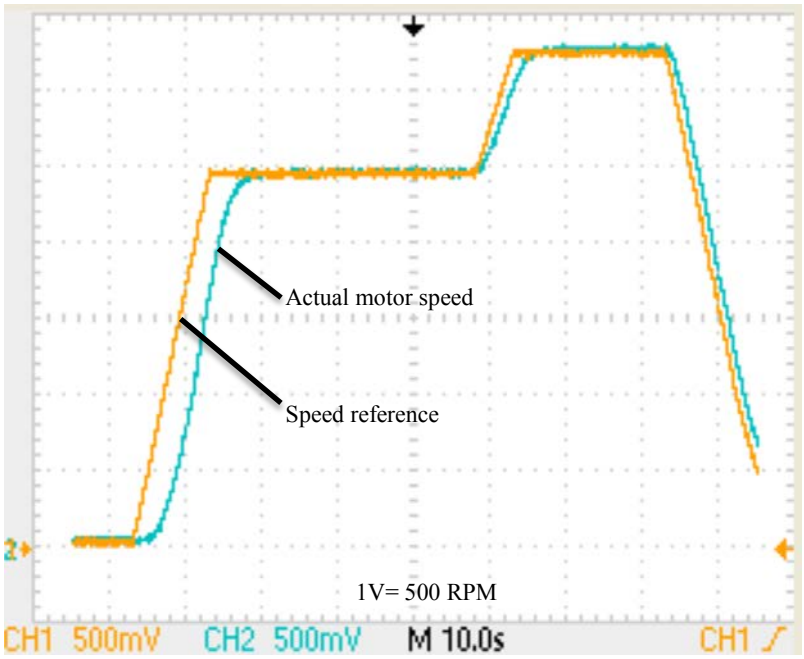

Figure 5.3: Speed reference and the motor response

Figure 5.4a shows the acceleration pedal, which is proportional to the speed reference and the steering wheel angle (input variables). Four different speed references are shown in Figure 5.4b. Although the motors are not connected to an actual vehicle, two flywheels are attached to the shafts in order to resemble the loading on the motor similar to a real vehicle.

Figure 5.5 shows the two flywheels that are connected to the dynamometer and the motor. Since the experiment is not performed in a real vehicle, the proposed yaw motion control method cannot be tested in this setup. In order to experiment with the proposed yaw motion control algorithm, one can use a lookup table extracted from Figure 3.7 to optimize the torque reference values given to the motors. A dynamometer with capability to exert different forces on the four wheels is needed to accomplish this test in an experimental setup.

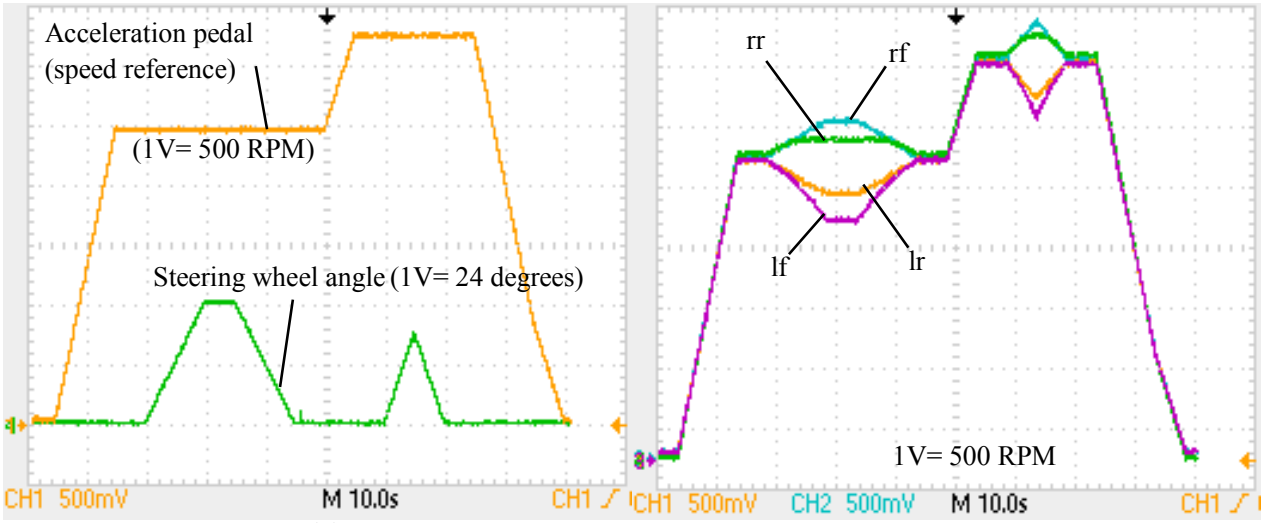

Figure 5.4: Experimental results a) speed reference and steering wheel angle (inputs) b) four different speed references of the motors

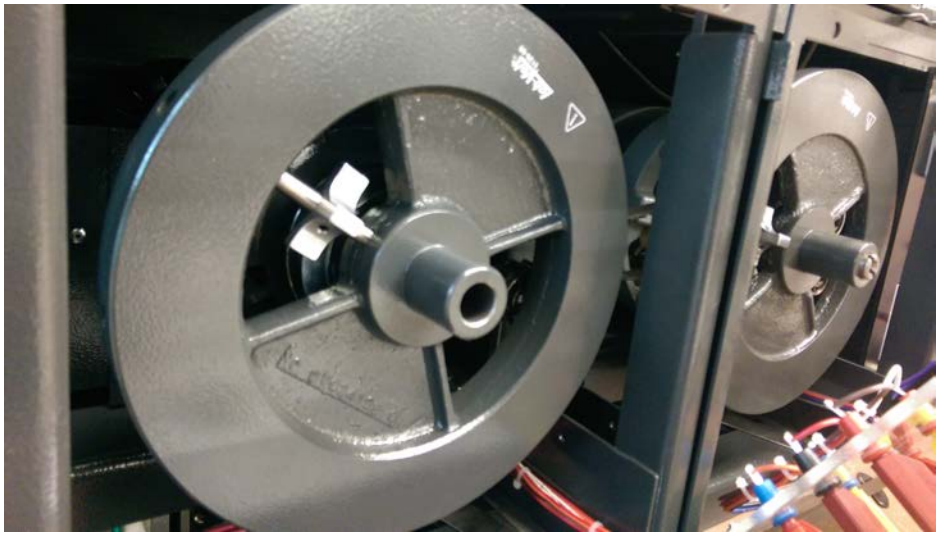

Figure 5.5: Flywheels are connected to the motor and dynamometer

Figure 5.6 shows the output currents and voltages of the three-phase inverter.

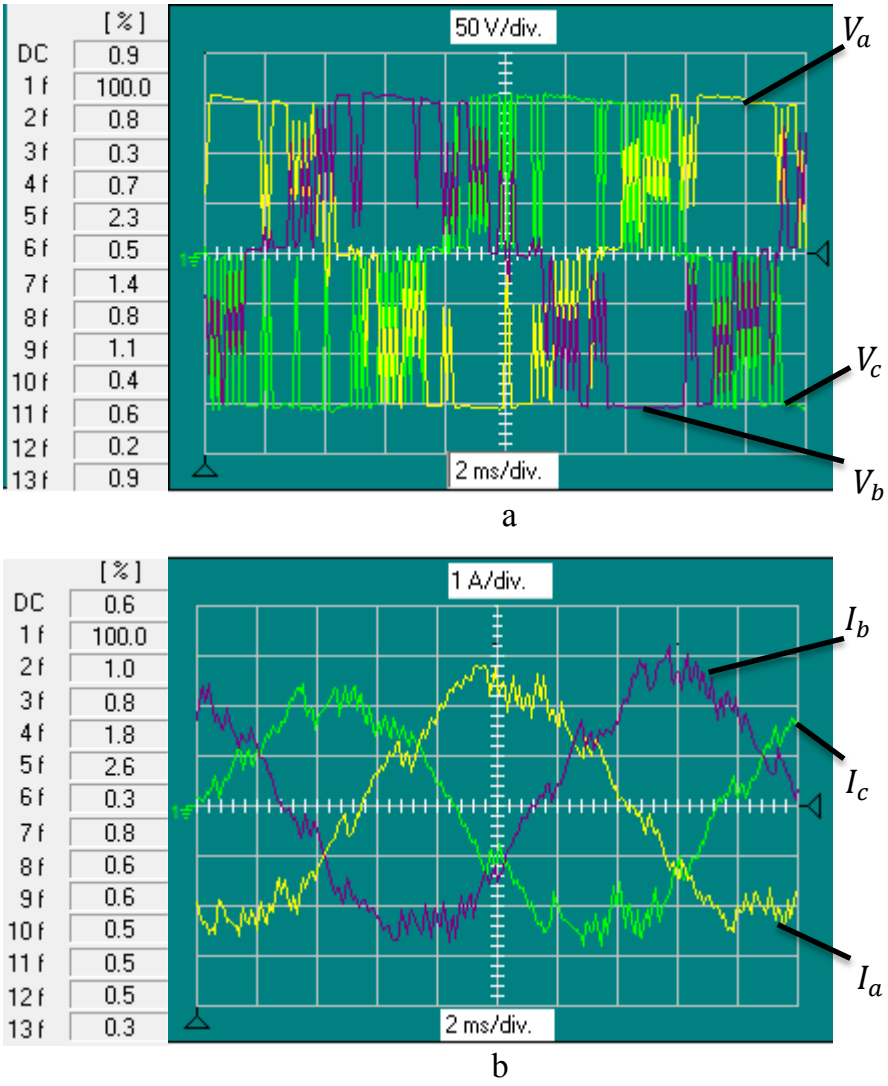

Figure 5.6: Inverter output voltages and currents

The harmonic components of voltages and currents of the stator are shown in the left hand side of each figure. The results are acceptable since undesirable harmonics are negligible. In order to control the torque and speed on the wheels, two parameters will have important roles: the voltage amplitudes and the frequencies. As seen in Figure 5.2, the only input to the motor drive is the speed reference. The speed reference will be compared to the wheel speed and passed through a speed controller

to create the quadrature current references while i_d is set to zero. These currents will be compared to i_d^* and i_q^* and they go through a voltage controller and create v_d^* and v_q^*. Using the inverse park transformation block, the V_{abc} becomes available. Note that torque is linearly proportional to quadrature current. Therefore, i_q^* can be considered as the torque reference.

5.2 Experimental Results for the Traction Control System

In this section the proposed traction control system for two common issues in vehicle stability will be presented. High rate of acceleration may cause excessive wheel slippage especially on slippery roads, which can cause vehicle instability and excessive power consumption. The optimized traction control system will prevent this by evaluating the optimal slip ratio, continuously monitoring the slippage, and optimizing the torque references for the different wheels. This test is performed for two different road types: dry asphalt and snowy road, for which plastic tape has been wrapped around the dynamometer to make it slippery. The second case study is while the vehicle is traveling with constant speed and the two right (or left) wheels transition to a snowy patch, and cause the vehicle to become unstable. In this section, this test will be performed for only one wheel. The road is supposed to suddenly change from a high friction road (asphalt) to a low friction road (snowy road). The latter case is somewhat similar to the case when on a bumpy road the normal force exerted on one of the wheels suddenly decreases or even the wheel may be lifted up (tem-

porarily off the ground) and the wheels start to spin faster with the same amount of torque exerted on them. This phenomena happens particularly in off-road trails. If the proposed controller in this thesis can limit the torque command and prevent the slippage when a wheel is suddenly lifted, it will work properly when one (or more) wheels suddenly go on a snowy, or icy patch.

Figure 5.7 shows the setup that is capable of testing and verifying the functionality of the controller for the above case studies.

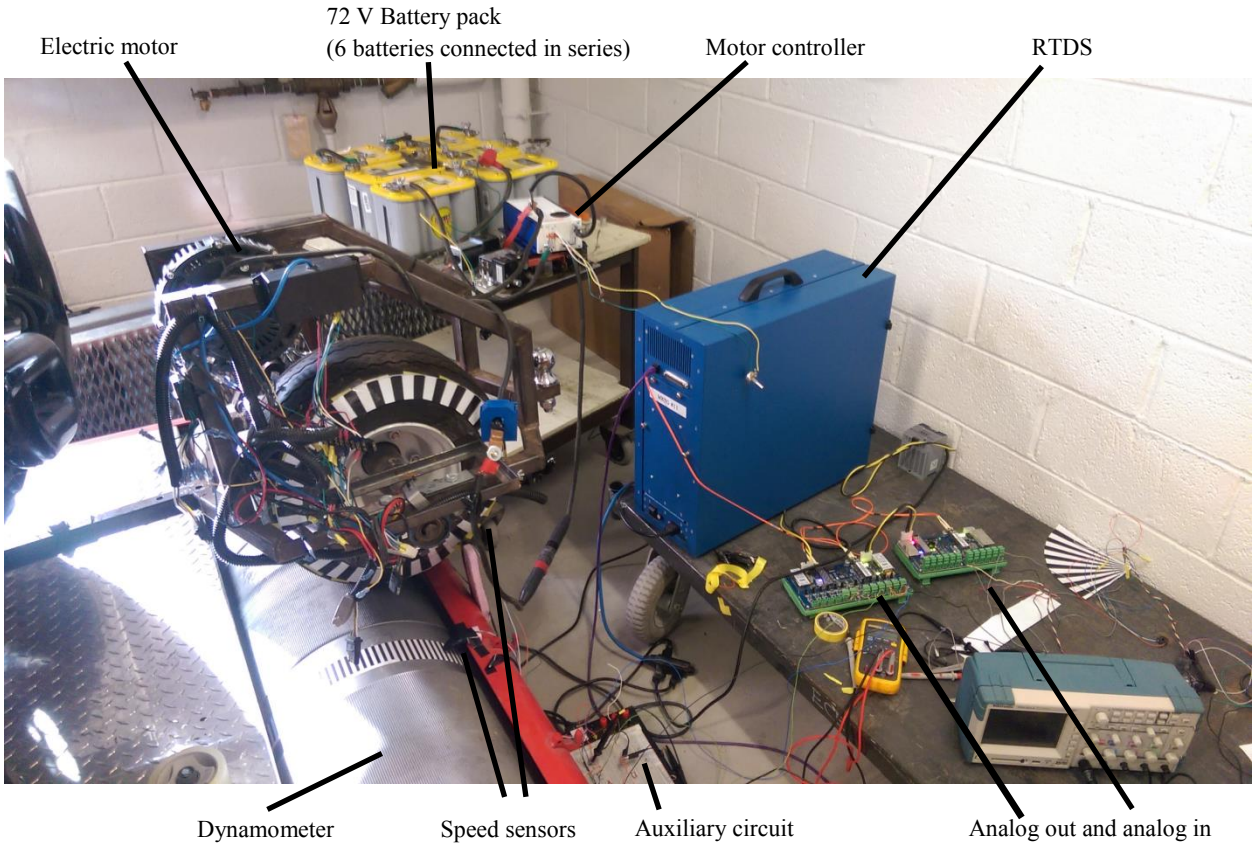

Figure 5.7: Experimental setup for the traction control system developed in the Electric Vehicle Laboratory

5.2.1 Start-up Traction Control System Experiment on Dry Asphalt

This section presents the controller response on the dry dynamometer, which is similar to dry asphalt. Figure 5.8 shows two input torque references that are given to the electric motor. One is while the regular controller is used and the other one is while the proposed optimized traction control system is used. The two torque references resemble an acceleration pedal reference.

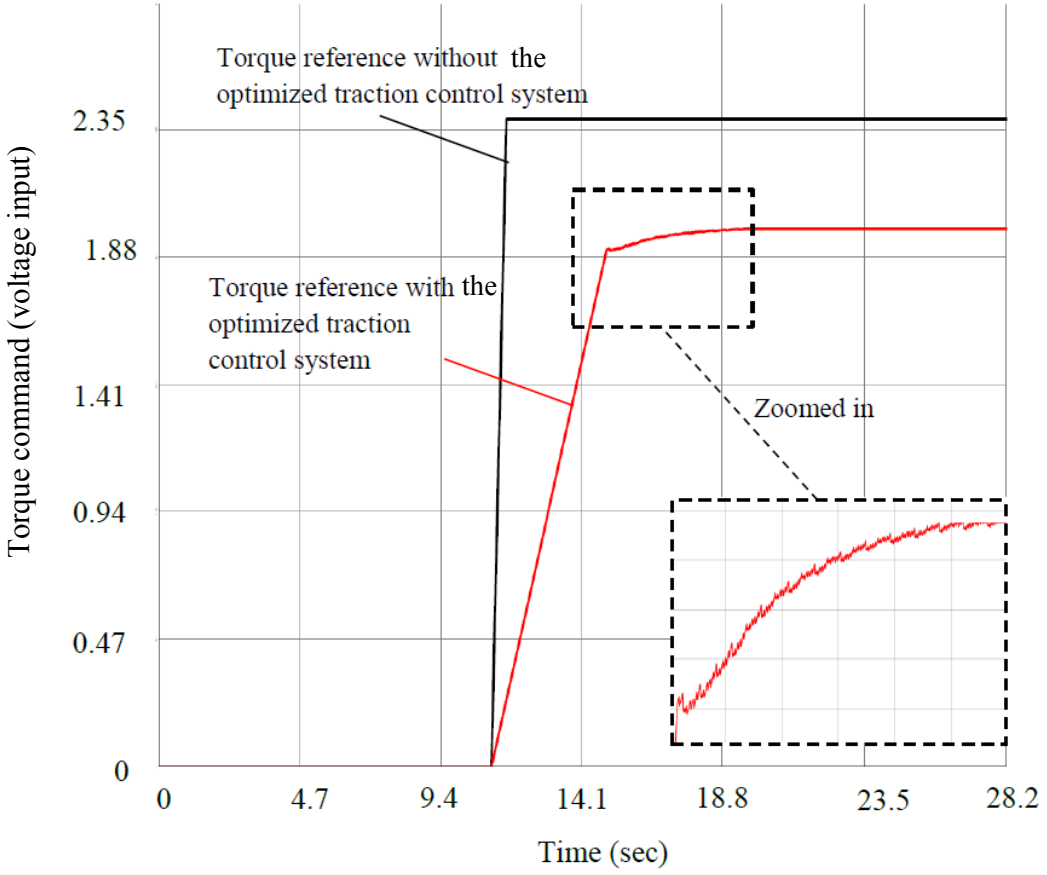

Figure 5.8: Torque reference for two different systems on the dynamometer (dry asphalt)

As shown in this figure, the input command has been limited in order to keep the

slippage close to its optimal range.

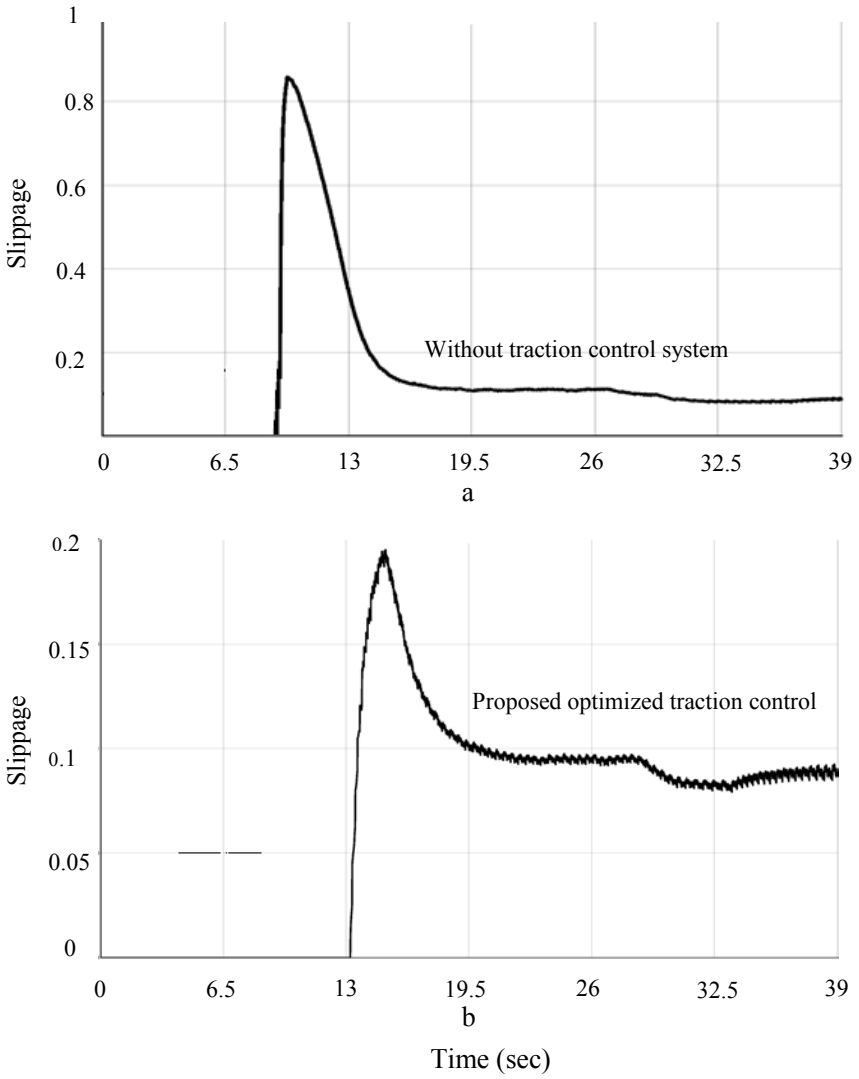

Figure 5.9: Slip ratio for two different controllers on the dynamometer (dry asphalt)

Figure 5.9a shows the slip ratio while the proposed traction control system is not used. As illustrated, after a sudden increase in the acceleration pedal, the slippage uncontrollably increases up to 88%, which is over the optimal slip ratio point. In Figure 5.9b, however, the proposed traction control system prevents the slippage from exceeding the optimal point and keeps it below 18%. Since this experiment is performed on the dry dynamometer, it can be assumed that this experiment resembles

dry asphalt. As it can be seen in Figure 3.15, for dry asphalt the optimal slip ratio that provides maximum traction force is around 16%, which is close to the results shown here.

5.2.2 Start-up Traction Control System Experiment on Snowy Road

In order to resemble a snowy road and reduce the friction on the dynamometer, a plastic tape is used to reduce the friction between the surface of the tire and the dynamometer.

Figure 5.10 shows the acceleration pedal for the system with and without the optimized traction control system. As shown, the moment the slip ratio of the wheel exceeds the stable region, the torque reference is limited and the controller will not allow the inverter to supply excessive current to the stator windings. This limitation will prevent waste of energy, damage to the tire(s), and will help to boost the stability of the vehicle.

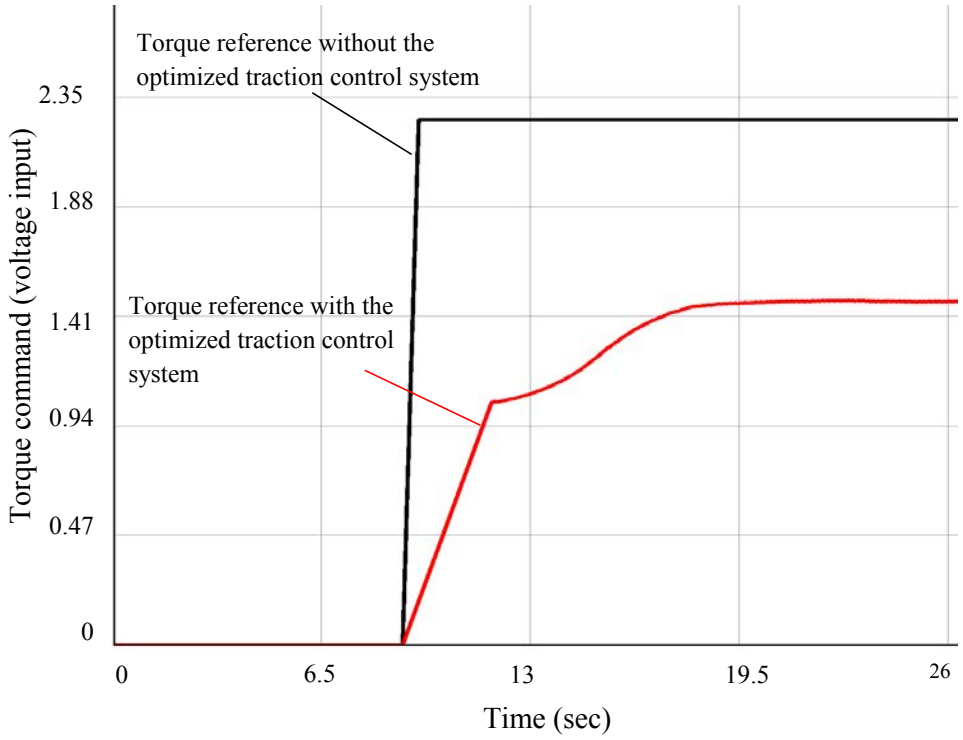

Figure 5.10: Torque reference for two different systems on a snowy road (taped dynamometer)

Figure 5.11 shows the slip ratio for the two controllers. Figure 5.11a shows the slip ratio without the traction control system. As seen, the slip ratio exceeds 90%, which is not acceptable and has several disadvantages as mentioned in the previous section. Figure 5.11b presents the slip ratio when the proposed traction control system is used. The slippage is limited and will not exceed more than 14.5%. By taking a closer look at Figure 3.15 it can be seen that the slippage has been limited to a proper amount. It needs to be pointed out that the experimental results in this part may not be as flawless as the simulation results since in the simulation results it is assumed that the adhesion friction versus slippage characteristics are available and are accurate. In the experiment, however, the adhesion friction versus slippage curves of the wheel and

the dynamometer are not available and the optimal slip ratio that corresponds to the maximum rolling force is unknown. However, it is observed that the friction versus slippage characteristics of the wheel and the dynamometer is close to the wheel and the surface of dry asphalt road and, therefore, it successfully limits the slip ratio and provides stable and smoother acceleration.

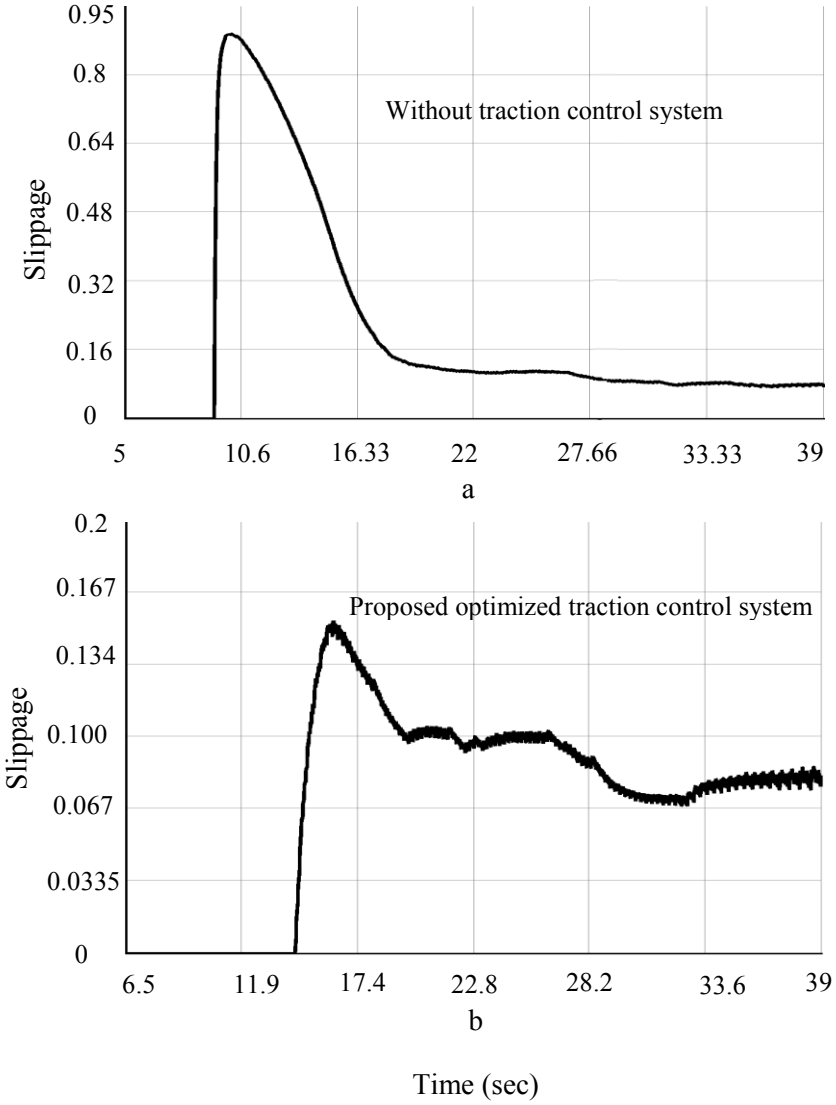

Figure 5.11: Slip ratios of two controllers on a snowy road (taped dynamometer)

5.3 Stability Control System for Sudden Changes of the Road Adhesion Friction and/or the Normal Forces Exerted on the Wheel(s)

In this section an experimental setup has been prepared to test the traction control system and verify the functionality of the proposed method to respond to sudden changes in the road conditions or the normal force exerted on the wheels. For example, one assumption could be while driving on a dry asphalt, the two right wheels go on a snowy patch in a road shoulder. This experiment is also similar to the case when the normal force exerted on each wheel suddenly decreases because of a bumpy road or on off-road trails.

The input torque reference, which is proportional to the acceleration pedal reference, is constant in this experiment. The results will be presented in two different sections: first, without the traction control system being utilized and then, the results will be presented while optimized traction control system is deployed.

5.3.1 Experimental Results without the Optimized Traction Control System

The experiments in this section are performed when the wheel is suddenly lifted. It means that the normal force exerted on the wheel suddenly decreases to zero. If the controller works properly for this scenario, it will work for other cases in which the normal force suddenly decreases to a lower rate (not lifted completely). The reason

for that is the worst case scenario of a sudden change on the friction-slippage curves is when a wheel is completely lifted up and the normal force drops to zero. Figure 5.12 shows the input acceleration pedal command and the two arrows show the moment that wheel is lifted and the moment the wheel is placed back on the dynamometer (on the ground).

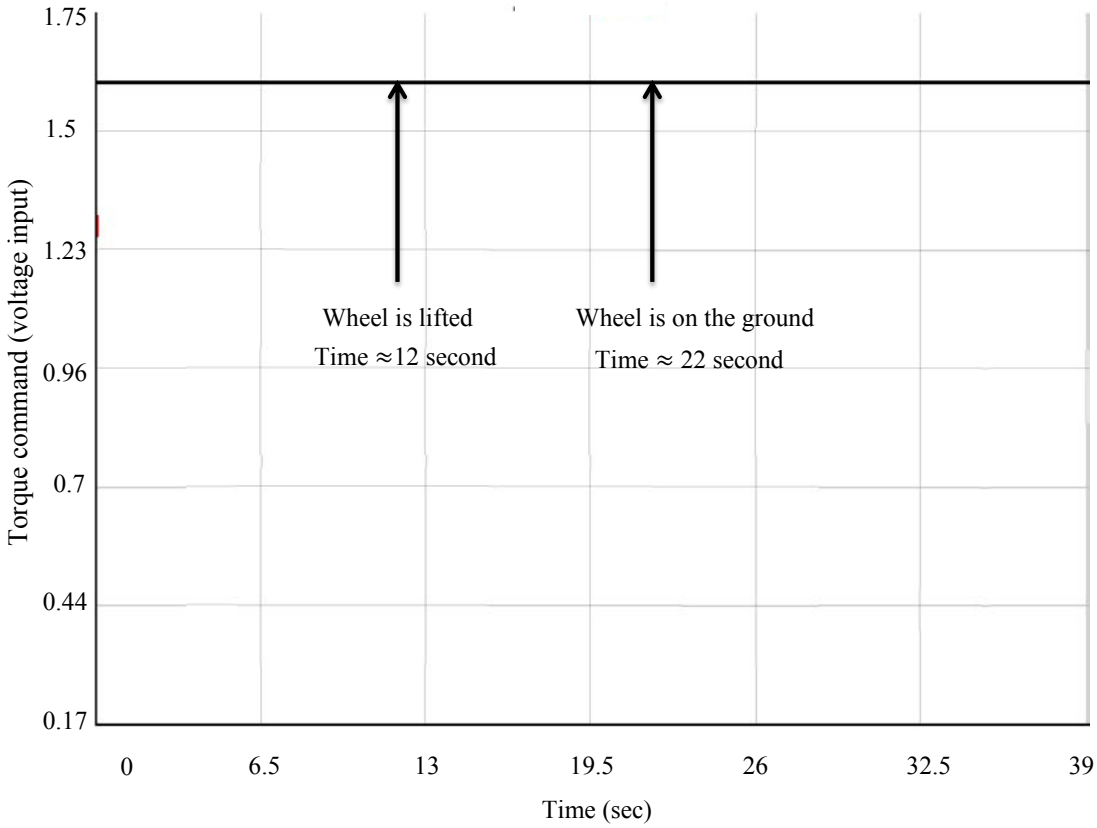

Figure 5.12: Acceleration pedal command without the optimized traction control system

Figure 5.13 shows the dynamometer and the wheel's linear speed. At approximately t=12 sec the wheel is suddenly lifted and the wheel speed rises quickly. Since there is no positive rolling force on the dynamometer, its speed decreases until the wheel is again back on the dynamometer and dynamometer's speed increases to a value close to the wheel speed. Note that the wheel's linear speed is not supposed to

match the dynamometer linear speed since their diameters are not equal. However, the angular velocities of the wheel and the dynamometer are almost equal in low rate of the wheel slippage.

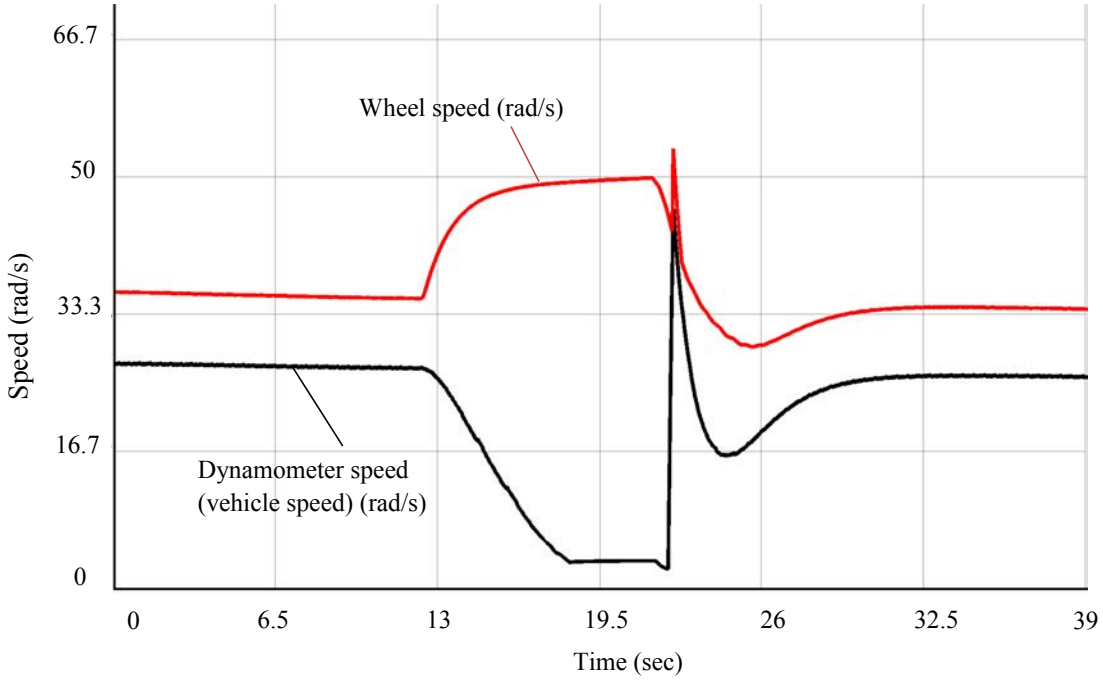

Figure 5.13: Wheel and vehicle (dynamometer)'s speed while the wheel is suddenly lifted for 10 seconds

Figure 5.14 shows the slip ratio of the wheel. As soon as the wheel is lifted the slippage rises to 93% and as seen, at t=22 sec (shown by arrow) when the wheel is placed back on the dynamometer, the slippage jumps up for a short amount of time and drops instantly to a very low value and after that stays in a stable operating slip ratio.

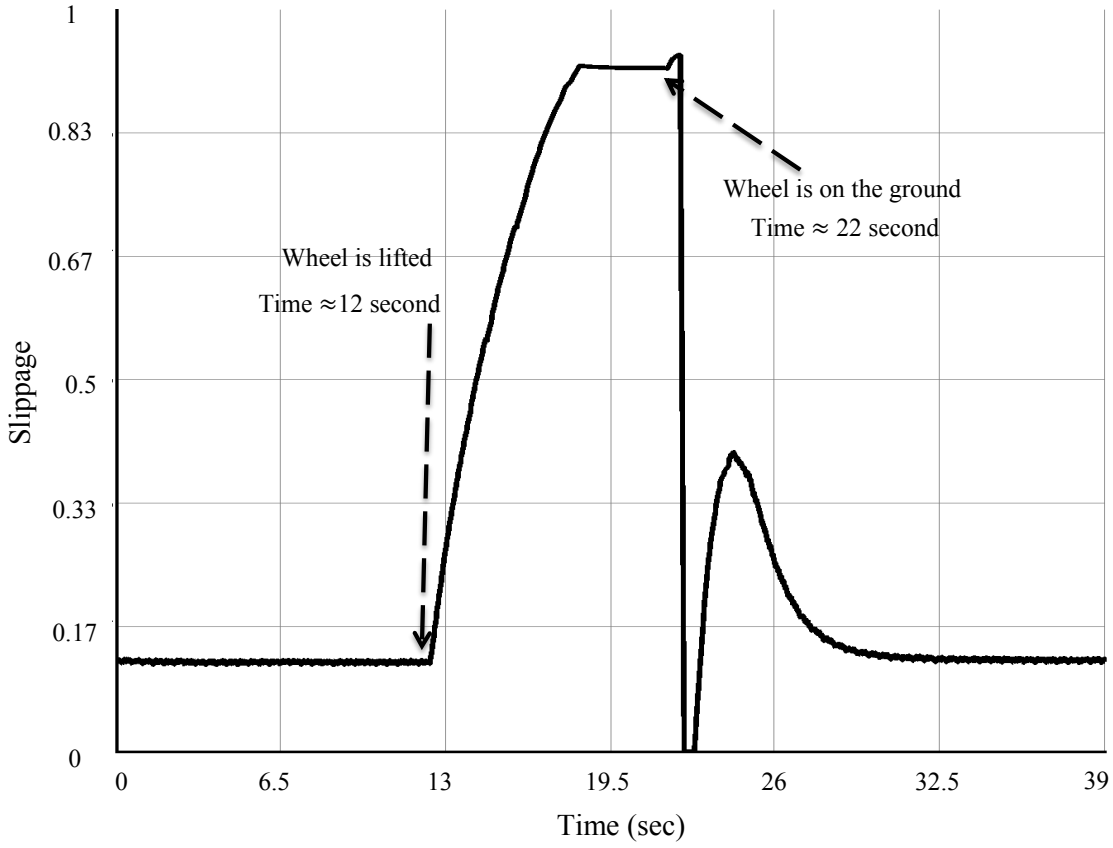

Figure 5.14: Slip ratio while the wheel is suddenly lifted for 10 seconds

These experiments illustrate that without a traction control system, by lifting the wheel, the wheel's speed quickly increases while the vehicle speed is decreasing, which may make the car unstable. But the main goal of the proposed traction control system is that when the wheel is on a slippery road or the wheel is lifted, the torque command instantly goes to lower value to prevent excessive power usage and keep the vehicle stable.

5.3.2 Experimental Results for Sudden Changes in the Road with Optimized Traction Control System

In this part experimental results will be presented while the traction control system is deployed. In this experiment the wheel is off the ground at approximately t=8 sec and it is placed back on the dynamometer at approximately t=16 sec.

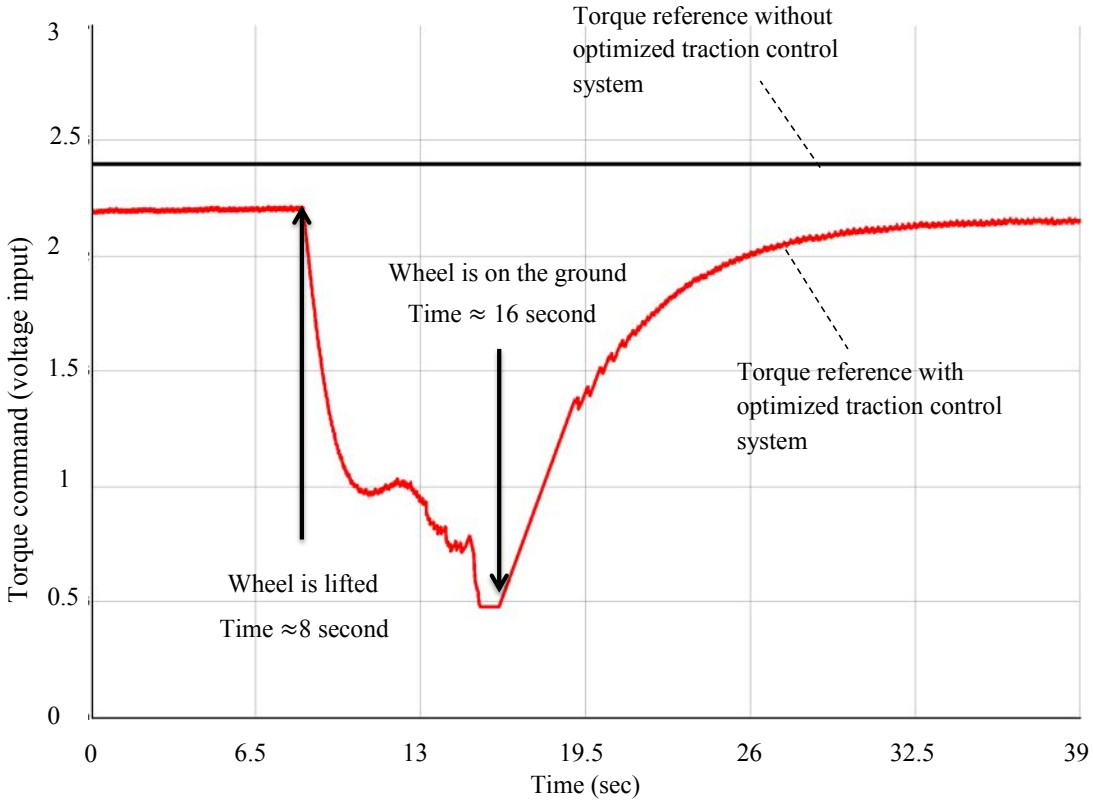

Figure 5.15: Acceleration pedal command and the controller output torque reference

As illustrated in Figure 5.15, at t=8 sec, the wheel is lifted and the output torque command instantly drops the torque reference to prevent excessive slippage and power consumption. When the wheel is back on the dynamometer, the torque reference goes back to the previous amount.

Figure 5.16 shows the linear speed of the dynamometer and the wheel. As seen, when the wheel is lifted, it tends to spin faster while the dynamometer's speed decreases. The controller reduces the torque quickly and the speed of the wheel decreases as well as the dynamometer. Then, at t=16 sec, the wheel is back on the dynamometer and the torque command is restored to the previous value and the wheel speed increases as well as the dynamometer's speed.

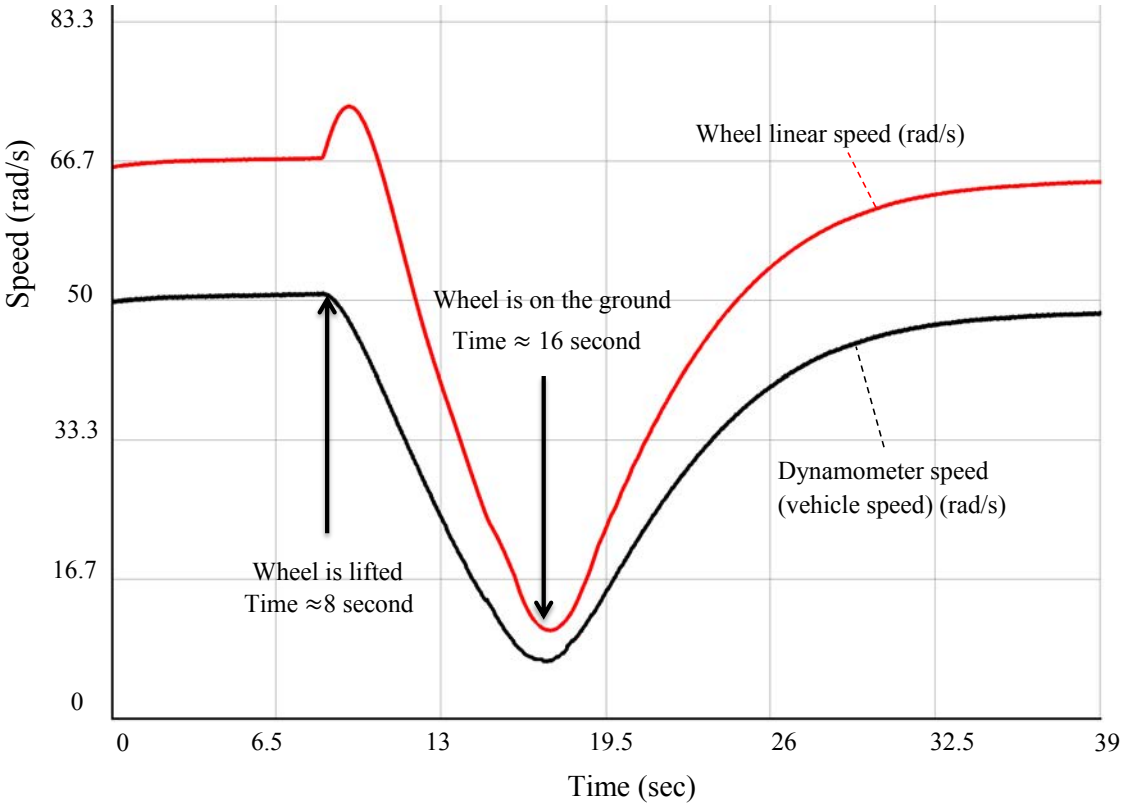

Figure 5.16: Wheel and vehicle (dynamometer)'s speed while the proposed controller is deployed

As shown in Figure 5.17 the slippage is limited and it remains less than 37% and it quickly goes back to a lower amount.

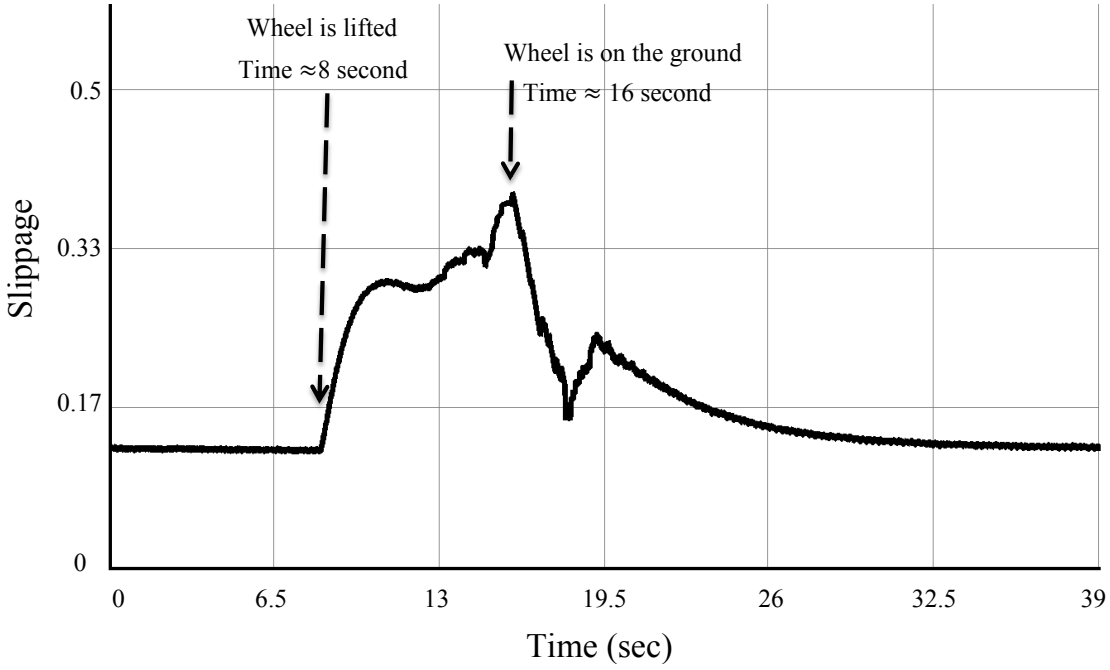

Figure 5.17: Slip ratio when the wheel is lifted for 8 seconds while the proposed controller is deployed

These case studies presented in this chapter demonstrated the results of the proposed traction control system and compared them with conventional traction system. The results illustrate that by utilizing the methods presented in this thesis, firstly, the electronic differential boosts the vehicle stability during cornering. Second, the results indicate that the same controller will limit the slippage to keep it in the stable region and prevent excessive power usage for different road conditions. Third, the results also showed that the same traction control system will limit the torque commands to the the individual wheels to limit the slippage on bumpy roads while the normal force exerted on a wheel is low.

Chapter 6

Contributions, Conclusions and Future Work

The objective of this thesis was to review and develop a robust controller for an electric vehicle drive-train with four independently controlled electric motors. The thesis investigated the main components and the performance of a typical drive-train. It explained that in order to encourage customers to use electric cars, electric vehicles' performance and price must be able to compete with ICE cars. In order to achieve this goal, any betterment in drive-train components is important and can boost the electric vehicle industry. Among different components, this thesis initially investigated two important parts of the drive-train: power electronics and motor drive and, then, in great detail, it developed a control system with several attributes.

In Section 2.2, the thesis highlighted the importance of the power electronic components in the drive-train with four in-wheel motors. Then it illustrated that by increasing the efficiency and reducing the size and the price, it significantly affects

electric vehicle drive-train performance and efficiency. In the appendix, it demonstrated a commonly used resonant converter, which has several applications in dc/dc, dc/ac, and ac/dc converters in electric vehicle drive-trains. It shows that by increasing the frequency, converters can be miniaturized. This is critical because in in-wheel technology, converters and motor controllers are built inside the hub of the motor. Motor drive controller is also another unit that was investigated by modeling, simulating and real-time digital simulation testing. Real-time digital simulation cases showed fast and accurate response for the motor drive, which is a crucial factor for designing the proposed traction control system.

It was shown that during cornering, the four wheels will have different speeds and, therefore, they require different torque commands. This chapter presents the main contribution of this thesis and demonstrates the major applications of the proposed methods in electric vehicle industry. Then it concludes the thesis by presenting certain limitation of in-wheel electric vehicle and the proposed traction control system. In the future work, the idea of implementing the proposed methods in a vehicle will be presented.

6.1 Contribution

The contributions of this thesis are mainly on different aspects in a drive-train with four in-wheel electric motors and the advantageous and challenges associated with them. Even though there is significant research conducted in the area of electric vehicles, a fully-electric vehicle with four in-wheel electric motors is fairly a new

concept. The following specific contributions have been made in this thesis:

A. A motor drive controller was simulated in PSCAD/EMTDC simulator and implemented in RTDS. Although the field-oriented control method is a proven concept, however, in this part, this thesis presented a combination of this commonly-used method and the proposed electronic differential topology. It was shown that it is fairly simple to design a reliable electronic differential using mathematical equations and include it in the existing controller.

B. In order to improve power electronic converters in an electric vehicle, this thesis studied, modeled, and developed dc/ac and dc/dc resonant converters, which is presented in the appendix. It was mentioned that soft-switching is not a new concept and there are different topologies in the existing literature. However, this resonant converter is specifically designed and developed for vehicular applications. In order to exemplify this, one must note that in order to use in-wheel motors and dc/ac inverter inside the wheel, the motor drive and converter must be as small as possible to be built into the hub of the wheels. By increasing the switching frequency to range of MHz, the passive elements will be significantly reduced. It makes the system more efficient, cheaper and smaller. The developed dc/ac and dc/dc converters have significant applications in ac/dc fast charging of the batteries, boost up/down of the dc voltage, and converting dc to ac voltage for driving ac motors.

C. In Chapter 3, design of a basic motor controller that includes the electronic differential system was explained. This section mentioned that there are different topologies for electronic differential in literature and they have used different vehicle

dynamics models. This thesis utilized geometry of the vehicle to extract the desired equations to design a controller containing the electronic differential. It clearly showed that adding the electronic differential topology to the existing controller, the drive-train creates a reliable and acceptable performance during cornering. This topology was modeled and simulated using MATLAB and implemented in RTDS. Both the simulation and experimental results prove the validity of the control method.

D. Chapter 3 continued by defining the slippage and its effects on the rolling force of the individual wheels. This showed that there is an unstable region for the rolling force versus slippage characteristic. In other words, increasing the slippage after a certain point, the rolling force of the tire will be reduced. This part showed that this method prevents the wheel to go in the unstable region and also proposed a topology to limit the torque command when the slippage reaches to its optimal point. Although, negative slippage (during braking) is not discussed in detail in this thesis, however, the same concept works for braking systems. In anti-lock braking systems (ABS), brake is applied and released several times per second and prevents the wheel slip ratio from surpassing the optimal slip ratio. The traction control method introduced in this thesis is different since it does not apply the mechanical brake several times. Instead, it applies negative torque to the wheels by recovering its kinetic energy. This negative torque keeps the slippage remain close to the optimal point that gives the maximum negative traction force. In braking system, both torque and slip ratio are negative and their characteristics are obtained by the odd symmetry rules from the curves shown in Figure 3.5

E. Another appealing concept presented in this chapter is combining the traction control method with the yaw motion stability control. Section 3.3 illustrated how it is possible to use an advanced traction control system and apply yaw stability control into it (Figure 3.8). Although this proposed method was not implemented in an actual vehicle, it demonstrated considerable improvements that can be achieved.

F. In simulation cases and experimental results, this thesis examined the traction control system in greater detail. It demonstrated that the proposed controller not only contains an electronic differential built in it, it also provides two important attributes for the traction system: (i) it increases the stability of the vehicle when the road condition suddenly changes on certain wheels and/or when the normal force exerted on a wheel is suddenly reduced, and (ii) it prevents excessive slippage during sudden acceleration. This method works for all different road conditions and restrains the slippage to the optimal slip ratio.

6.2 Conclusions

One of the issues in this scheme was that the available adhesion friction curves versus slippage may not be accurate. In other words, in this thesis it is assumed that the adhesion friction coefficients presented in Table 3.1 already exist and are precise. Further improvement may be needed to keep the slippage at the optimal operating point even by varying road conditions. A possible method is that to identify whenever the slippage starts to go to the unstable region and the controller limits the torque regardless of the road condition. These further improvements can be done with es-

timation of slippage sudden changes. As shown in Figure 3.15, when the slippage passes the optimal point, slippage increment will be faster while rolling force will be reduced. This fact can help one to design an advance controller to sense the slip ratios and prevent excessive slippage regardless of the road type. Moreover, in this thesis it is assumed the ground speed of the vehicle is continuously measured and is accurate. When using two in-wheel motors for front(rear) wheels, measuring ground speed would be easier by measuring the speed of rear(front) wheels. However, in case of using four in-wheel motors it could be challenging to have an accurate ground speed measurement. Experimental results developed in this thesis verified the performance of the proposed algorithm. Since all experiment tests were performed on a single wheel, it restrains the verification of the yaw stability control method.

6.3 Future work

This thesis studied an all-electric vehicle with four independently-controlled electric motors and then investigated its traction control system. To develop an electric vehicle with the proposed traction control system and increase the performance and reliability of the traction control system, the following items need to be tested and they are recommended as future direction for this subject.

A. Four permanent magnet synchronous motors should be provided and installed in a vehicle. As it is explained in Section 2.2.1, it is critical to utilize a robust ac motor controller to drive the electric motors. PMSM vector control was explained and developed in Section 3.1 and its experimental results were illustrated in Chapter 5.

This control strategy should be used in the motor drive controllers to independently drive four ac motors.

B. This thesis laid the foundation for three main important parts in traction systems. It firstly designed and developed an electronic differential to control all wheels independently. Secondly, it introduced slippage and adhesion friction. Then, it proposed a method to maximize traction control and minimized energy wasted in the motors during high rate of slip ratios. Finally, it combined the two above methods and presented a topology to increase the vehicle stability in slippery road and off-road trails. These three main subjects should be programmed in a controller such as the field programmable gate array (FPGA). The mathematical model for electronic differential can be converted to machine language and compiled with FPGA controller. The topology explained in Section 3.4 and included equations and the look up table extracted from Figure 3.7 must be given to the controller. Moreover, a high level programing language must be used to program the flowchart that is shown in Figure 3.8.

C. A resonant converter developed and presented in the appendix can be used in the electric vehicle drive-train and in ac/dc fast charger. A high power and high current ac/dc resonant converter should be used to charge the batteries. The aim of this high frequency charger is to have high efficiency, smaller size, and ability to carry high current. The advantage of the resonant converter developed in this thesis is that it can be controlled and programmed in the same FPGA board. Therefore, the main controller board can manage the ac/dc charger as well as the other converters and

power management systems. It is notable that some modifications must be made to the existing resonant converter such as rated power, rated frequency, and the devices that have been used.

References

[1] I. T. Forum., "Transport outlook, meeting the needs of 9 billion people," online, www.internationaltransportforum.org/Pub/pdf/11Outlook.pdf, pp. 5. Year: 2011.

[2] A. T. van Zanten, "Bosch esp systems: 5 years of experience," SAE, 2000-01-1633.

[3] J. S. E. K. Liebemann, K. Meder and G. Nenninger, "Safety and performance enhancement: the bosch electronic stability control (esp)," sAE 2004-21-0060.

[4] M. Zeraoulia, M. E. H. Benbouzid, and D. Diallo, "Electric motor drive selection issues for hev propulsion systems: A comparative study," *Vehicular Technology, IEEE Transactions on*, vol. 55, no. 6, pp. 1756–1764, 2006.

[5] A. Haddoun, M. E. H. Benbouzid, D. Diallo, R. Abdessemed, J. Ghouili, and K. Srairi, "A loss-minimization dtc scheme for ev induction motors," *Vehicular Technology, IEEE Transactions on*, vol. 56, no. 1, pp. 81–88, 2007.

[6] J. Faiz, M. B. B. Sharifian, A. Keyhani, and A. B. Proca, "Sensorless direct torque control of induction motors used in electric vehicle," *Energy Conversion, IEEE Transactions on*, vol. 18, no. 1, pp. 1–10, 2003.

[7] H.-D. Lee, S.-J. Kang, and S.-K. Sul, "Efficiency-optimized direct torque control of synchronous reluctance motor using feedback linearization," *Industrial Electronics, IEEE Transactions on*, vol. 46, no. 1, pp. 192–198, 1999.

[8] S. R. Cikanek and K. E. Bailey, "Regenerative braking system for a hybrid electric vehicle," oct 2 2003, uS Patent 20,030,184,152.

[9] A. Hajihosseinlu, M. Jahanmahin, E. Afjei, and S. Tajik, "A novel four layer switch reluctance motor with high torque and ripple reduction," in *Power Electronics and Drive Systems Technology (PEDSTC), 2012 3rd.* IEEE, 2012, pp. 62–67.

[10] P. Pillay and R. Krishnan, "Modeling, simulation, and analysis of permanent-magnet motor drives. i. the permanent-magnet synchronous motor drive," *Industry Applications, IEEE Transactions on*, vol. 25, no. 2, pp. 265–273, 1989.

[11] J. M. Miller, "Power electronics in hybrid electric vehicle applications," in *Applied Power Electronics Conference and Exposition, 2003. APEC'03. Eighteenth Annual IEEE*, vol. 1. IEEE, 2003, pp. 23–29.

[12] C. Chan and K. Chau, "Power electronics challenges in electric vehicles," in *Industrial Electronics, Control, and Instrumentation, 1993. Proceedings of the IECON'93., International Conference on*. IEEE, 1993, pp. 701–706.

[13] Z. Amjadi and S. S. Williamson, "Power-electronics-based solutions for plug-in hybrid electric vehicle energy storage and management systems," *Industrial Electronics, IEEE Transactions on*, vol. 57, no. 2, pp. 608–616, 2010.

[14] A. Emadi, Y. J. Lee, and K. Rajashekara, "Power electronics and motor drives in electric, hybrid electric, and plug-in hybrid electric vehicles," *Industrial Electronics, IEEE Transactions on*, vol. 55, no. 6, pp. 2237–2245, 2008.

[15] A. Hajihosseinlu, S. Filizadeh, G. Bistyak, and E. Dirks, "Electronic differential design for a vehicle with four independently controlled in-wheel motors," in *Electric Vehicle Conference (IEVC), 2014 IEEE International*. IEEE, 2014, pp. 1–7.

[16] S.-i. Sakai, H. Sado, and Y. Hori, "Motion control in an electric vehicle with four independently driven in-wheel motors," *Mechatronics, IEEE/ASME Transactions on*, vol. 4, no. 1, pp. 9–16, 1999.

[17] J. Kim and H. Kim, "Electric vehicle yaw rate control using independent in-wheel motor," in *2007 Power Conversion Conference-Nagoya*, 2007, pp. 705–710.

[18] J. Kim, C. Park, S. Hwang, Y. Hori, and H. Kim, "Control algorithm for an independent motor-drive vehicle," *Vehicular Technology, IEEE Transactions on*, vol. 59, no. 7, pp. 3213–3222, 2010.

[19] F. J. Perez-Pinal, I. Cervantes, and A. Emadi, "Stability of an electric differential for traction applications," *Vehicular Technology, IEEE Transactions on*, vol. 58, no. 7, pp. 3224–3233, 2009.

[20] Y. Chen and J. Wang, "Design and evaluation on electric differentials for over-actuated electric ground vehicles with four independent in-wheel motors," *Vehicular Technology, IEEE Transactions on*, vol. 61, no. 4, pp. 1534–1542, 2012.

[21] M. Lobur, Y. Darnobyt, and R. Kryvyy, "Methods of car speed measurement based on doppler's effect," in *CAD Systems in Microelectronics (CADSM), 2011 11th International Conference The Experience of Designing and Application of*. IEEE, 2011, pp. 394–396.

[22] L. Cocco and S. Rapuano, "Accurate speed measurement methodologies for formula one cars," in *Instrumentation and Measurement Technology Conference Proceedings*, 2007, pp. 1–6.

[23] K. Kobayashi, K. C. Cheok, and K. Watanabe, "Estimation of absolute vehicle speed using fuzzy logic rule-based kalman filter," in *American Control Conference, Proceedings of the 1995*, vol. 5. IEEE, 1995, pp. 3086–3090.

[24] I. T. Forum, "Hybrid cars,protean electric," online, available: http://www.proteanelectric.com/index.html. [Accessed: 2012].

[25] J. Hu, A. D. Sagneri, J. M. Rivas, Y. Han, S. M. Davis, and D. J. Perreault, "High-frequency resonant sepic converter with wide input and output voltage ranges," *Power Electronics, IEEE Transactions on*, vol. 27, no. 1, pp. 189–200, 2012.

[26] L. Zhu, "A novel soft-commutating isolated boost full-bridge zvs-pwm dc–dc converter for bidirectional high power applications," *Power Electronics, IEEE Transactions on*, vol. 21, no. 2, pp. 422–429, 2006.

[27] J. G. Hayes, M. G. Egan, J. Murphy, S. E. Schulz, and J. T. Hall, "Wide-load-range resonant converter supplying the sae j-1773 electric vehicle inductive charging interface," *Industry Applications, IEEE Transactions on*, vol. 35, no. 4, pp. 884–895, 1999.

[28] D. J. Perreault, J. Hu, J. M. Rivas, Y. Han, O. Leitermann, R. C. Pilawa-Podgurski, A. Sagneri, and C. R. Sullivan, "Opportunities and challenges in very high frequency power conversion," in *Applied Power Electronics Conference and Exposition, 2009. APEC 2009. Twenty-Fourth Annual IEEE.* IEEE, 2009, pp. 1–14.

[29] I. Husain, "Electric and hybrid electric vehicles fundamental," Second Edition, cRC Press, Chapter 9.

[30] W. Jiang, L. Tao, K. Tsang, and N. CHEUNG, "Differential algebraic observer-based nonlinear control of pmsynchronous motor [j]," *Proceedings of the Csee*, vol. 2, p. 017, 2005.

[31] Wikipedia, "Range anxiety," Retrieved online, March, 2015.

[32] Y.-P. Yang and T.-H. Hu, "A new energy management system of directly-driven electric vehicle with electronic gearshift and regenerative braking," in *American Control Conference, 2007. ACC'07.* IEEE, 2007, pp. 4419–4424.

[33] J. Yao, Z. Zhong, and Z. Sun, "A fuzzy logic based regenerative braking regulation for a fuel cell bus," in *Vehicular Electronics and Safety, 2006. ICVES 2006. IEEE International Conference on.* IEEE, 2006, pp. 22–25.

[34] X. Liu, Q. Zhang, and C. Zhu, "Design of battery and ultracapacitor multiple energy storage in hybrid electric vehicle," in *Vehicle Power and Propulsion Conference, 2009. VPPC'09. IEEE.* IEEE, 2009, pp. 1395–1398.

[35] J. Cao, B. Cao, Z. Bai, and W. Chen, "Energy-regenerative fuzzy sliding mode controller design for ultracapacitor-battery hybrid power of electric vehicle," in *Mechatronics and Automation, 2007. ICMA 2007. International Conference on*. IEEE, 2007, pp. 1570–1575.

[36] M. Ortúzar, J. Moreno, and J. Dixon, "Ultracapacitor-based auxiliary energy system for an electric vehicle: Implementation and evaluation," *Industrial Electronics, IEEE Transactions on*, vol. 54, no. 4, pp. 2147–2156, 2007.

[37] website : "public.asu.edu", "Ultracapacitor," Retrieved online, March, 2015.

[38] T. Motors, "Increasing energy density means increasing range." (Online Article) 2012.

[39] Wikipedia, "Energy density," Retrieved online, March, 2015.

[40] M. Abe, "Vehicle handling dynamics , theory and applications," Book, chapter 7.

[41] J. Wong, "Theory of ground vehicles," Book, John Wiley and Sons, 2nd ed, 1993.

[42] F. Gustafsson, "Monitoring tire-road friction using the wheel slip," *Control Systems, IEEE*, vol. 18, no. 4, pp. 42–49, 1998.

[43] M. Oudghiri, M. Chadli, and A. Hajjaji, "Robust fuzzy sliding mode control for antilock braking system," *International Journal on Sciences and Techniques of Automatic Control*, vol. 1, no. 1, pp. 13–28, 2007.

[44] R. Technologies, "www.rtds.com/the-simulator/our-software/about-rscad/," online, retrieved March 2015.

[45] I. Batarseh and C. Lee, "High-frequency high-order parallel resonant converter," *Industrial Electronics, IEEE Transactions on*, vol. 36, no. 4, pp. 485–498, 1989.

[46] S.-C. Wong and A. D. Brown, "Analysis, modeling, and simulation of series-parallel resonant converter circuits," *Power Electronics, IEEE Transactions on*, vol. 10, no. 5, pp. 605–614, 1995.

[47] M. K. Kazimierczuk, N. Thirunarayan, and S. Wang, "Analysis of series-parallel resonant converter," *Aerospace and Electronic Systems, IEEE Transactions on*, vol. 29, no. 1, pp. 88–99, 1993.

[48] S.-A. El-Hamamsy, "Design of high-efficiency rf class-d power amplifier," *Power Electronics, IEEE Transactions on*, vol. 9, no. 3, pp. 297–308, 1994.

[49] D. C. Hamill, "Impedance plane analysis of class de amplifier," *Electronics Letters*, vol. 30, no. 23, pp. 1905–1906, 1994.

[50] H. Koizumi, T. Suetsugu, M. Fujii, K. Shinoda, S. Mori, and K. Iked, "Class de high-efficiency tuned power amplifier," *Circuits and Systems I: Fundamental Theory and Applications, IEEE Transactions on*, vol. 43, no. 1, pp. 51–60, 1996.

[51] P. Imbertson and N. Mohan, "Asymmetrical duty cycle permits zero switching loss in pwm circuits with no conduction loss penalty," *IEEE transactions on industry applications*, vol. 29, no. 1, pp. 121–125, 1993.

[52] H. Hex inverting Schmitt trigger, "Rev. 7 21 november 2011, product data sheet."

[53] M. 6A High-Speed Power MOSFET Drivers, "Product data sheet."

Appendix A

Resonant Converters in Automotive Drive-Train Application

Power electronic converters applications are growing in electric vehicles drive-train. Electric vehicles' manufacturers are looking into improving the drive-train by utilizing the most advanced power electronic technologies which feature lower costs, higher efficiency and lower volume and weight. This chapter presents dc/ac and dc/dc high frequency inverter for automotive applications. It first, introduces the newest methods in high frequency converters, and it develops a dc/ac inverter and presents the results.

A.1 DC/AC Resonant Converters in Electric Vehicle Drive-Trains

The advantages of higher operating frequencies in converters are not only given by the reduced size of the passive filter components, but it also improves the efficiency and transient performance of them. With smaller capacitors and inductors in the circuit, there will be less amount of energy stored in the passive components and that allows a faster response to the load changes. Unfortunately, in any kind of switch type converters, switching losses are issue and by increasing the frequency, switching losses increase and high efficiency can not be achieved. In [45, 46] variable frequency resonant converters have been investigated using half bridges and in [47] a class-D resonant converter is used to increase the efficiency. In higher frequencies, building such a converter encounters several challenges. This section addresses some of these challenges and demonstrates certain ways to solve these problems. Some of the most suitable resonant converter topologies for operation at very high frequencies are the class-D series resonant converters, class-E and more recently the class-DE voltage-fed series resonant converters [48–50]. There are two ways to control output the voltage, frequency control and duty cycle control. Some researchers have proposed certain methods that control both duty cycle to maximize efficiency and control output voltage [51]. In this appendix, a topology for high frequency dc/ac converter is developed

and presented. Then, same topology is used in a dc/dc converter which has several application in electric vehicles such as boost up/down converters.

Figure A.1 shows the voltage and current of a MOSFET when it turns off for both hard switching and soft switching cases. The switching losses are proportional to the multiplication of the voltage and current of the switch. As seen, in hard switching the multiplication of the voltage and current will not be zero and it causes switching losses. Multiplication of voltage and current is switching losses and it is illustrated in Figure A.2a and Figure A.2b. On the other hand, in soft switching cases, the voltage of the switch starts to increase while the current has been already reached to value close to zero. Figure A.1 shows voltage and current of the MOSFET while Figure A.2c shows the switching losses for soft switching method. As seen, the switching losses has been incredibly reduced in soft switching method.

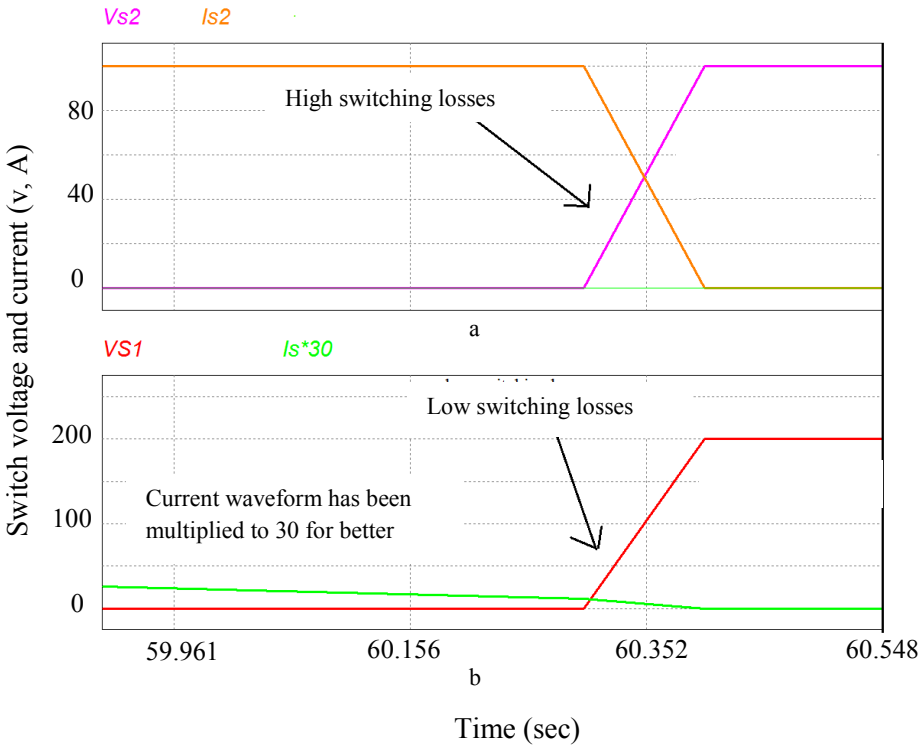

Figure A.1: Voltage and current of the switch the moment it is turned off a) hard switching b) soft switching

Figure A.2 shows the switching losses for three different cases. 100 kHz hard switching, 1 MHz hard switching and 1 MHz soft switching are shown in Figure A.2a, FigureA.2b and Figure A.2c, respectively.

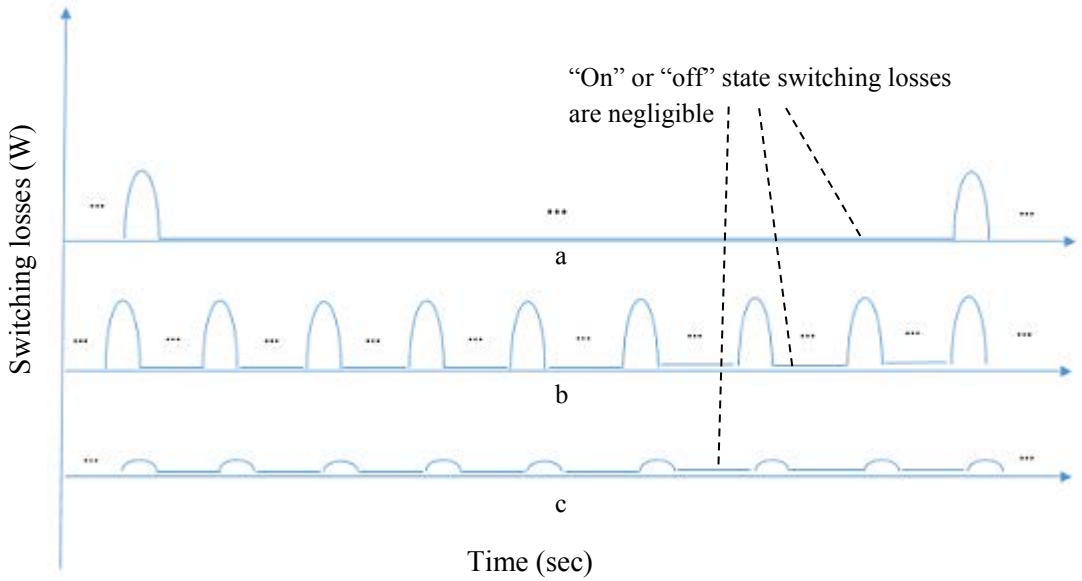

Figure A.2: Switching losses for three different cases

In Figure A.2a the frequency is 100 kHz. The time between turn off and the next turn on will be equal to 5 μs. Therefore, semiconductor device dissipate the heat generated by the turn off/on losses within that time. In Figure A.2b, however, the frequency is 10 times higher than previous case. There will be only 500 ns for the semiconductor device to dissipate the heat and stays in allowable temperature. In Figure A.2c the frequency is still high, but the switching losses have been greatly reduced due to the zero voltage switching and zero current switching.

A.2 Gate Drives for High Frequency Resonant Converter

In higher frequencies, there are some challenges regarding to developing a control circuit and MOSFET gate drives. Firstly, in both full bridge and half bridge converters, the upper MOSFET needs to have an isolated signal because the source pins are floated. There are different ways to provide an isolated signal for upper MOSFET including opt-couplers, electronic level shifters, bootstrap techniques and high frequency transformers.

Figure A.3 shows a typical schematic diagram of the controller for driving the half bridge. Different factors must be considered in high frequencies. This control circuit has been tested for frequency up to 3 MHz and works well. The main controller is a field-programmable gate array (FPGA) with the clock frequency of 50 MHz which is considered very fast for the power electronic converters control in electric vehicle drive-trains.

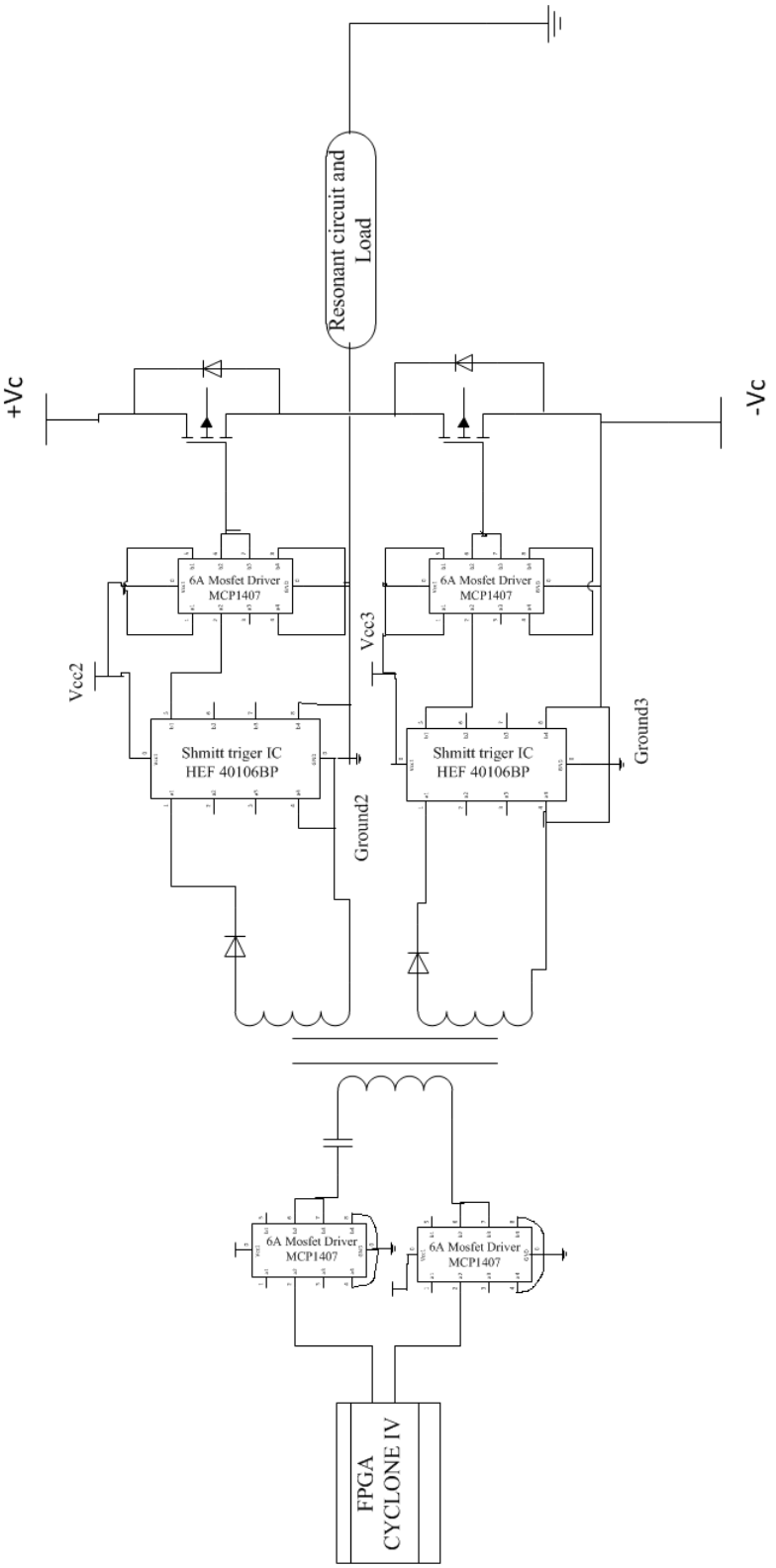

Figure A.3: Half bride gate drive circuit

Verilog hardware description language has been utilized to create the code for FPGA board. It creates two pulses which are complementary i.e. one is high/low

while the other one is low/high. The controller has been designed in a way that it independently controls the frequency and duty cycle in a wide range. The output pulses have peak voltage of 3.3 V. As seen in the schematic diagram, the output pulses of FPGA board go to the two buffers. Two IC MCP1407 have been used for this part for this purpose. Putting amplifiers between FPGA board and pulse transformer protects the board from high output current draw. The pulse transformers contain one core and three windings with same number of loops. The core is Ferrite Toroid which is selected for very high frequencies. The output pulses of transformer are ac pulses and must be rectified. The HEF40106B provides six inverting buffers and all inputs pass through a Schmitt trigger circuit. The Schmitt trigger circuit is used for enhanced noise immunity and/or to square up slowly changing waveforms [52]. The outputs of the Schmitt triggers go into two MOSFET driver ICs (MCP 1407). The MCP1406/07 devices are a family of MOSFET drivers that feature a single-output with 6A peak drive current capability, low shoot-through current, matched rise/fall times and propagation delay times. The MCP1406/07 MOSFET drivers can easily charge and discharge 2500 pF gate capacitance in under short amount of time [53].

There are three different dc sources for control circuit and they must be isolated from each other. There will also be a power source for the converter. Figure A.4 shows the experimental setup of the control circuit.

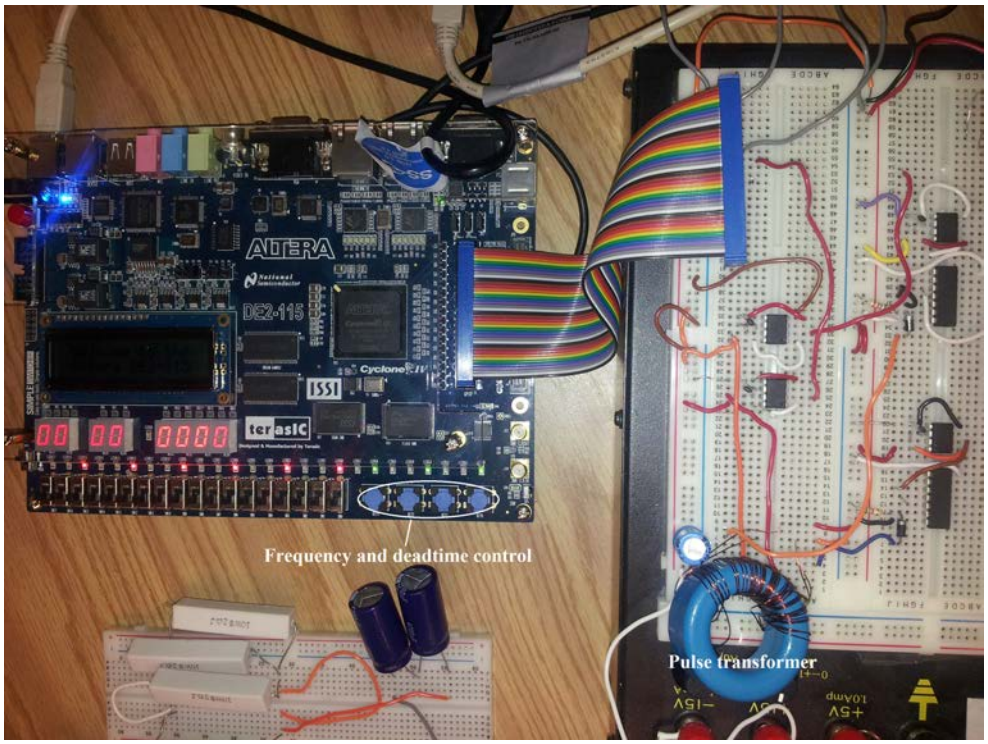

Figure A.4: Controller and MOSFET driver circuit

The output pulses of FPGA are shown in Figure A.5.

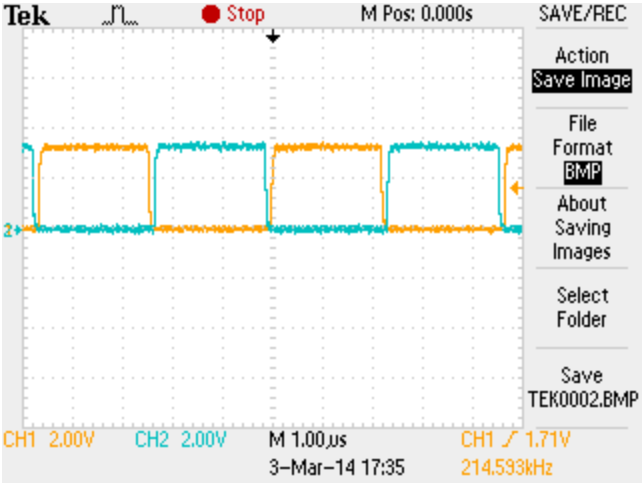

Figure A.5: Output pulses of the FPGA board

Since it is preferred to limit the current provided by the FPGA board, two buffers are utilized to amplify the output current of the FPGA which are seen in Figure A.4 and Figure A.5. The output voltage of FPGA is 3.3 v which is not high enough and the IC MCP 1407 is used to increase the voltage level, then, the output of the following ICs go to the pulse transformer. The output pulses of the transformer are shown in Figure A.6

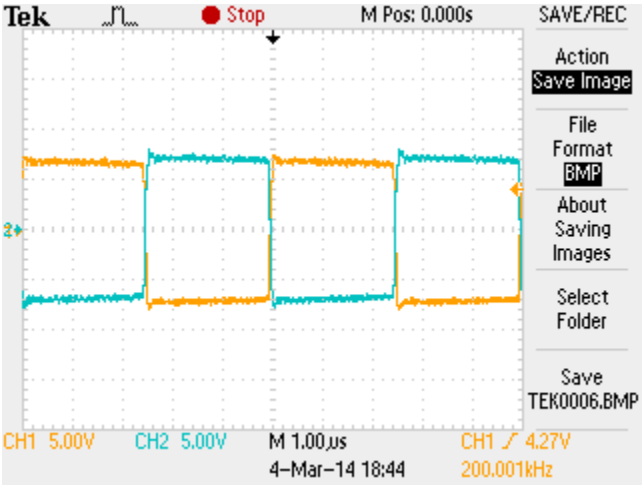

Figure A.6: Output pulses of the transformer

The output signals of the transformer are ac signal and they must pass through diodes to be rectified. The output pulses of the diodes are shown in the following figure.

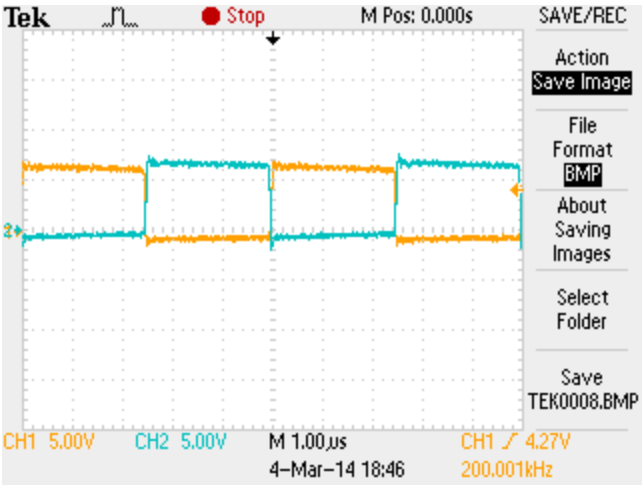

Figure A.7: Output pulses after passing through the diodes

The output of the diodes go to the Schmitt trigger IC (HF40106) to make cleaner pulses without any negative value. Since the diodes are used in this project are not suitable for very high frequencies, in reverse bias they act same as a small capacitors. If the frequency increases to higher value than 1 MHz, they may pass negative current as well. This problem can be solved by the Smith trigger ICs which can operate with negative pulses and they omit the negative part and generate good pulses with minimum rise and fall time.

A.3 Series-Parallel DC/AC Resonant Converter

A.3.1 Circuit basics

Figure A.8 shows a series-parallel resonant converter. Figure A.8a shows half bridge connected to LCR tank. $V_{in}(t)$ is a rectangular waveform with same frequency of switches. It is intended to calculate output voltage as a function of switching frequency, quality factor and input dc voltage.

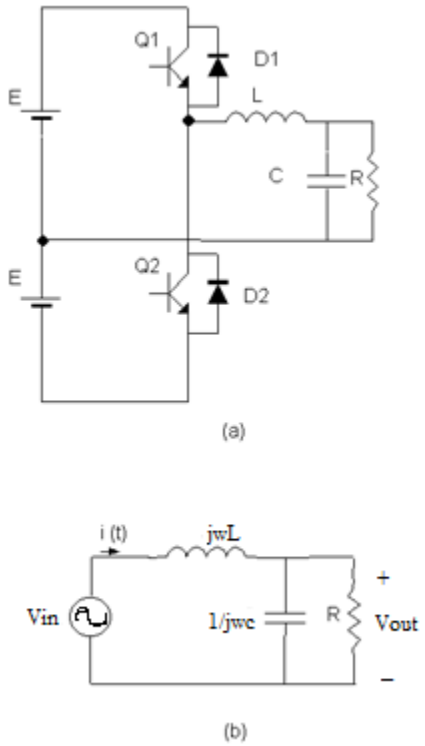

Figure A.8: Series-parallel RC circuit a) Original circuit b) Equivalent circuit

Equivalent impedance is evaluated as follow;

$$Z_{eq} = \frac{R - R\omega^2 LC + j\omega LC}{jR\omega L + 1} \tag{A.1}$$

$$I(t) = \frac{u(t)}{Z_{eq}} \tag{A.2}$$

$$\frac{V_{out}}{V_{in}} = \frac{1}{1 - \omega^2 LC + \frac{j\omega L}{R}} \tag{A.3}$$

Which ω_0 is resonance angular frequency and Q is quality factor. Quality factor is 2π times of peak stored energy of the elements divided to energy dissipated per cycle.

$$\frac{V_{out}}{V_{in}} = \frac{1}{1 - \frac{\omega^2}{\omega_0^2} + \frac{j\omega Q}{\omega_0}} \tag{A.4}$$

Converter gain versus switching frequency is shown in Figure A.9 .

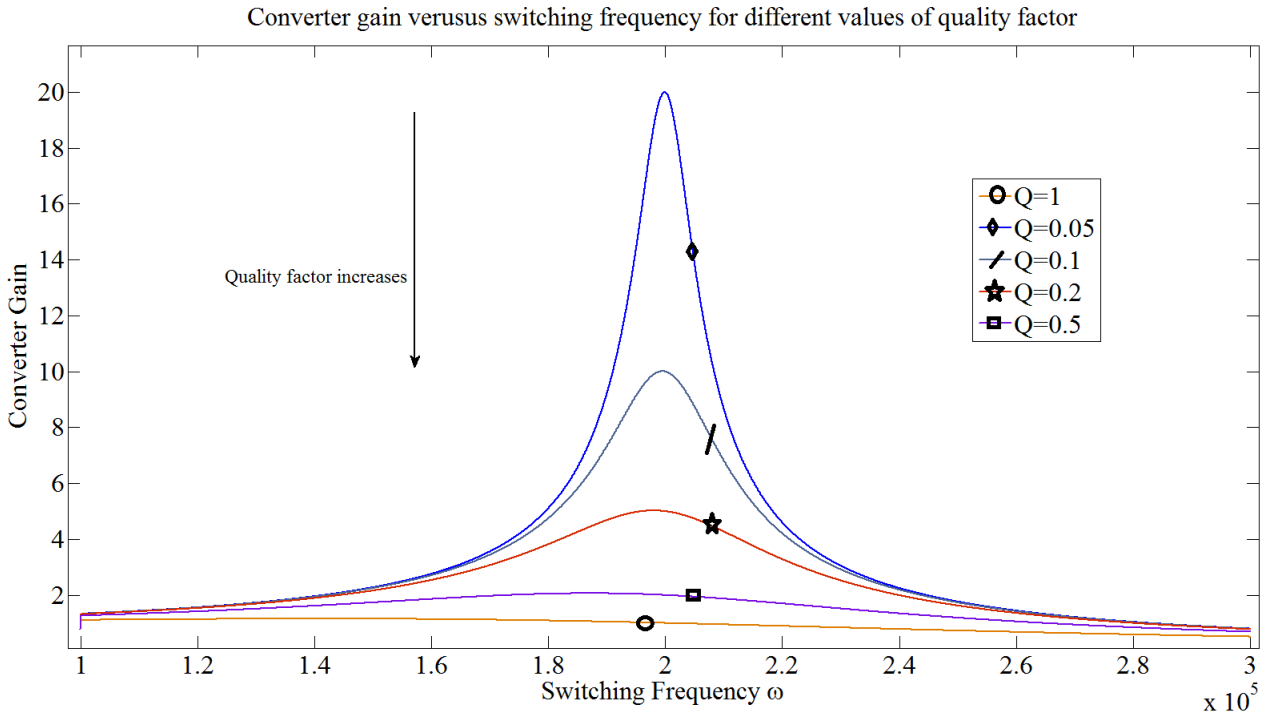

Figure A.9: Converter gain versus switching frequency

As seen in this figure, system gain increases if quality factor decreases.

A.3.2 Simulation Results

This converter has been simulated in PSIM software shown in Figure A.10.

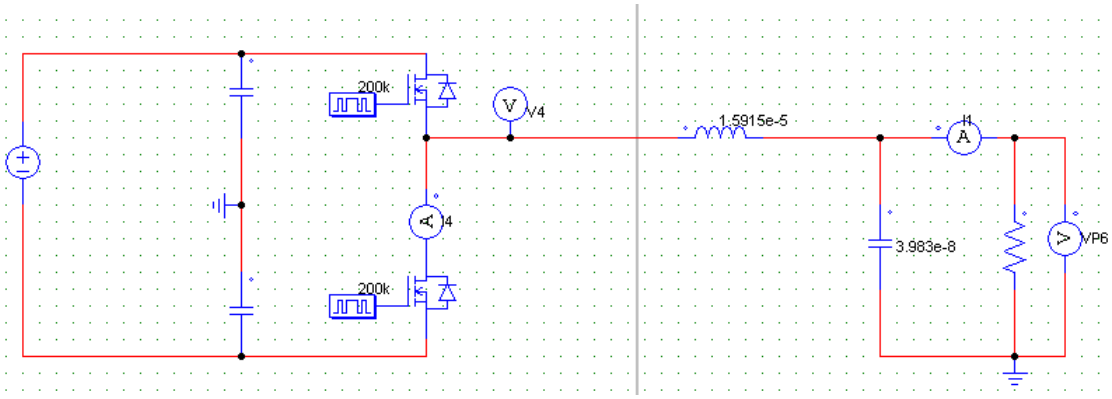

Figure A.10: Series-parallel resonant converter simulated circuit

Following table shows the parameters for this series-parallel resonant converter.

Figure A.11 shows input and output voltages for the selected circuit parameter which shown in table A.1. Since quality factor is 0.2 and also based on the mathematical model and Figure A.9, the converter gain must be 5 for the operating frequency

Circuit Characteristic	
ω_0	200 kHz
L	15.9μH
C	39.8nF
R	100
V_{dc}	10 V
Q	0.2

Table A.1: Circuit characteristic and parameter values

of 200 kHz. The output ac voltage has peak value of 32.2 V which is 5 times of the input voltage which shows good agreement with the mathematical model.

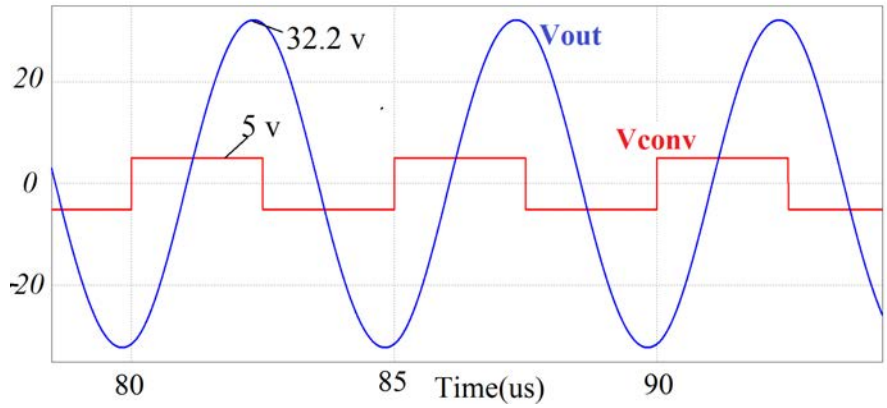

Figure A.11: Input and output voltage of the converter

Figure A.12 shows the voltage and current of the MOSFET.

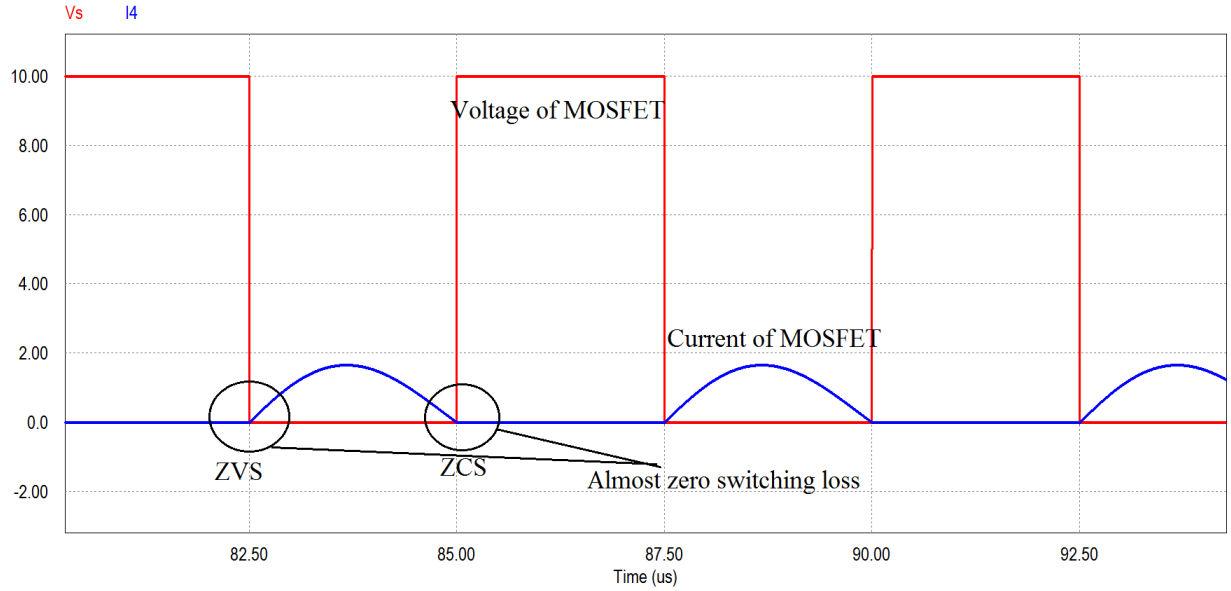

Figure A.12: Voltage and current of switch

Switching losses have been significantly reduced. As seen in this figure, the current starts to rise when the voltage of switch is zero and the current goes to zero before the switch turns off. Same as series resonant converter, switching losses will be non zero if circuit operate under or over resonance frequency.

A.4 Experimental Results

The complete system has been shown in Figure A.13

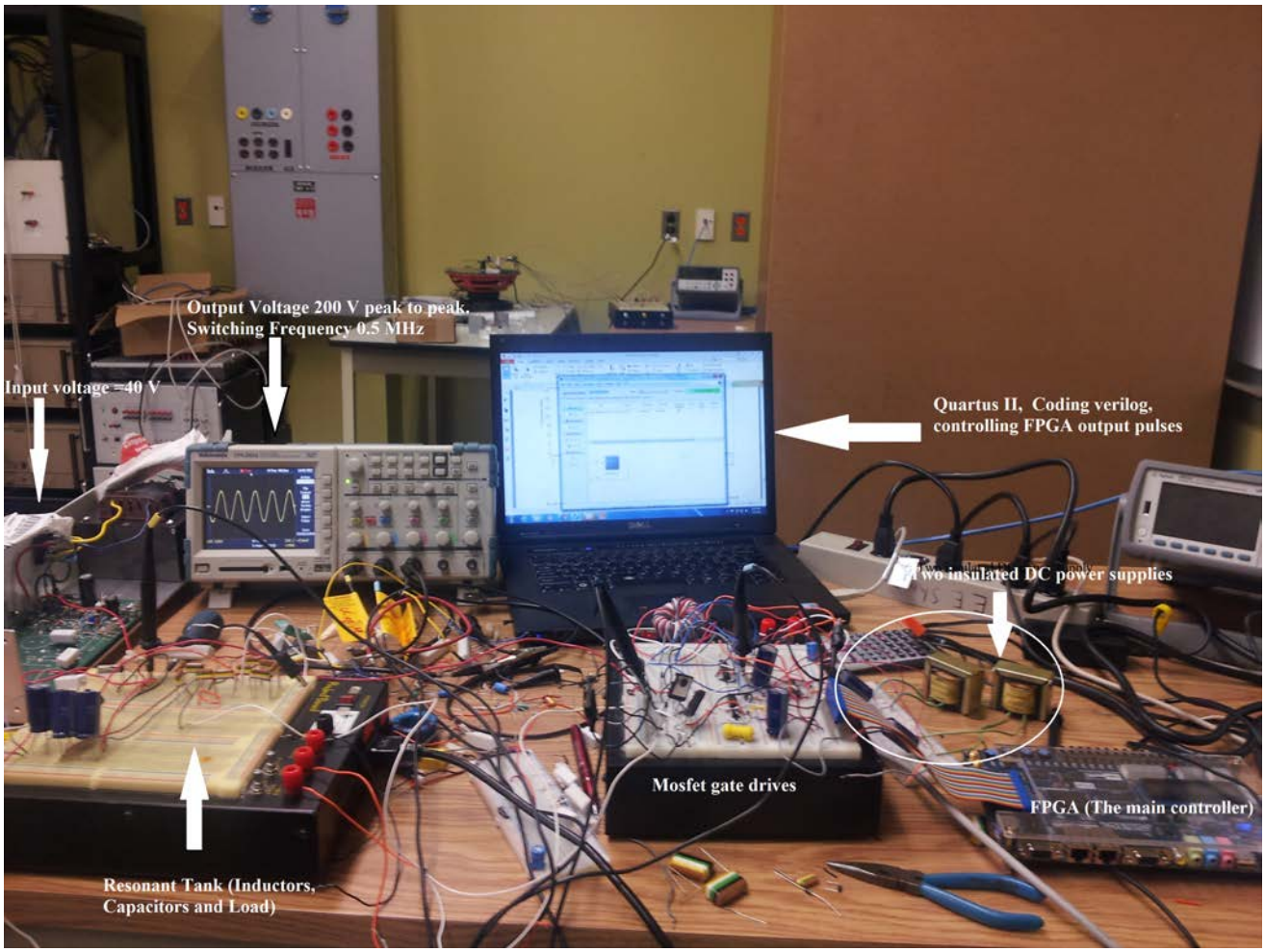

Figure A.13: Experimental setup

Input voltage is a dc power supply with a value of 40 V which will be divided to two since half bridge is used in this project. The output voltage of the half bride is shown in Figure A.14.

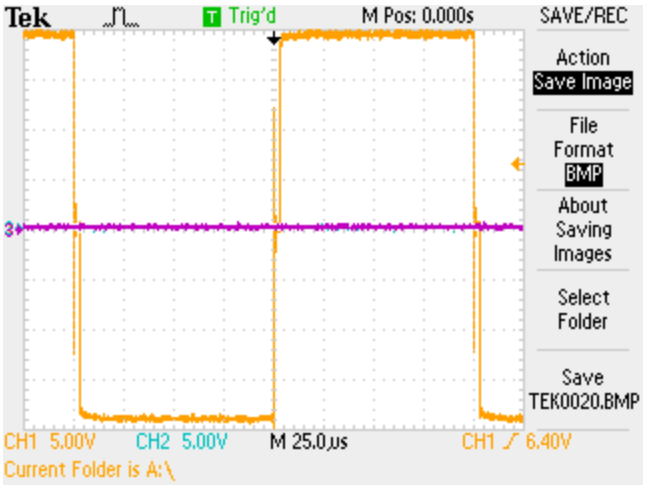

Figure A.14: Output voltage of full bride

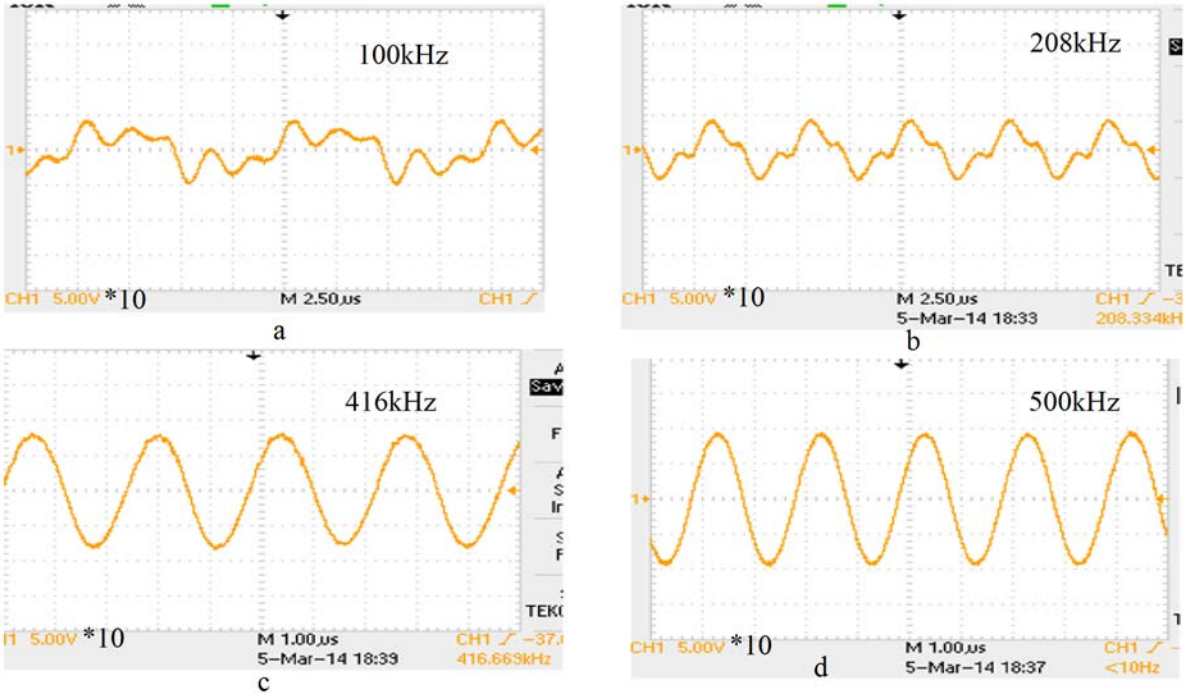

Figure A.15: Output voltage of the inverter for four different frequencies

The output voltage for different frequencies is shown below. If the switching frequency is less than 500 kHz the converter is functioning under frequency state which will generate lower output voltage than the nominal value as illustrated in Figure A.15. In Figure A.15a the frequency is 100 kHz and as seen the other harmonics are still shown in the output i.e. the impedance is zero for frequency of 500 kHz and for other frequencies including fundamental (100 kHz) is not zero. Therefore, the output does not look like a sinusoidal waveform with the frequency of 500 kHz. In Figure A.15b the frequency increases, the amplitude goes up and the output voltage become more similar to a sinusoidal waveform. For frequency of 416 kHz the output

looks pretty much like a sinusoidal waveform but still the amplitude is about 150 V peak to peak. Figure A.15d shows the output voltage when the switching frequency is very close the resonance frequency and the output is about 190 V peak to peak and it matches an ideal sinusoidal waveform. The gain of the circuit can be calculated by dividing the output voltage to the input voltage which will be 3.75.

A.5 Very High Frequency DC/DC Converter

This dc/dc converter is similar to the previous part. The major difference is that dc/dc converter has a rectifying bridge on the output to rectify the ac output voltage. In order to do than one can use four high speed diodes to rectify the high frequency ac voltage. Since the output voltage has very high frequency. The output filter for dc side can be very small.

This ac/dc part can be added to almost any type of resonant dc/ac converters. This ac/dc part is shown in Figure A.16.

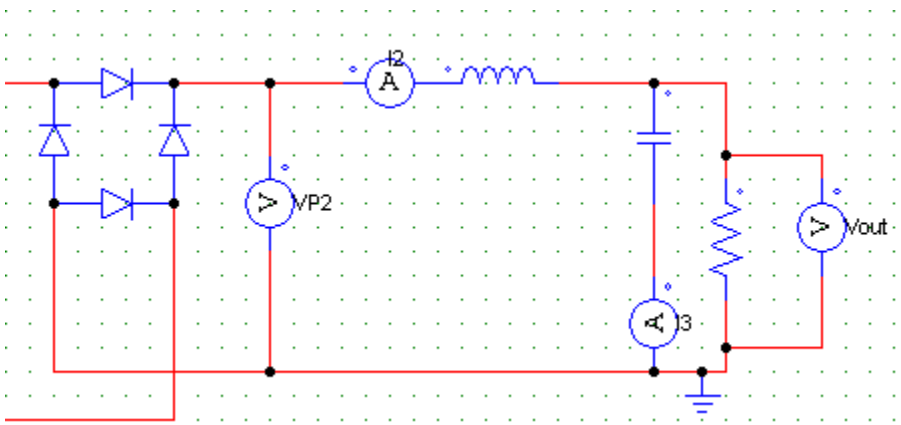

Figure A.16: AC/DC part of the dc/dc converter

The output dc depends on circuit quality factor and also can be controlled by changing the frequency as it is illustrated in A.9.